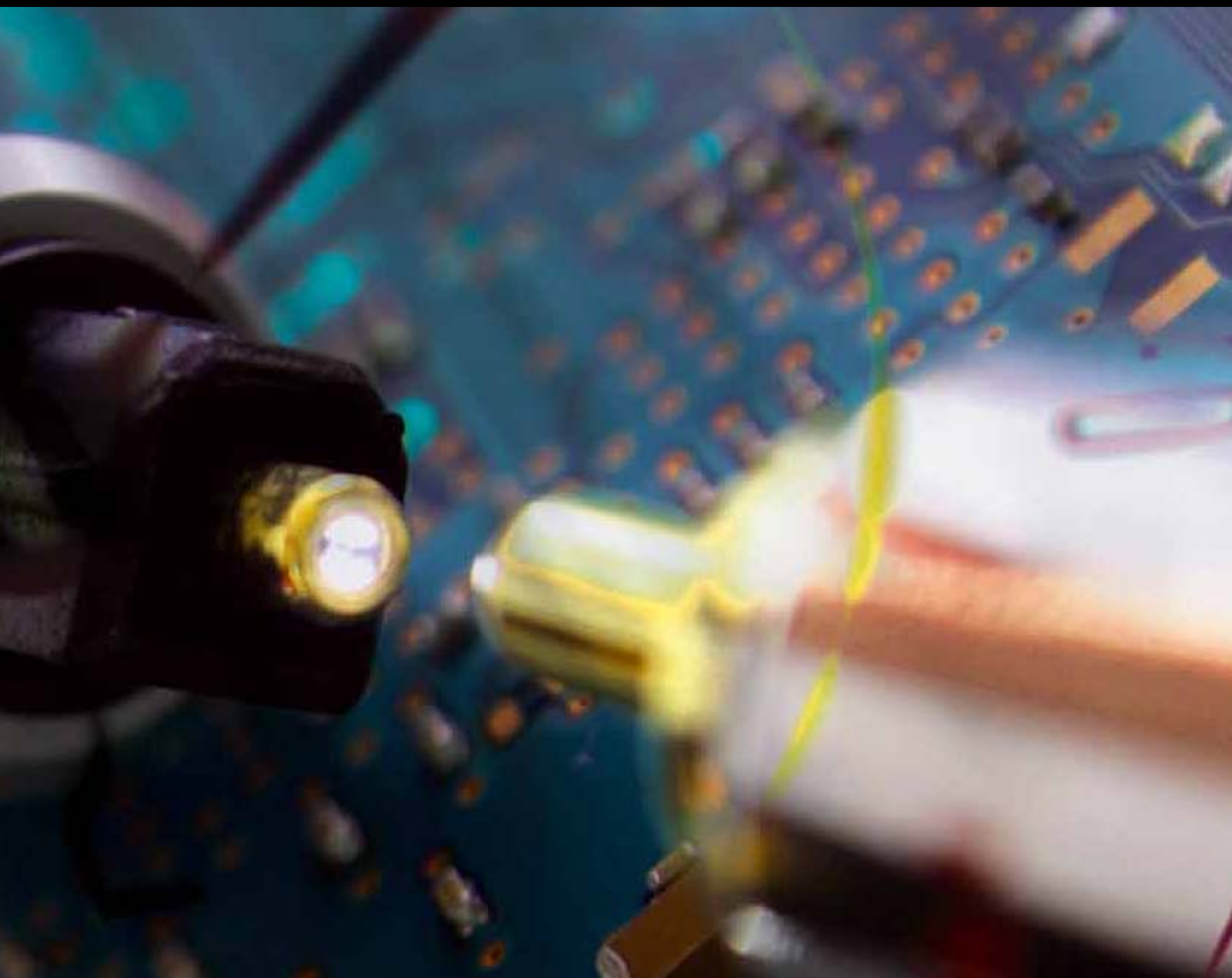# Advanced Sensor Technologies for Nondestructive Testing and Evaluation and Structural Health Monitoring

Guest Editors: Gui Yun Tian, Lalita Udpa, Raimond Grimberg, B. P. C. Rao, and Shenfang Yuan

Advanced Sensor Technologies for Nondestructive Testing and Evaluation and Structural Health Monitoring

Advanced Sensor Technologies for Nondestructive Testing and Evaluation and Structural Health Monitoring

Guest Editors: Gui Yun Tian, Lalita Udpa, Raimond Grimberg, B. P. C. Rao, and Shenfang Yuan

Editorial Board

Contents

Editorial

Advanced Sensor Technologies for Nondestructive Testing and Evaluation and Structural Health Monitoring

Gui Yun Tian,[1, 2] Lalita Udpa,[3] Raimond Grimberg,[4] B. P. C. Rao,[5] and Shenfang Yuan[6]

[1] School of Electrical and Electronic Engineering, Newcastle University, Newcastle upon Tyne, NE1 7RU, UK
[2] School of Automation Engineering, University of Electronic Science and Technology of China, Chengdu 611731, China
[3] Department of Electrical and Computer Engineering, Michigan State University, East Lansing, MI 48824, USA
[4] Nondestructive Testing Department, National Institute of Research and Development for Technical Physics, 47 D. Mangeron Boulevard, 700050 Iasi, Romania
[5] Metallurgy and Materials Group, EMSI Section, NDE Division, Indira Gandhi Centre for Atomic Research (IGCAR), Kalpakkam 603 102, India
[6] The Aeronautic Key Lab for Smart Materials and Structures, Nanjing University of Aeronautics and Astronautics Nanjing 210016, China

Correspondence should be addressed to Gui Yun Tian, g.y.tian@ncl.ac.uk

The need for monitoring the condition of critical structural components, that is, structural health monitoring (SHM), combined with increased requirements for the safety and quality of components, has resulted in the development of nondestructive testing and evaluation (NDT&E) and nondestructive evaluation (NDE) methods for characterising materials and detecting the presence of defects. Defects and abnormalities such as corrosion, residual stresses, and microstructural changes may result in the structural integrity being compromised and an increased likelihood of failure. NDT&E and SHM provide a means of identifying this damage and are often the only means of obtaining information about the current "health status" of a structure, through the installation of appropriate novel sensor technologies. It is our great pleasure to introduce the special issue in this emerging area to readers.

This special issue is devoted to the important area of sensor technology for NDT&E and SHM, aiming to cover diverse aspects such as novel sensing methods, smart structures, sensor arrays and distributed sensors, advanced signal processing for sensor systems, and sensors for device, structural, and environmental monitoring. The papers in this issue demonstrate applications in monitoring of material properties, monitoring of advanced materials (composites), wireless sensor networks, and structural health monitoring.

The issue contains several papers dealing with the NDT&E of various types of ferromagnetic components. The paper by I. J. Garshelis and G. Crevecoeur presents a novel method to measure hysteresis properties of ferromagnetic sheets using the magnetic field measurements measured by a magnet moved in the forward and reverse directions, where differences between these two measurements provide information on material properties affecting hysteresis. The paper by G. Psuj et al. presents a novel eddy current sensor for the detection of degradation in duplex stainless steel caused by an increase in sigma phase making the material more paramagnetic. W. S. Singh et al. present a paper on array of giant magnetoresistance (GMR) sensors to monitor the condition of steel track ropes. In this case the sensor array is constructed on a flexible PCB to wrap around the rope and detect flaws in and erosion of the steel rope. The paper by H. Lei et al. presents a method to monitor the health of steel belts used in elevators by measuring the resistance of the steel ropes within the belts. This technique allows monitoring of the stress fatigue present in the rope from resistance changes.

Two papers present work on inspection of composite materials. The paper by L. Cheng and G. Y. Tian shows how both flash thermography and the recently developed PEC thermography techniques can be used to identify delamination within carbon fiber reinforced polymer components. An

invited paper by T. Chady et al. presents a study of using pulsed terahertz (THz) and thermography measurements to detect impact damage in glass-fiber reinforced composites.

This special issue contains two papers on work relating to wireless sensor networks. The paper by O. M. Bouzid et al. presents a novel signal processing method for wireless sensor networks. Envelope and wavelet transforms are used to enhance the resolution of data from the sensors when low sampling rates are used. The paper by P. Wang et al. presents an overview on the use of wireless sensor networks for SHM, specifically for monitoring offshore wind farms. The paper deals with issues related to monitoring of different types of components and the integration of sensor nodes into a network.

The paper by S. D. Boone et al. presents a novel sensor for the structural health monitoring of concrete structures, measuring variations in longitudinal compression wave velocity and energy absorption in concrete structures, which have been subjected to fatigue loading.

Acknowledgments

Research Article

Investigation of Wireless Sensor Networks for Structural Health Monitoring

Ping Wang,[1] Yan Yan,[1] Gui Yun Tian,[2] Omar Bouzid,[2] and Zhiguo Ding[2]

[1] *College of Automation Engineering, Nanjing University of Aeronautics and Astronautics, Yudaojie Road 29, Jiangsu 210016, China*
[2] *School of Electrical and Electronic Engineering, Newcastle University, Newcastle upon Tyne NE1 7RU, UK*

Correspondence should be addressed to Ping Wang, zeit@263.net

Wireless sensor networks (WSNs) are one of the most able technologies in the structural health monitoring (SHM) field. Through intelligent, self-organising means, the contents of this paper will test a variety of different objects and different working principles of sensor nodes connected into a network and integrated with data processing functions. In this paper the key issues of WSN applied in SHM are discussed, including the integration of different types of sensors with different operational modalities, sampling frequencies, issues of transmission bandwidth, real-time ability, and wireless transmitter frequency. Furthermore, the topology, data fusion, integration, energy saving, and self-powering nature of different systems will be investigated. In the FP7 project "Health Monitoring of Offshore Wind Farms," the above issues are explored.

1. Background

Wireless sensor networks (WSNs) are considered one of the most important technologies in the 21st century, which will have a profound impact on the future way of life for humankind. A typical wireless sensor network consists of wireless communication, data acquisition, processing, and fusion stages. The sensor nodes are self-organised through a specific protocol and are able to obtain information about the surrounding environment, working together to accomplish specific tasks. The technology spans many fields, such as wireless communication, network technology, integrated circuits, sensor technology, microelectromechanical systems (MEMS), and embedded systems, to name just a few. Figure 1(a) illustrates the typical basic architecture of a sensor network, and Figure 1(b) shows the typical hardware of a sensor network node. In February 2003, "Technology Review," a magazine published in the United States, selected ten far-reaching impacts of emerging technologies, where sensor networks were ranked in the first place. The US Department of Defense gave high priority to wireless sensor networks and put it as an important research area, establishing a series of military research projects. Intel, Microsoft, and other companies also have carried out some research in the field.

Not only industry and defense organisations have shown strong interest in wireless sensor networks, some world class universities such as UCLA, MIT, Cornell University, and the University of California, Berkeley [1] also have carried out research on WSN and achieved some results. The University of California, Berkeley, presented network connectivity reconstruction method for sensor location, based on the correlation of the data coding modes, to determine the location of sensor network nodes; they also developed a sensor operating system, TinyOS. The Massachusetts Institute of Technology studied sensor network data stream management systems integration frameworks, query optimisation, network congestion control for energy saving purposes, along with middleware technologies such as positioning, tracking, networking, and scalable algorithms for large-scaled sensor networks. These studies received NSF, DARPA, and the Air Force Space Laboratory support. The ZigBee Alliance and IEEE also developed standards of Chinese version IEEE 802.15.4c [2].

After developing further in the past several years, some applications of wireless sensor networks have been turned
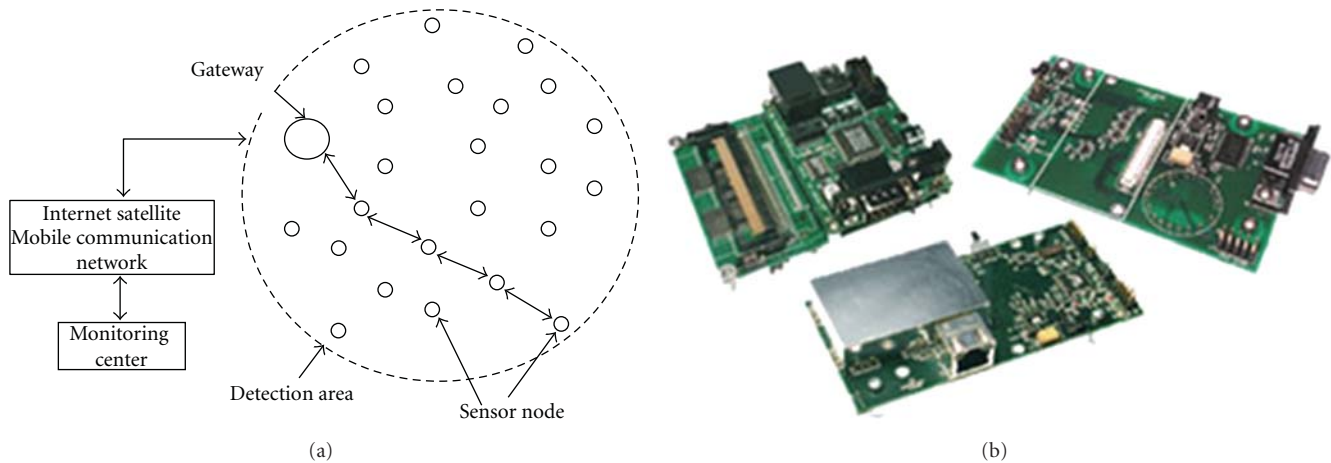
FIGURE 1: (a) a sensor network architecture. (b) hardware of sensor network nodes.

into products. Nowadays a number of WSN research platforms have been developed successfully, such as the University of California, Berkeley TinyOS/Mica, Smart Dust, and PicoRadio platforms. The ZigBee Alliance was codeveloped by Invensys, Mitsubishi Electric, TI, Motorola, Philips, and more than 20 other semiconductor and IT companies. Meanwhile, the IEEE has also developed the IEEE802.15.4 standards and has established a number of demonstration systems. Crossbow has developed a series of modules and products based on the ZigBee protocol and TinyOS, which can be used to form a WSN. TI has also developed some solutions based on ICs such as CC2431, which embed the ZigBee protocol of MAC and PHY on them and offer developments that contain the software and firmware of the complete ZigBee protocol stack [3].

Structural health monitoring (SHM) is a typical area amongst the many possible applications of wireless sensor networks. SHM is an emerging research area and is focussed on the field of infrastructure [4, 5], mainly on the integration and application of sensors, signal processing, and communication technologies. It also focuses on complex engineering systems and infrastructure to prevent structural failure and disaster, such as with the monitoring of bridges, large buildings, and dams. One of the possible SHM applications is that of a wind power monitoring system illustrated by the EU science and technology key project FP7 "Health Monitoring of Offshore Wind Farms." By 2020, China wind power capacity will reach 150 million kilowatts [6], and nondestructive testing (NDT) and SHM are useful means with which to reduce the maintenance costs of wind power, and to extend the lifetime of infrastructure, and to ensure the safety of power supply. As shown in Figure 2, the project aims to analyse wind power generation systems and to develop intelligent WSN and SHM technologies for the wind turbine blade, gearbox, generator, power electronics, and other structural components. In this project, a complete wind power system health analysis, life cycle assessment, fault diagnosis, maintenance management programs, planning and scheduling system of a complete windpower system

is provided, including the design, production, installation, maintenance, and supply chain feedback.

In Section 2, the key problems acting against the implementation of WSNs for SHM on wind power systems will be identified and discussed.

2. The Key Problems of Wireless Sensor Networks Combined with Structural Health Monitoring

As briefly discussed in Section 1, the key problems to developing such an SHM system in conjunction with WSN are summarised as follows: the problem of compatibility between different sensors, their sampling frequencies, and operational modes, the problem of transmission bandwidth and real-time ability variance, the selection of a wireless transmission frequency, topology choice, data fusion method, and the contrast between the energy consumption requirements of different applications to that of each different device. In the following subsections, each individual problem will be discussed in detail.

2.1. Sampling Frequency and Operation Mode. In the field of structural health monitoring, various types of sensors are used, including, but not restricted to, resistance strain, piezoelectric vibration, optical fiber strain, dip angle, acoustic emission, and stress measurement sensors [7]. Each of these sensors has different physical mechanisms and should thus be operated in different ways; some examples are given as follows.

(1) The signals of strain, deformations, and dip angle are static or of low frequency, and they usually work at low sampling frequencies. For example, some of the signals in a strain test are sampled by a frequency lower than 1 Hz. The likelihood of a request for data processing and real-time transmission is low.

(2) Vibration sensors usually measure objects where the level of vibration can range from dozens of Hz to
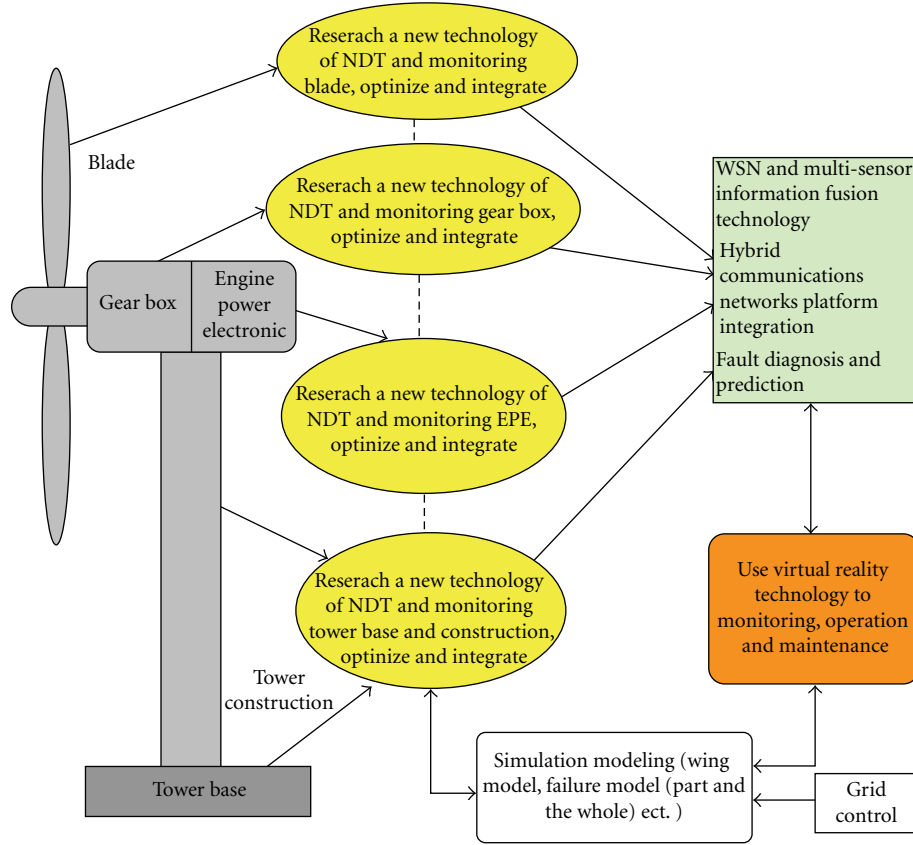
FIGURE 2: The system architecture of FP7 project "Health Monitoring of Offshore Wind Farms".

TABLE 1: The carrier frequency and transmission bandwidth of ZigBee Alliance and the IEEE 802.15.4 standard.

Carrier frequency	Band nature	Maximum bandwidth	Frequency point
2.4 GHz	ISM Worldwide	250 kbps	16
868 MHz	Europe	20 kbps	1
915 MHz	ISM Americas	40 kbps	10
780 MHz	802.15.4c (Chinese)	250 kbps	8

hundreds of KHz. Thus, there is a much greater requirement from the system in terms of sampling frequency, data processing, and transmission. The added need for synchronisation from the system adds an extra burden.

(3) Eddy current, pulsed magnetic flux leakage, and other nondestructive testing sensors are used for the monitoring of key components, where signals are sampled with a frequency of more than a few hundred Hz. In addition to this the requirement of data processing and analytical abilities from the WSN nodes is very high.

(4) The imaging sensors require the WSN nodes to have the ability to carry out high-speed data transmission. They also require WSN nodes to have certain decoding and image processing abilities.

As the task of structural health monitoring systems is a complicated one, consisting of the monitoring of many physical and electrical failures in different components, they need various sensors working together. The choices of the sensor network sampling frequency, from several Hz to several hundreds of kHz, working mode, and compatibility must be considered when choosing each node.

2.2. Transmission Bandwidth and Real-Time Monitoring. In general, with the requirements of low cost and low power, the design of WSN has mainly been for low bandwidth and non/nonurgent real-time applications, as shown in Table 1. For applications such as SHM, designs based on low-bandwidth and non-real-time systems can only be applied to strain deformation or dip monitoring, which require only slowly varying signal sensing and transmission. The data from vibration measurements as well as those resulting from image acquisition require a higher transmission bandwidth.
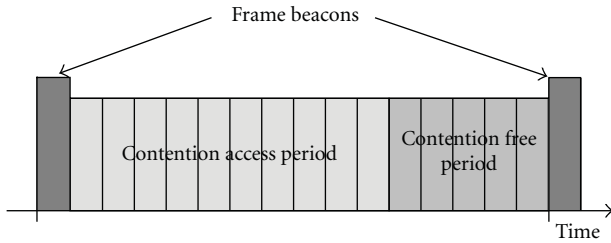
Figure 3: ZigBee MAC time slot with competition and sub-slot competition.

In addition to these, for some alarm transmission with high real-time requirements, such as those from pulsed eddy current measurement node (which can receive harbinger information of the sudden occurrence of crack), special considerations with regard to real-time network transmission need to be undertaken.

Except for the physical communication and processing capacity of a system, the protocols, especially MAC protocols, influence the real-time ability and transmission bandwidth of network communication [8, 9]. MAC technology usually consists of two different mechanisms, competitive and noncompetitive mechanisms. The competitive MAC mechanism, carrier sense multiple access with collision avoidance (CSMA/CA), is most commonly used. Distributed layer MAC protocols, which are based on the CSMA/CA protocol, use a sleep cycle mechanism to limit energy consumption. But a larger network time delay is produced as the system needs to be awoken from a sleep cycle before the data can first be sent to it and then transmitted onwards. In addition, the T-MAC (MAC) protocol transmits all of the data through a variable-length sudden transmission and sleeps during the two sudden transmissions to reduce spare detection.

Noncompetitive MAC protocols are generally used for cluster-based networks. The cluster head is responsible for allocating time slots to all of the sensor nodes within a cluster, collecting and processing data which is sent by the sensor nodes within a cluster, and forwarding data to the sink node.

In this project, we use a MAC mechanism, which is a combination of both competitive and noncompetitive methodologies, which is common practice in WSN technologies. One example of this is within ZigBee, with its purpose illustrated in Figure 3, allowing accommodation of the varied application requirements of a different network number of nodes and different real-time requirements.

Although the most common WSNs are for low-bandwidth applications, the development of technology and the demands of more diversified sensing technologies and more various information acquisition—especially for the application of acquisition of large amounts of data such as the vibration and image data—and the bandwidth requirements for sensor networks have enlarged and the management models required have become more strict.

2.3. Synchronization.
In structural health monitoring, there are many requirements regarding synchronous and real-time data acquisition of the vibration information, which

are distributed over different parts of an installation. It is especially important for the vibration model analysis of bridge structures, structural stability, and life assessments, which contain a large number of sensor nodes that are distributed over different positions, with different topology structures. The signals must be sampled synchronously by the nodes; otherwise there will be incorrect information (due to samples grouped together coming from different times) of the vibration phase, resulting in an incorrect vibration model judgement. In applications in which sampling frequencies usually exceed 1 KHz, the delay of the sensor nodes synchronisation is usually required to be less than $1\,\mu s$. This results in a higher requirement of synchronisation in an SHM WSN.

2.4. Operation Frequency.
The wireless carrier frequency has a direct impact on the physical layer transmission accessibility of a network, which plays a significant role in the application of structural health monitoring. Carriers of 2.4 GHz and 868 MHz and 915 MHz are used according to IEEE 802.15.4 and ZigBee Alliance standards listed in Table 1. The penetration ability through buildings at these frequencies is acceptable, but the diffraction characteristics are relatively poor. When the interior structure of a building is under test, the performance using ZigBee is poor due to poor penetration. In contrast, the 433 MHz ISM band, which is used widely in fields such as automated meter reading (AMR), has achieved relatively good results. In addition, the frequency band of 470 MHz has been selected to be the instrumentation and sensor network special frequency band in China.

Frequencies used in applications such as AMR can be a reference for comparison, classification, and standardisation of the carrier frequency of WSN in SHM.

2.5. Topology and Data Fusion.
WSNs need different topologies to meet the needs of different application characteristics in SHM. Typical topologies include star, cluster tree, and mesh networks [9]. Taking the ZigBee network for example, shown in Figure 4, the node is composed of both a reduced function device (RFD) and a full function device (FFD). The ZigBee standard supports the three kinds of topologies that were stated above [10, 11].

In the FP7 project mentioned previously, "Health Monitoring of Offshore Wind Farms," the project team compared the characteristics of three different topologies, as we can see in Table 2.

In our practical application, the star network is used for deformation monitoring of low-speed, nontimely applications. In addition to the above three forms, a chain structure (a simplification of mesh) and a combination of the chain structure and the three previous mentioned methodologies has become a commonly used topology.

2.6. Energy Issues.
A lot of WSN nodes in SHM applications work in environments where a direct power supply is not available, such as with nodes located upon spinning wind power blades. Therefore, any enhancement of a single node lifetime through the use of low-power technology is a major
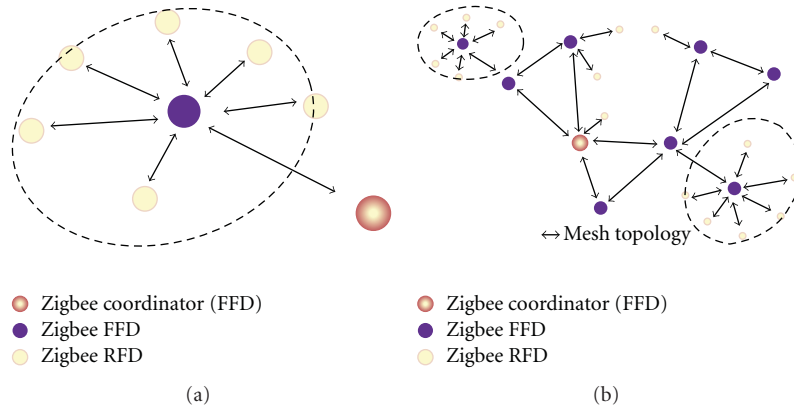
Zigbee coordinator (FFD)
Zigbee FFD
Zigbee RFD

Zigbee coordinator (FFD)
Zigbee FFD
Zigbee RFD

(a) (b)

Figure 4: ZigBee (a) STAR and (b) MESH network topologies.

Table 2: Comparison of three kinds of topology for WSN.

	Networking features	Advantage	Disadvantage
Star	Supporting point-to-multipoint and multipoint-to-point communication. Need for a concentrator or hub (coordinator for ZigBee network). All data are transited by hub. Suited for networking in which the distance between equipments is small and scattered in a circular fashion. Suitable for massive, low-speed, and non-real-time applications, such as distortion monitoring.	Brief structure. Protocol is simple by using a polling mode.	The entire spatial span of the transmission network is equal to the span of the physical layer. Concentrator can carry out the role of data fusion. Its reliability has the decisive effect regarding the performance of the entire network.
Cluster tree	Network is composed of many star topologies, using a star to connect the concentrator. Suitable for situations where data needs to be converged, such as in a structure monitoring network that has an intelligent analysis ability.	A leveled and clear structure. Transmission distance is greater than the star topology. Protocol is relatively simple and clearer than with mesh networks.	All the root nodes of the cluster tree (concentrator or the convergent point) are essential nodes, upon which there is also the demand of a high ability in terms of data fusion. Energy consumption and reliability as well as the influence on the entire network are a major issue.
Mesh	All entities can communicate with each other as long as they are within the scope of the network and if there is no direct path; they also can communicate in "multihop" fashion. They can form highly complex and large capacity networks. The network can cover a large physical space so it is suitable for installation on scattered structures. The network also has self-organisation and self-healing capabilities.	The behaviour of the single node is relatively consistent. The capacity of the network is large. Generally it does not have any essential node. There are many available communication routes and the success ratio of the transmission is increased in comparison to those gained with other networks.	The behaviour of the entire network is not easily controlled. With an increasing number of nodes, the complexity of the network behaviour increases greatly and the efficiency is reduced.

issue in the application of WSN. Impacting factors upon the lifetime of nodes and the entire network include the following.

(1) The Working Principle and Mode of Sensing System. Each of the many sensors that adopt different physical principles to detect the different phenomena of strain, vibration, obliquity, cracks, the sampling frequency, working mode, and working energy consumption has a very different working principle. A resistance strain sensor operational current needs range from about $200 \sim 400$ uA, while pulsed eddy current sensors require an excitation current of up to 1A or more. Low-speed, low real-time detection usually operates in a larger working cycle, and vibration signals are usually sampled by continuous measurements. The working mode of each sensing system has a decisive influence on the energy consumption of the overall WSN.

(2) The Low-Power and Dormancy Wake-Up Mechanism of Node. Each node employs its own technology to achieve

low power consumption, whilst ensuring the monitoring application. This has to be achieved via the work/sleep mode along with a low duty cycle [12]. Currently the dormancy mode of low-power nodes has reduced current consumption to 1 uA. Generally, the ZigBee node designed for low-speed and real-time applications can run for a period of 6 months to 2 years, with the power supplied by a single AAA battery. In SHM applications such as strain testing, the duty cycle is usually low and so the life of nodes is long.

(3) The Impact of Network Protocols and Calculated Capacity. The calculated capacity requirements of hardware and for the node itself will have a direct impact upon the function of the node. Low-power requirements often conflict with the processing protocol of the WSN, its secure computational ability, and so on. Each function of a WSN, such as self-organisability, adaptability, signal sampling, and information fusion, requires energy consumption. How to ensure the above-mentioned aspects of performance under the condition of low power consumption is always a WSN most crucial issue.

In addition, reasonable network protocols will also play an enhanced role in the reliability of the entire network. For example, in a tree structure, based on the remaining node energy consumption, the key nodes (such as the tree root node and concentrators) are selected in turn. This approach greatly enhances the reliability of the system.

(4) The Self-Powering Capacity of the Node. Currently, with the tendency towards green energy conservation technology development, the use of self-power-generation technology to support nodes has become a research hotspot. Typical self-generation technologies include solar energy technology, vibration and wind-power generation based on the principle of electromagnetic induction, vibration generation based on the principle of the piezoelectric effect, electrostatic collection techniques, and thermoelectric technology based on the temperature effect [13–16]. Amongst these, ZigBee blends the self-generation node into a self-supported system.

In some SHM applications, vibration is the object of measurement as well as the potential power supply source, such as with the vibration of motors and bridges or the spin of blades on a wind farm. In other circumstances there is a large range of solar or temperature change, especially in the west of China, where wind farms are built on a large scale.

3. Conclusion

Wireless sensor networks are one of the supporting technologies in structural health monitoring. Through intelligent, self-organising means, they connect sensor nodes, with a variety of different test objects and working principles into a network along with functions of data processing and integration. Structural health monitoring is a convergence area, with a variety of sensor and information processing technologies. Sampling frequencies, operational modalities of different sensors, their respective transmission bandwidth, and real-time monitoring including interference, wireless operation frequency problems, topology, data integration, and energy issues have been laid out as the key components that will need to be considered carefully when designing the wireless sensor network. In this FP7 project HEMOW, "Health Monitoring of the Offshore Wind Farm Monitoring," our international consortium including research teams from China, India, Poland, and the UK will address the above issues in great detail over the next few years.

References

[1] http://www.jlhlabs.com/jhill_cs/jhill_thesis.pdf.

[2] Part 15.4: Wireless Medium Access Control (MAC) and Physical Layer (PHY) Specifications for Low-Rate Wireless Personal Area Networks (WPANs), IEEE 802.15.4, 2009.

[3] http://www.ti.com/.

[4] H. Q. Si and T. G. Wang, "Calculation of the unsteady airloads on wind turbine blades under yawed flow," *Modern Physics Letters B*, vol. 23, no. 3, pp. 493–496, 2009.

[5] S. Yuan, X. Lai, X. Zhao, X. Xu, and L. Zhang, "Distributed structural health monitoring system based on smart wireless sensor and multi-agent technology," *Smart Materials and Structures*, vol. 15, no. 1, pp. 1–8, 2006.

[6] Fundamental study of Large Size Wind Turbine Aerodynamics, funded by the National Basic Research Program of China; funding: 35 million RMB; project leader: Tongguang Wang, duration: 2007–2011.

[7] J. W. Wilson, G. Y. Tian, and S. Barrans, "Residual magnetic field sensing for stress measurement," *Sensors and Actuators A*, vol. 135, no. 2, pp. 381–387, 2007.

[8] C. Shen, C. Srisathapornphat, and C. Jaikaeo, "Sensor information networking architecture and applications," *IEEE Personal Communications*, vol. 8, no. 4, pp. 52–59, 2001.

[9] J. Yick, B. Mukherjee, and D. Ghosal, "Wireless sensor network survey," *Computer Networks*, vol. 52, no. 12, pp. 2292–2330, 2008.

[10] ZibBee Alliance, ZigBee Specification, ZigBee Document 053474r06 Version 1.0., 2004.

[11] IEEE Standards 802.15.4 TM-2003.Wireless medium access control (MAC) and physical layer (PHY) specifications for low-rate wireless personal area networks (LR-WPANs), 2003.

[12] K. Vijayaraghavan and R. Rajamani, "Active control based energy harvesting for battery-less wireless traffic sensors: theory and experiments," in *Proceedings of the American Control Conference (ACC '08)*, pp. 4579–4584, June 2008.

[13] A. Hande, T. Polk, W. Walker, and D. Bhatia, "Indoor solar energy harvesting for sensor network router nodes," *Microprocessors and Microsystems*, vol. 31, no. 6, pp. 420–432, 2007.

[14] Y. K. Tan, K. Y. Hoe, and S. K. Panda, "Energy harvesting using piezoelectric igniter for self-powered radio frequency (RF) wireless sensors," in *Proceedings of the IEEE International Conference on Industrial Technology (ICIT '06)*, pp. 1711–1716, Mumbai, India, December 2006.

[15] L. Mateu, C. Codrea, N. Lucas, M. Pollak, and P. Spies, "Energy harvesting for wireless communication systems using thermogenerators," in *Proceedings of the IEEE XXI Conference on Design of Circuits and Integrated Systems (DCIS '07)*, Barcelona, Spain, November 2006.

[16] M. T. Penella and M. Gasulla, "A review of commercial energy harvesters for autonomous sensors," in *Proceedings of the Instrumentation and Measurement Technology Conference (IMTC '07)*, pp. 1–5, Warsaw, Poland, May 2007.

Research Article

A Simple Magnetostatic Sensing Method for Assessing the Local Hysteresis Properties in Ferromagnetic Sheet Materials

Ivan J. Garshelis[1] and Guillaume Crevecoeur[2]

[1] *Magnova, Inc., 17 Downing Three, Pittsfield, MA 01201, USA*
[2] *Department Electrical Energy, Systems and Automation, Ghent University, Sint-Pietersnieuwstraat 41, B-9000 Ghent, Belgium*

Correspondence should be addressed to Ivan J. Garshelis, ijgarsh@att.net
and Guillaume Crevecoeur, guillaume.crevecoeur@ugent.be

Global hysteretic properties of electrical steels can be measured using ring or strip samples, while the assessment of the local hysteretic properties is a much more difficult task since the measurement method needs to be very sensitive. This paper presents a new method wherein the intensity and spatial distribution of the magnetic field, arising from large gradients in the local magnetization, are measured. These large gradients are induced by the passage of a test sample through the steep gradient field of a small, proximate permanent magnet. Magnetic field measurements during both directions of motion provide information indicative of the hysteresis properties. We theoretically analyze these measurements and show experimentally that the measurements correlate well with all the significant aspects of conventional hysteresis loops. The results given in this paper are qualitative, and the method is both by its simplicity and its sensitivity to important hysteresis features a powerful means of magnetic nondestructive evaluation.

1. Introduction

Hysteresis loss is not only a critical factor in the selection of steels for use in electrical machines but, by its nature, can also provide significant information on the structural condition and/or magnetic anisotropy of ferromagnetic materials generally. With electrical steels, the energy loss itself is the usual parameter of prime interest, whereas one or both of its (typically) key components, namely, coercivity and the remanent induction, or at some other "standard" field intensity, provide the sought for information. There is a need for a technique that can give useful information about relationships between microstructure or internal stress with magnetic performance.

Conventional measurements of hysteretic properties usually employ ring or strip samples, with the latter being necessary when anisotropy is being explored [1]. Indeed, the directional nonuniformity of the magnetic properties is measured by cutting samples at various angles from a sheet of material. Nondestructive determinations of local properties on the other hand, for example, to explore the relative structural damage associated with different processes used to cut electrical steel sheets, typically require either specially prepared samples [2], sophisticated techniques such as the needle probe method [3], or specialized apparatus such as with the drag force method [4]. All methods except drag force employ magnetic fields derived from electric currents.

A new magnetostatic method for obtaining comparative measurements of hysteresis loss and its components in ferromagnetic sheet materials is described in this paper. The measurements will be shown to provide qualitative information, which correlates directly with all of the significant aspects of conventional hysteresis loops. Essential features of the measurement apparatus are shown in Figure 1. The distance between the Motion Limits is called the "Stroke." The field sensor is located at the center of the Stroke, generally as close to the SUT surface as its physical package allows ($c \approx 0$). The size of the Stroke is typically from 10 G to 20 G. Remark that the presented method can measure the directional nonuniformity of the magnetic properties in a nondestructive way.
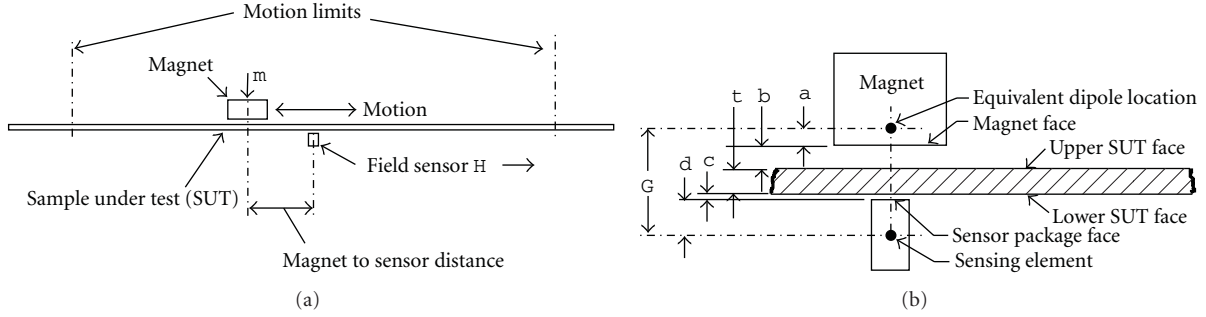
Figure 1: (a) Side view of basic arrangement. (b) Magnified view of the active elements showing the dimensional factors that contribute to the "Gap", $G \cdot x$ is the longitudinal distance between the magnet and the field sensor.

The *modus operandi* of the measurement method is as follows: the magnet, polarized normal to the sample under test (SUT) surface, initially located at one end of the Stroke is moved, at a speed slow enough (~ 3 mm/s) such that making it slower does not significantly alter the results, across the face of the SUT at a small fixed separation distance (0.05–2.5 mm) until it reaches the opposite Motion Limit at which time the motion is stopped. It is then moved, at the same speed and separation distance, back to its starting position. This "initializing" cycle of motion is repeated several times to obtain stable magnetization excursions in the SUT. During the next *forward* traversal of the Stroke, both the intensity of the field (in the longitudinal direction), $H_{\mathrm{F}}(x)$, and the coincidental longitudinal distance between the magnet and the field sensor, x, are measured and recorded. After a momentary stop at the end of the Stroke, motion is resumed in the *reverse* direction, during which, the field, $H_{\mathrm{R}}(x)$, and corresponding position are again measured and recorded. For each recorded data pair $(H(x), x)$, the difference, $H_{\mathrm{F}}(x) - H_{\mathrm{R}}(x) = D(x)$, is calculated. As will be seen, $D(x)$ will have some salient features (maxima, minima, and others) that correlate with the SUT's hysteresis loss and its components.

2. Theory

2.1. Assumptions. The inarguable simplicity of the method and apparatus notwithstanding, a detailed understanding of its operation is quite the opposite. Nevertheless, the operational basis and a *qualitative* relationship between features of $D(x)$ and hysteresis can be made adequately clear by an analytical model built from the following assumptions.

(1) The *existence* of the signature features in $D(x)$ reflects magnetic hysteresis in the sample; in the absence of hysteresis $D(x) \equiv 0$.

(2) The field from the magnet and its spatial distribution are approximated well enough by that of an equal moment dipole located within the magnet body.

(3) A solution of the 2D problem is sufficient.

(4) The sample is assumed to be thin enough such that the field from the magnet, while varying with longitudinal position, is uniform throughout its

thickness. This assumption ignores thus also radial components of the field from the magnet.

(5) The instantaneous local magnetization at points within the sample, $M(x)$, is determined entirely by the instantaneous local field from the magnet, $H_L(x)$, and the history of changes in that field. It is recognized that $H_{\mathrm{F}}(x)$ and $H_{\mathrm{R}}(x)$ are each comprised of components from two sources, the magnet and $\nabla \cdot M(x)$ within the sample. Nevertheless, effects of these latter fields on $M(x)$ are ignored on the assumption that they modify only *details* of the $D(x)$ signature features, not their presence.

(6) The *M-H* characteristics of the sample can be defined by any function which results in closed, symmetrical, sigmoidal loops without concern for underlying physical sources, for example, domain wall pinning or anisotropy. Thus suitable loops can be constructed from purposefully modified Langevin functions.

The authors are fully aware that this model is an approximation, but it enables to directly correlate simple hysteresis properties with the $D(x)$ measurements. This is the major aim of the theory shown here. More advanced numerical techniques could be used for understanding in depth the measurements.

2.2. Analysis. Guided by the previous assumptions, the analysis proceeds as follows.

(a) Determine the variation with x of the longitudinal component of the field (H_L) from the equivalent dipole source.

(b) Determine the sequence of field variation at underlying points in the sample during forward and reverse motion of the magnet, that is, $H_L(x)_{\mathrm{F}}$ and $H_L(x)_{\mathrm{R}}$.

(c) Create families of hysteresis loops with variable loss densities and components, that is, $M(H_L)$ functions with different values of coercivity and remanence.

(d) Determine $M(x)$ for both directions of motion by transposing the sequence of field variation, that is, $H_L(x)_{\mathrm{F}}$ and $H_L(x)_{\mathrm{R}}$ onto the $M(H_L)$ loops created in (c).

(e) Determine $\nabla \cdot M(x)$ ($= \varphi$, the free-pole density) for each direction of motion. (This becomes a second source (in addition to m) of the sensed field.)

(f) Determine $\nabla \varphi(x) = -H$ for each direction of motion, that is, $H_F(x)$ and $H_R(x)$.

(g) Determine $D(x) = H_F(x) - H_R(x)$, identify, and characterize salient features.

(h) Correlate feature characterizations from (g) with hysteresis loop features from (c).

For the arrangement diagrammed in Figure 2, the relationship between H_L at point P (the location of the field sensor in Figure 1), and P's distance from a dipole of moment m, is found (following from Cullity's derivation [5]) as

$$H_L = 3m \frac{xG}{(x^2 + G^2)^{5/2}}. \tag{1}$$

The longitudinal component H_L is directed to the right at points to the right of O ($x > 0$) and to the left at points to the left of O ($x < 0$), thus $H_L(x) = -H_L(-x)$. Equation (1) with $m = 1$ and $G = 1$ is plotted in Figure 3. The numbers indicate noteworthy magnet (dipole) positions relative to a field sensor at $x = 0$ during its motion in the forward, F, and reverse, R, directions of motion. When, for example, the magnet is at position 1, $H_{L1} = -0.00435$, at position 2, $H_{L2} = -0.8587$, at position 3, $H_{L3} = 0$, and so forth. Since the field distribution is effectively "attached" to the magnet, it moves together with the magnet. Determination of $M(x)$ requires knowledge of the corresponding M-H relationships for the sample material. Assumption 6 permits suitable, analytically defined M-H functions to be created from modified Langevin functions.

Ascending and descending limbs of hypothetical hysteresis loops are, respectively, generated from

$$M_a = \coth(k(H - H_c)) - \frac{1}{k(H - H_c)}, \tag{2}$$

$$M_d = \coth(k(H - H_c)) - \frac{1}{k(H + H_c)}, \tag{3}$$

wherein the "constants" H_c and k provide means to vary the "coercive field" and "remanence ratio," respectively, thereby to simulate different sample materials. Indeed, we use H_c to shift the function along the H axis, to the left ($+H_c$) to obtain the descending limb of the loop and to the right ($-H_c$) to obtain the ascending limb. Similarly, we use k to adjust the tilt of these loop limbs, which modifies the remanence ratio.

A closed loop is formed by shifting M_a upward and M_d downward by 1/2 the difference, $\Delta = M_d - M_a$, when H is at its peak value, H_P, in (2) and (3). The loop will then consist of an ascending limb:

$$M_A = M_a + \frac{\Delta}{2}, \tag{4}$$

and a descending limb:

$$M_D = M_d - \frac{\Delta}{2}. \tag{5}$$
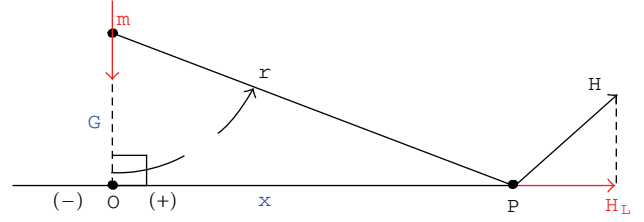
FIGURE 2: Diagram showing the field H, present at a point P, distance r, and angle q (x and G) from dipole m.
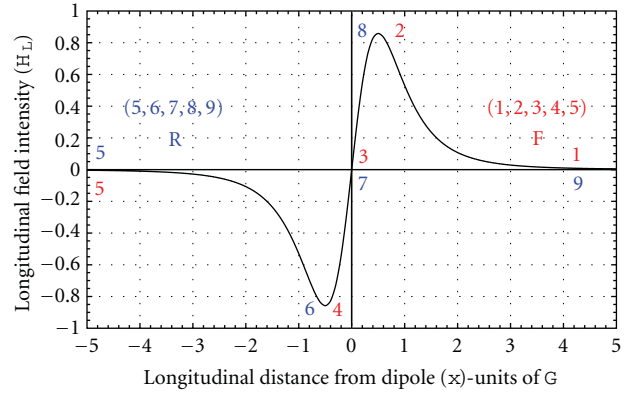
FIGURE 3: Variation in (normalized) H_L with distance x. Note that H_L is symmetrical around the origin, has peak values of ± 0.8587 at $x = \pm 0.5$, and becomes only ± 0.00435 at $x = \pm 5$.

Hypothetical positive and negative *minor* limbs from remanence ($H = 0$) to $H = \pm H_P$ can be produced from

$$M_{m+} = M_A + \frac{M_D - M_A}{1 + f * H},$$

$$M_{m-} = M_D + \frac{M_A - M_D}{1 - f * H}, \tag{6}$$

where f ($\ll 1$) is selected to insure that $|M_m|$ increases continuously with increasing $|H|$ while staying always between M_A and M_D. Of the three shape modifiers (H_c, k, and f), only H_c has physical dimensions (the same as those of H).

From the above equations, it is possible to determine $\nabla \cdot M(x) = \varphi$ for both the forward and reverse directions: $\varphi_F = (\partial M_{m+}(x))/\partial x$ and $\varphi_R = (\partial M_{m-}(x))/\partial x$, from which $H_F(x) = \nabla_{\varphi F}(x)$ and $H_R(x)$, and thus $D(x)$, can be calculated.

To avoid the need to deal with equations having ever growing numbers of ever more complex terms, and to provide means for graphically following the evolving analysis, we assign arbitrary (but as will be seen, arguably reasonable) values to the material-dependent parameters H_c, k, and f, and set $H_P = 15$. In this way, M_A, M_D, M_{m+} (for $0 \le H \le H_P$), and M_{-m} (for $0 \ge H \ge -H_P$) become numerical functions of H. For similar reasons and to make $H_{LPeak} = H_P = 15$, we assign the value $5/0.8587 = 17.47$ to m in (1).

As the magnet moves forward from $x = -5$ to $x = 5$, $H_L(0)$ and $M(0)$ will follow the sequence shown in Figure 4(a), and during reverse motion (from $x = 5$ to $x = -5$), the sequence shown in Figure 4(b). The corresponding
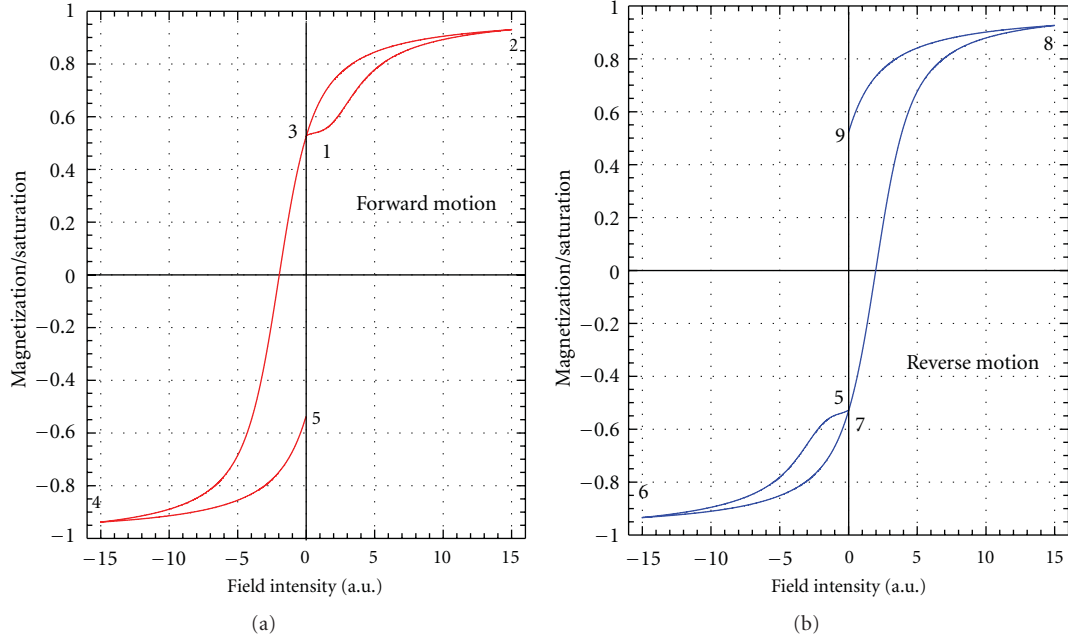
FIGURE 4: (a) Variation of field and resulting magnetization at the point on the SUT, which is directly over the field sensor during forward motion of the magnet. (b) Same for reverse motion. ($H_c = 2$, $k = 1$, $f = 0.135$).
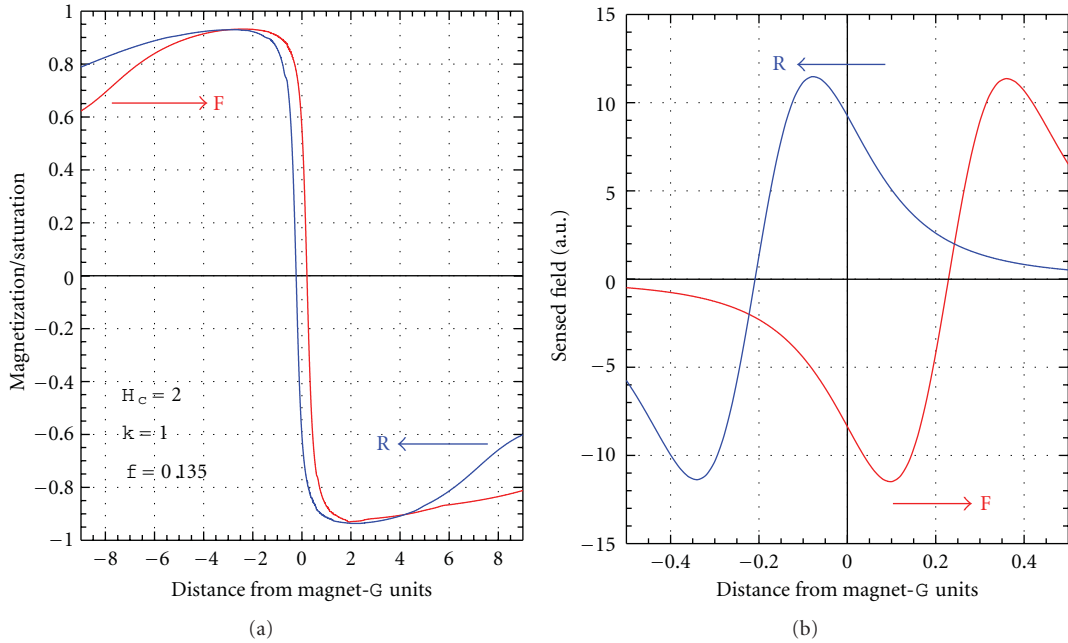
FIGURE 5: (a) Variation of M at the sensor position during forward (F) and reverse (R) motion. (b) Corresponding sensed field = $\nabla(\nabla \cdot M(0)_F)$ and $\nabla(\nabla \cdot M(0)_R)$.

variations of $M(0)_F$ and $M(0)_R$ with magnet position are shown in Figure 5(a), with the central regions of $\nabla(\nabla \cdot M(0)_F)$ and $\nabla(\nabla \cdot M(0)_R)$ shown in Figure 5(b). The starting points in Figure 5(a) are not exactly the same as the numbered points in Figure 4. This is because the field at the end of the motion in either direction does not reach zero at any finite values of x. Figure 4(a) presumes that the value of

x at the motion extrema is large enough for the field starting and finishing points to be close enough to zero. In contrast, the start (and finish) of the plots (but not the motion) in Figure 5 clearly occur at finite (± 8.8 G) distances from the sensor. Thus the end of the plot in one direction does not have the same magnetization as the start of the plot in the opposite direction.

(a)

(b)
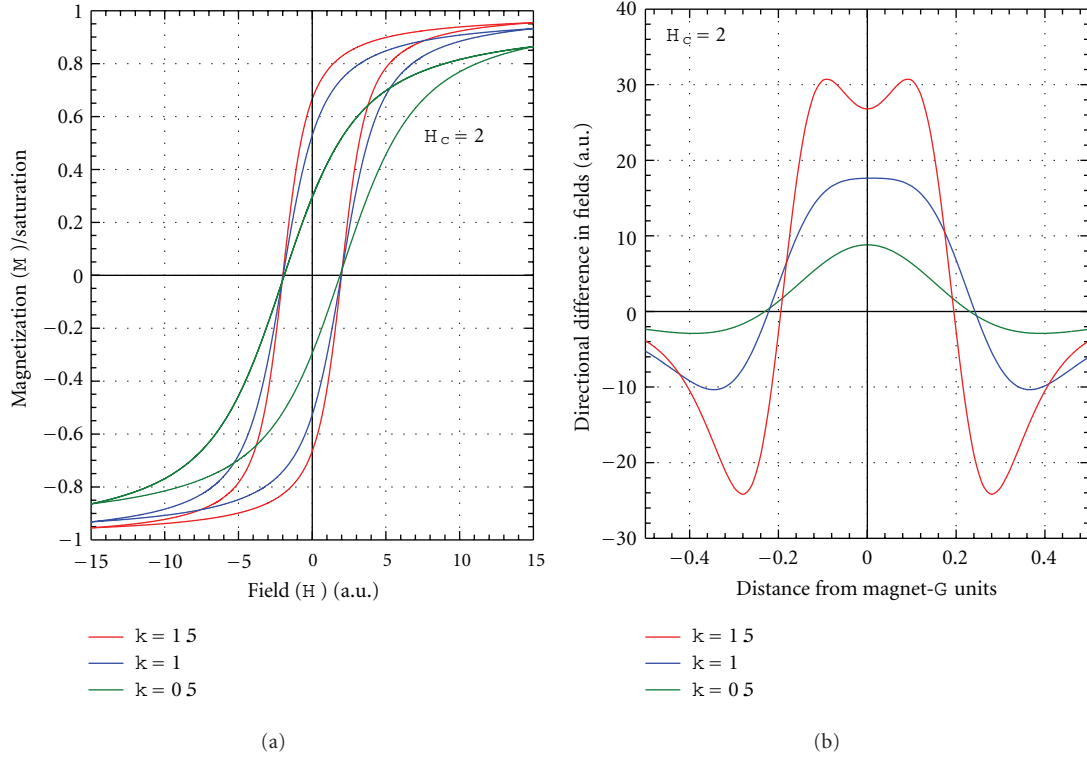
FIGURE 6: (a) Hysteresis Loops for constant H_c, variable k values. (b) Resulting $D(x)$.

Major hysteresis loops created from (4) and (5) for the values of H_c and k indicated are shown in Figures 6(a) and 7(a). Resultant values of $D(x)$ are shown in Figures 6(b) and 7(b). The sizes of the central positive peak and the symmetrical negative peaks are seen to vary directly with the loop squareness, peak M, and H_c, as does hysteresis loss.

3. Experimental

An experimental apparatus was set up on a vertical milling machine, thereby conveniently accommodating a variety of experimental conditions, including SUT size (width, thickness, and length), field sensor position relative to the SUT edge, length of Stroke and center position relative to the field sensor, adjustability of both the space between the magnet face and SUT (dimension b in Figure 1), and the location of the magnet relative to the field sensor centerline. An Allegro 3515 UA Hall effect field sensor (sensitivity = 0.0628 mV/A/m), with d (Figure 1) = 1.62 mm, was mounted just below (~0.05 mm) the mounting surface of the SUT. Nd-Fe-B magnets of a variety of sizes and energy levels were mounted into aluminum holders having common mounting features (a 9.5 mm diameter × 20 mm long cylindrical portion) to allow easy interchangeability in the machine spindle.

Except that the magnet was stationary while the SUT/ field sensor combination (being mounted on the milling machine table) were the movable elements, operation of the apparatus followed the description in the Introduction.

For each magnet and gap combination, $H_L(x)$ was first measured without any SUT. The comparative amplitudes, $\pm H_{L\text{Peak}}$ for the various magnet/"gap" (G in Figure 1) combinations were used to gain understanding on how these parameters affect the later test results. On the basis of the plot of (1) in Figure 3, together with assumption 2, G was presumed to be the distance between $\pm H_{L\text{Peak}}$. Measurements of this distance with two or more different physical gaps allowed both the location of the equivalent dipole ("a" in Figure 1(b)) and the dipole moment to be calculated.

Values of $D(x)$, calculated from measurements of $H_F(x)$ and $H_R(x)$ for the samples and magnet indicated, are plotted in Figures 8 and 9. The most salient features of the plots are seen to match the prediction of the analysis. Moreover, since losses in electrical steels are in approximate proportion to their grade number, and the drastic reduction in coercivity by annealing of cold worked steels is common knowledge, these plots verify the theoretically expected correlation between the amplitude of the signature features and the factors contributing to hysteresis loss. The nominal coercivity values of the three samples shown in Figure 8 are 100 A/m, 45 A/m, 35 A/m for the 800-50, 350-50, and the 290-50, respectively. Comparison with Figure 8 teaches us that there is indeed a larger difference between the 800-50 and the 350-50 than between the 290-50 and the 350-50.

The versatility of the described method was shown by its use to measure the relative losses in regions near the cut edges of strip samples of the 350 and 800 grades. The SUT was placed with the edge being examined ~1 mm over the center
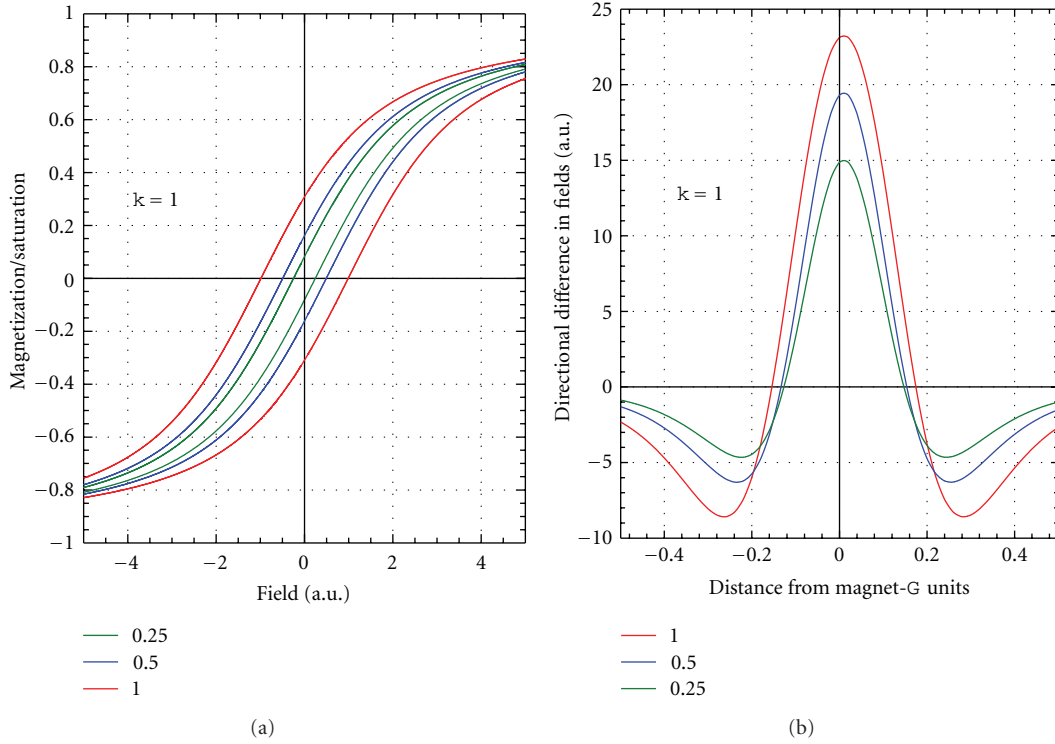
FIGURE 7: (a) Hysteresis Loops for constant k, variable H_c values. (b) Resulting $D(x)$.
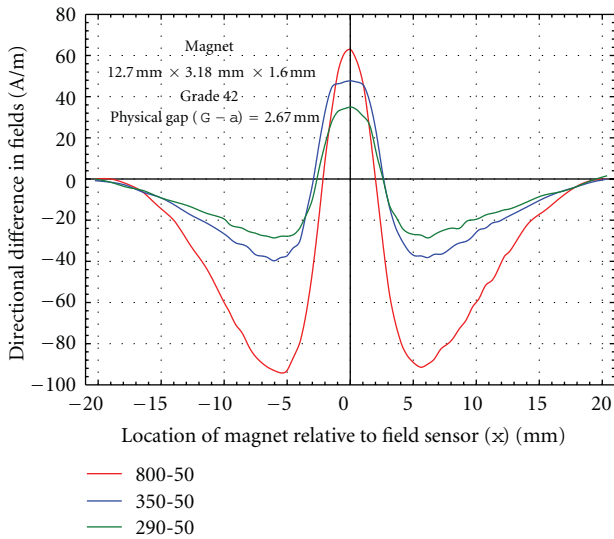
FIGURE 8: $D(x)$ from measured values of $H_F(x)$ and $H_R(x)$ for the 3 grades of NO Si steels indicated.

FIGURE 9: Same as Figure 8 for 0.61 mm thick cold rolled AISI 1010 in as-received and annealed conditions.

of the field sensor. A magnet, 3.18 mm square by 12.7 mm long (in the direction of m) was positioned 1 mm back from the edge and 2.5 mm above the SUT. $D(x)$ measurements on 2 samples each, cut by a fast moving laser, averaged 40% (350 grade) and 14% (800 grade) less than those cut more slowly, in good agreement with results from other measurement methods [4].

The more compact spacing of the signature features predicted in the analysis than those experimentally observed

is attributed to several critical but enormously complicating factors being ignored in the analysis; namely, the interaction between the magnetization and the generated fields and the gradients in these throughout the SUT thickness. Nevertheless, the model correctly shows that the magnetization gradients are different for the two directions of motion, a difference founded on the double-valued M-H relationships which manifest "hysteresis." We also ignored in this paper the effects of sample thickness, distance of the field sensor from

the sample surface, possible effects of the circuit permeance on the field from the magnet, and so forth. However, a significant contributor to the less compact detected field difference profile is this interaction of the $\nabla \cdot M$ fields with the M fields.

This paper proposes an experimental method for locally assessing hysteresis properties, and a theoretical basis is given for explaining the obtained difference curves. The correlation between the experimentally obtained Figure 8 and Figures 7(a) and 7(b) shows that indeed the difference curves are correlated with the hysteresis losses. The same correlation was observed with Figure 9. The results in this paper are qualitative, and by refinement of the numerical model for explaining the difference curves we can aim in further work to more quantitative assessment of hysteresis properties and losses. The numerical model can be refined by, for example, taking into account the thickness of the sample under study so to have a more correct explanation of the measurements. The method we describe does give quantitative results. We do not claim, however, that the quantitative description of salient features of $D(x)$ plots have translatable correlations with quantitative descriptions of salient features of B-H plots.

A possibility to more quantitative studies is to determine the input model parameters (i.e., k, H_c, and f) starting from directly measured B-H loops. Also, more advancements are needed in the theory for better understanding the $D(x)$ measurements. For instance, sensitivity analysis can help us in better understanding the measurements by looking at how the variation in one parameter affects the $D(x)$.

4. Conclusions

In this paper, we propose a unique methodology together with its modus operandi and important experimental results. Both analytical and experimental results convincingly show the signature features of the difference measurements $D(x)$ to be reflective of those same properties of test sample material, which are the underlying determinants of the size, shape, and intercept features of conventional hysteresis loops. As such, and considering both the rapidity and sensitivity by which $D(x)$ measurements might be obtained with purposefully constructed apparatus of obvious simplicity, the utility of the described method for comparative evaluations by nondestructive means, of factors affecting hysteresis properties, seems well established. The proposed technique has the possibility to assess in detail the relationships between microstructure (or internal stress) and magnetic performance.

References

[1] M. Emura, M. F. de Campos, F. J. G. Landgraf, and J. C. Teixeira, "Angular dependence of magnetic properties of 2% silicon electrical steel," *Journal of Magnetism and Magnetic Materials*, vol. 226–230, part 2, pp. 1524–1526, 2001.

[2] E. G. Araujo, J. Schneider, K. Verbeken, G. Pasquarella, and Y. Houbaert, "Dimensional effects on magnetic properties of fesi steels due to laser and mechanical cutting," *IEEE Transactions on Magnetics*, vol. 46, no. 2, pp. 213–216, 2010.

[3] G. Crevecoeur, P. Sergeant, L. Dupré, L. Vandenbossche, and R. Van de Walle, "Analysis of the local material degradation near cutting edges of electrical steel sheets," *IEEE Transactions on Magnetics*, vol. 44, no. 11, pp. 3173–3176, 2008.

[4] I. J. Garshelis, G. Crevecoeur, S. P. L. Tollens, and L. Dupre, "Application of the drag force method to evaluate magnetic property degradation near the cut edges of electrical steels," *Journal of Applied Physics*, vol. 109, no. 7, Article ID 07E518, 2011.

[5] B. D. Cullity, *Introduction to Magnetic Materials*, Addison-Wesley, Reading, Mass, USA, 1972.

Research Article

Health Monitoring for Coated Steel Belts in an Elevator System

Huaming Lei,[1, 2] Guiyun Tian,[2] Hui Zhao,[1] Yimei Mao,[1] and Zuoying Huang[1]

[1] *Department of Instrument Science & Engineering, Shanghai Jiaotong University, Shanghai 200204, China*
[2] *School of Electrical, Electronic & Computer Engineering, University of Newcastle, Newcastle NE1 7RU, UK*

Correspondence should be addressed to Huaming Lei, hmlei@sjtu.edu.cn

This paper presents a method of health monitoring for coated steel belts in an elevator system by measuring the electrical resistance of the ropes embedded in the belt. A model on resistance change caused by fretting wear and stress fatigue has been established. Temperature and reciprocating cycles are also taken into consideration when determining the potential strength degradation of the belts. It is proved by experiments that the method could effectively estimate the health degradation of the most dangerous section as well as other ones along the whole belts.

1. Introduction

Elevator systems usually include a car and a counterweight (CW) which are suspended by tension members. A hoisting motor drives the tension members to lift the car to the desired levels within a hoistway as shown in Figure 1. Traditionally, steel ropes were used. More recently, coated steel belts have been introduced, which have a plurality of steel rope encased in a polyurethane jacket [1, 2]. The usage of coated steel belts has several merits, such as high abrasion resistance, good flexibility and maintainability, long lifespan, low space occupation, and low noise.

With the introduction of the belts, new monitoring techniques should be developed to keep elevator systems working safely. The primary source of belts strength degradation is the cyclic bending around sheaves when the elevator is moving up and down in an elevator shaft. The tension support strength degradation is normal not uniform along the length of the belts. Those areas subject to high level or severities of bending cycles will degrade faster than areas experiencing fewer bending cycles. The two most frequent degradation forms are diameter diminution of the cords and wire broken caused by fretting wear and stress fatigue damage. This would lead to the resistance change and imply that measuring the resistance could estimate the possible degradation for the belts. Fortunately, the structure of belt ensures the possibility and convenience of measuring resistance as there is an insulating jacket and multiwire encased in the jacket. As long as some ropes were shorted at one end of the belt through a special connector, resistance could be measured at the other end.

2. Modeling of Health Degradation

Two basic mechanisms, fretting wear and stress fatigue damage, would cause the increasing of electrical resistance for a metallic rope. Fretting wear usually refers to the diminution in cross-sectional area of metal caused by fretting friction among the ropes. As matter of course, cross-sectional area changes of wires will naturally lead to changes in resistance. On the other hand, stress fatigue damage would cause resistance increasing based on the fact that the germination of microcracks within the material would affect the electrical conductivity [3, 4].

2.1. Modeling of Fretting Wear. It is quite complicated to model the fretting wear of interwire contact between wires in a rope. The wear rate is related to the contact pressure, sliding velocity, material hardness, and so on. A large number of wear models were developed in the past [5–7]. The most common wear model can be expressed by the following mathematical equation, called the Archard's law [6]:
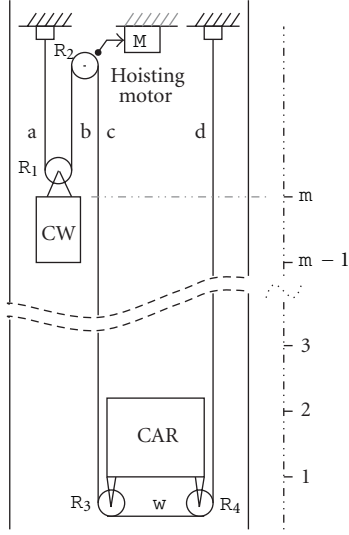
$$\frac{dw}{ds} = kp. \tag{1}$$

FIGURE 1: Schematic diagram of an elevator system.

Here, w is the linear wear, known as, the worn volume per unit apparent contact area, p is the contact pressure, k is the dimensional wear coefficient, and s is the sliding distance.

When p is assumed to be a constant, formula (1) indicates that the wear is linearly proportional to the contact pressure p in one cycle. For multicycles, the wear is linearly proportional to the number of cycles.

The belts working as tension members in an elevator system would experience two kinds of loading as axial loading and bending over sheaves. The interwire contact pressures are quite different in these two circumstances. In straight ropes the contact pressures are determined by axial loading and in bending ropes additional contact pressure would generate which depends on the diameter ratio of sheave and ropes. Based on the assumption that the maximum additional contact pressure induced due to bending of the wire rope over a sheave is proportional to axial loading, the fretting wear due to axial loading and bending could be, respectively, expressed as

$$
\begin{aligned}
w_0 &= 2\Delta x_0 k p_0 n_0, \\
w_b &= 2\Delta x_b k p_b n_b.
\end{aligned}
\tag{2}
$$

Here, Δx is the stroke of cycles, and n is the reciprocating cycles. The subscripts 0 and b indicate the parameters are concerned with the axial loading and bending, respectively.

2.2. Modeling of Stress Fatigue Damage.

When a cyclic loading is acting on metal components, fatigue microcracks would generate within the material. Fatigue damage evolution rate and cycle-creep rate are generally assumed to be functions of stress σ, damage D, and temperature T. The damage value can be approximately expressed as [3, 4, 7, 8]

$$
D = 1 - \left[1 - \frac{n}{N}\right]^{1/(r(\beta)+1)},
\tag{3}
$$

where n is the number of reciprocating cycles and N the lifespan under the specific cyclic loading. The $r(\beta)$ is a function of β and material and temperature independent. β is the ratio of minimum stress and maximum stress during a cycle.

If the material experiences more than one kind of load and ignores the loading sequence, the damage D could be written as

$$
D = 1 - \left[1 - \frac{\sum_i n_{ei}}{N}\right]^{1/(r(\beta)+1)},
\tag{4}
$$

where,

$$
n_{ei} = N\left\{1 - \left(1 - \frac{n_i}{N_i}\right)^{(r(\beta)+1)/(r(\beta_i)+1)}\right\},
\tag{5}
$$

n_i is the number of cycles associated with the ith type of loading, and N_i and β_i are the corresponding lifespan and ratio. Formula (5) is derived based on equivalent damage principle.

2.3. Resistance Change Caused by Damage.

When fretting wear or fatigue damage happens, it indicates the diameter of rope becoming smaller and micro-cracks producing within the wires and results in resistance increasing. The resistance is determined by the effective cross-sectional area of the ropes. Assuming the fretting wear and fatigue damage occurred evenly along the section which experience the same loading, the resistance before and after experiencing the loading can be written as [3, 4, 8]

$$
\begin{aligned}
R_0 &= \frac{\rho L}{A_0}, \\
R &= \frac{\rho L}{A_0(1 - D_t)},
\end{aligned}
\tag{6}
$$

where A_0 is the cross-sectional area and L is the length of section being researched. A_0 is a coefficient related to the cross-sectional area reduction. Obviously, the coefficient D_t is an indication of the total damage caused by fretting wear and stress damage, it is written as

$$
D_t = D + \frac{w}{\Delta x A_0}.
\tag{7}
$$

From (6), D_t could be expressed as

$$
D_t = \frac{\eta}{(1 + \eta)},
\tag{8}
$$

where η is the resistance change rate, defined as $\eta = \Delta R/R_0 = (R - R_0)/R_0$.

From (7), the total damage could be written as

$$
D_t = 1 - \left[1 - \frac{\sum_i n_{ei}}{N}\right]^{1/(r(\beta)+1)} + q_0 n_0 + q_b n_b,
\tag{9}
$$

where the q_0, q_b are wear coefficients concerned with the number of reciprocating cycles. As the resistances were measured for a specified section after the section experienced different reciprocating cycles, the parameters in (9), such as $r(\beta_i)$, N_i, q_0, and q_b, could be solved by combining the (8) and (9).

Section (m)	0	2.5	4.5	5.8	9.1	11.1	12.4	17.7	18.9	20.5	22.2	23.8	24.3	25.5	27.1	28.8	30.4	35.4	Parameters to be determined
Sheave1			16	18	12														$w_{b1}, N_1, r(\sigma_1)$
Sheave2				16		18	12												$w_{b2}, N_2, r(\sigma_2)$
Sheave3								16	18	12									$w_{b3}, N_3, r(\sigma_3)$
Sheave4										16		18	12						$w_{b4}, N_4, r(\sigma_4)$
Axial loading								21											$w_{b0}, N_0, r(\sigma_0)$
Parking records	$1 \rightarrow 2$ 2×10^4 $2 \rightarrow 3$ 1×10^4 $3 \rightarrow 3$ 1×10^4 $1 \rightarrow 3$ 6×10^4 $1 \rightarrow 4$ 8×10^4 $2 \rightarrow 4$ 3×10^4																		$x \rightarrow y$ means from x^{th} floor to y^{th} floor

Figure 2: Sections division and the number of bending cycles (10^4).

2.4. Degradation of a Whole Steel Belt. As mentioned before, the strength degradation is normally not uniform along the whole length of the belt. Those areas subject to high level or severities of bending cycles will degrade faster than areas experiencing fewer bending cycles. Belts working in an elevator system could be divided into several sections according to the parking operation. The electrical resistance of a whole rope within the belt after a certain operating could be written as

$$\Delta R = \frac{R_0}{L} \sum_k \eta_k L_k = \frac{R_0}{L} \sum_k \frac{D t_k}{1 - D t_k} L_k. \quad (10)$$

Here, the subscript k represents the serial number of segments.

In order to determine damage of the every section and distinguish the most dangerous segment, a couple of resistance measurements should be conducted once the belt experiences a certain amount of reciprocating cycles. Thus, the parameters in (10) could be estimated by the least squares fitting method according to the following formula:

$$\min \sum_j |\Delta R_{\text{test}} - \Delta R|^2$$
$$s.t. \sum_k L_k = L. \quad (11)$$

Here j is the serial number of measurements. Once the parameters are obtained, the damage of each section could be calculated according to formula (9).

3. Method for Section Division

As the elevator runs up and down in the shaft for a long period, different parts of belts would suffer different number of cycles which could be obtained from the parking records of the elevator. Some parts may experience bending only on one sheave, some may do on more than one sheave, and some would never suffer bending. Those parts experiencing the same axial loading or bending are separated as one section. The whole belt could be theoretically divided into different sections according to the structure dimension of the elevator system. Figure 2 gives an example of the sections division

according to Figure 1 and the number of suffering from bending is listed. Here, the parameters are as $a = 2.5$ m, $b = 2$ m, $c = 4.5$ m, $d = 5$ m, $w = 1.6$ m, $h = 3.3$ m, and the total number of floor $m = 4$. The variable h presents height from floor to next floor.

From the results, it could be seen that different sections may suffer bending from different sheaves with different cycles. Those sections, such as [20.5–22.2], [23.8–24.3], would experience bending on more than one sheave. It could be anticipated that these sections may suffer more damage than others and become the most dangerous segments along the belt. The quantity of the damage could be estimated once obtaining the parameters by solving (11).

4. Experiment and Results

It would be a long-term work to conduct the experiment in a normal elevator system because the fretting wear and damage grow quite slowly even more than 30 years. In order to verify the effectiveness of the method, accelerated fatigue experimental work was conducted on a belt of length 5.541 m and with 6 core ropes whose diameter is 2.3 mm. The loaded belt experienced repeated bending on two sheaves with the diameter 110 mm and approximate contact angle 90 degrees. Figure 3 shows the schematic diagram of mechanical structure for fatigue experiment.

Temperature was recorded as well as the resistance in the experiment. It is found that the TCR (temperature coefficient of resistance) of the belt would not change after fatigue experiment. This is an important result for estimating damage under different temperature. The temperature and TCR are used to rectify the electrical resistance and get an identical evaluation criterion under an assumed temperature.

The resistances for one of the ropes that experienced different cycles were measured by a high-accuracy multimeter at temperature 26°C. The parameters were estimated by (11) and the estimated resistance curve is shown in Figure 4 compared with the measured data. By using the parameters, the damage for each section could be calculated. As a contrast, the resistances of each section were measured after 100,000 cycles. The calculated resistance is in good agreement with the actual measured ones as shown in Table 1. The measured $\Delta R/R_0$ rate is in good agreement with the inferred damage D_t.

TABLE 1: Data of fatigued belts according to different sections.

Segment no.	I	II	III	IV	V	Tot. or aver.
Length L (m)	2.279	0.478	0.461	0.486	1.837	5.541
Resistance R (mΩ)	217.3	46.5	48.3	47.8	175.2	535.1
Pre-fatigued R_{0i} (mΩ)	216.1	45.3	43.7	46.1	174.2	525.4
Measured ΔR (mΩ)	1.2	1.2	4.6	1.7	1.0	9.7
Normalized R (mΩ/m)	95.35	97.26	104.81	98.32	95.37	96.57
Measured $\Delta R/R_0$ (%)	0.56	2.65	10.53	3.69	0.57	1.85
Inferred ΔR (mΩ)	—	1.41	4.59	1.44	—	7.44
Inferred Damage D_t (%)	—	3.03	9.51	3.03	—	—
Condition			$R_0 = 94.83$ mΩ/m at temperature T_0 (26°C).			

Center distance: l = 430 mm

Contact angle: = 90°

Sheave diameter: D = 110 mm

Rope diameter: d = 2 3 mm
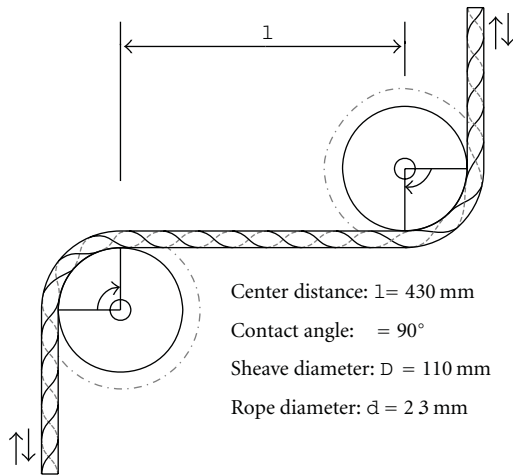
FIGURE 3: Mechanical structure diagram for fatigue experiment.

FIGURE 4: The estimated curve of the damage and the change of resistance for the belts.

On the condition that the belt is working under normal condition and will not suffer occasional injure, such as sharp twisting or hammer hitting, the presented method is effective and reliable for the damage evaluation and life prediction. Furthermore, from the measured $\Delta R/R_0$, it can be inferred that the fretting wear and stress damage that acted on section II and section IV of the two sheaves are not exactly the same. This may be attributed to the inconsistent installation of the two sheaves.

5. Conclusions

An inspection and health monitoring method for steel wire belts is presented and proved by fatigue experiment. It is an effective method to monitor the stress degradation for belts by measuring the electrical resistance of the embedded rope. It should be noted that the established model is based on a lot of assumptions and ignores the loading sequence. The fatigue experiment is built on an accelerated aging setup, which leads to that most of the change in resistance may be caused by stress fatigue. Although, in an elevator system, the belts experience high-cycles fatigue, resistance increase caused by fretting wear may take the dominant role. All these should be considered more carefully in an actual application for elevators. In the future, more efforts would be put on

using the magnetic flux leakage or eddy current methods to test the belts, and results will be compared with the inferred damage, to make the presented model more applicable.

References

[1] P. Wesson John and R. Gurvich Mark, "Method of making an elevator belt," WIPO Patent Application, WO/2010/056247 A1. 2010.

[2] Y. Konishi, A. Ueno, A. Wake, and K. Yuasa, "Elevator drive belt [p]," WO-02/064482. 2004.10.

[3] W. June, "A continuum damage mechanics model for low-cycle fatigue failure of metals," *Engineering Fracture Mechanics*, vol. 41, no. 3, pp. 437–441, 1992.

[4] J. Jusheng and X. Jinquan, "The research of damage in fatigue by means of resistance of metal materials," *Journal of Mechanical Strength*, vol. 21, pp. 232–234, 1999.

[5] I. I. Argatov, X. Gómez, W. Tato, and M. A. Urchegui, "Wear evolution in a stranded rope under cyclic bending: implications to fatigue life estimation," *Wear*, vol. 271, no. 11-12, pp. 2857–2867, 2011.

[6] A. Cruzado, M. Hartelt, R. Wäsche, M. A. Urchegui, and X. Gómez, "Fretting wear of thin steel wires. Part 1: influence of contact pressure," *Wear*, vol. 268, no. 11-12, pp. 1409–1416, 2010.

[7] D. K. Zhang, S. R. Ge, and Y. H. Qiang, "Research on the fatigue and fracture behavior due to the fretting wear of steel wire in hoisting rope," *Wear*, vol. 255, no. 7–12, pp. 1233–1237, 2003.

[8] P. Starke, F. Walther, and D. Eifler, "PHYBAL—a new method for lifetime prediction based on strain, temperature and electrical measurements," *International Journal of Fatigue*, vol. 28, no. 9, pp. 1028–1036, 2006.

Research Article

Eddy Current Transducer Dedicated for Sigma Phase Evaluation in Duplex Stainless Steel

Grzegorz Psuj,[1] Tomasz Chady,[1] and Cesar Giron Camerini[2]

[1] *Department of Electrical and Computer Engineering, Faculty of Electrical Engineering, West Pomeranian University of Technology, al. Piastow 17, 70-310 Szczecin, Poland*

[2] *Laboratory of Nondestructive Testing, Corrosion and Welding, Department of Metallurgical and Materials Engineering, Federal University of Rio de Janeiro, 21941-596 Rio de Janeiro, RJ, Brazil*

Correspondence should be addressed to Tomasz Chady, tchady@zut.edu.pl

The paper describes a new transducer dedicated for evaluation of a duplex stainless steel (DSS). Different phases which exist in DSS have influence on mechanical as well as on electrical properties. Therefore, an eddy current transducer was utilized. In order to achieve high sensitivity, a differential type of the transducer was selected. The performance of the transducer was verified by utilizing the samples which had a different amount of sigma phase.

1. Introduction

The duplex stainless steel (DSS) has been widely used in various industries, mainly because of good combination of mechanical properties and high corrosion resistance presented in this material [1, 2]. The DSS properties are determined by the presence of two phases in microstructure having very different physical properties: ferrite (δ) and austenite (γ). The austenite presents high electric conductivity and low magnetic permeability, while the ferrite presents low electric conductivity and high magnetic permeability. The best properties of DSS can be achieved when the phases δ and γ are in equal proportions. In many cases production techniques of DSS pipes involve welding operation, which may lead to microstructural changes in the base metal and heat-affected zone (HAZ). Exposition to temperatures ranging from 300°C to 1000°C can cause changes of balance of the phases and/or precipitation of deleterious phases. The most harmful of the deleterious phases that can be originated in the material microstructure is sigma (σ) phase. It presents higher than other phases volumetric fraction. Its precipitation causes chromium depletion in the adjacent regions, impairing dramatically mechanical and corrosion properties of the material [1–4].

The presence of σ phase also causes changes of the electromagnetic properties of DSS. The ferrite is ferromag-netic while austenite and sigma phase are paramagnetic. Thus, an increase of the sigma phase and the resulting decrease of the ferrite phase volumetric fraction render the material behavior more paramagnetic [5]. This phenomena motivates to use an eddy current testing (ECT) method for the detection of material degradation caused by an increased presence of the sigma phase.

2. Eddy Current Transducer and Measuring System

In the preliminary experiments various configurations of the transducers were considered and tested. In order to distinguish small differences of the electric parameters, the transducer operating in a differential mode was selected. The transducer presented in this paper was build using an H-shape ferrite core. Such shape of the ferrite allows to achieve higher density of the flux inside the material. Three-dimensional model of the transducer and a cross-section view with dimensions is shown in Figure 1. Photos of the transducer are shown in Figure 2.

The transducer has a single excitation coil and two pick-up coils. The main pick-up coil works in the neighborhood of a tested material having different amount of σ phase. In the same time the reference pick-up coil is in the vicinity
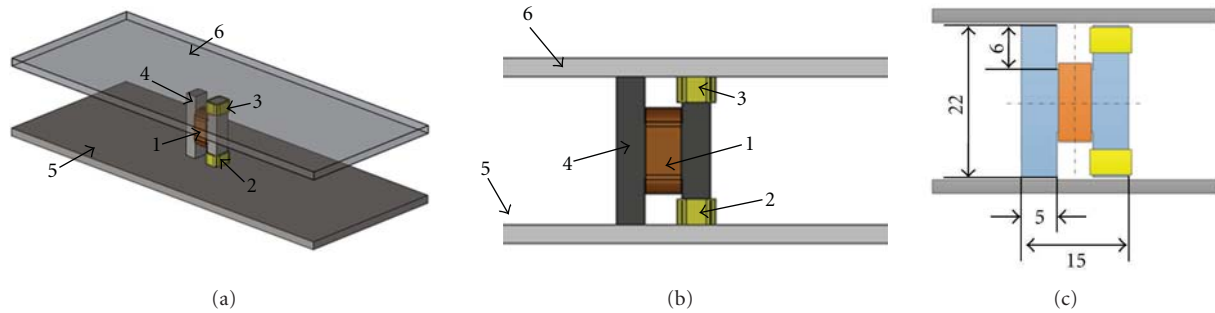
FIGURE 1: Views of the transducer: (a) three-dimensional view, (b) cross-section view, (c) view with dimensions (all given in mm); 1: excitation coil, 2: main section pick-up coil, 3: reference section pick-up coil; 4: ferrite core; 5: testing sample; 6: reference sample.
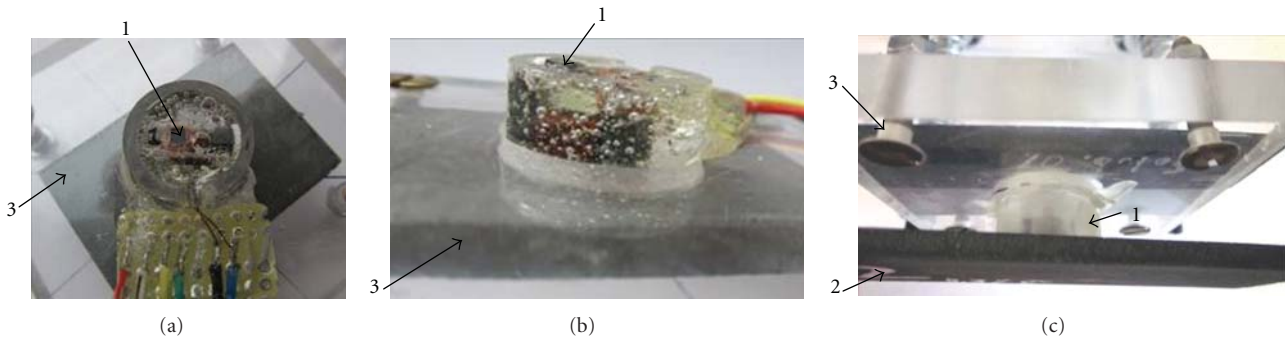
FIGURE 2: Photos of the transducer: (a) bottom view, (b) side view, (c) transducers over testing sample; 1: transducer, 2: testing sample, 3: reference sample.
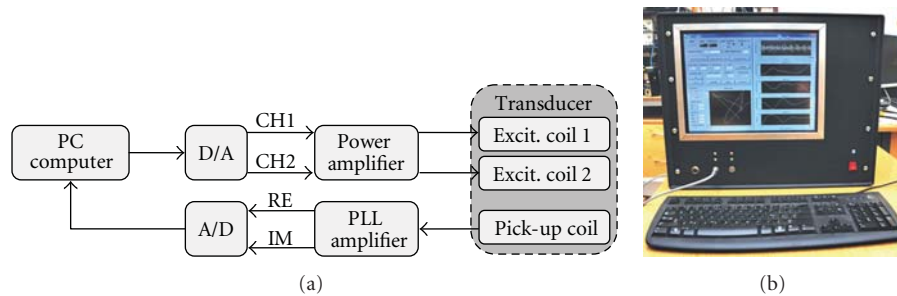
FIGURE 3: Block scheme (a) and photo (b) of the measuring system.
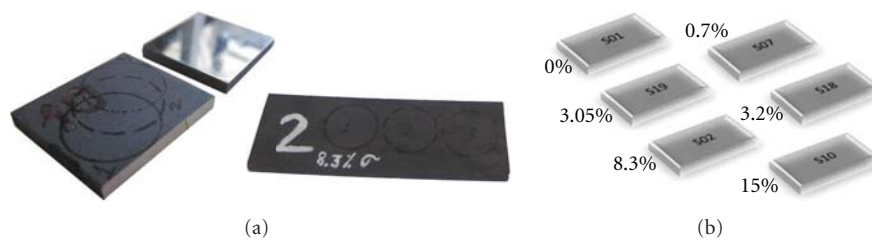
FIGURE 4: Testing DSS samples containing different amount of σ phase: (a) photo of the samples, (b) view of the samples.

of the sample without σ phase. The excitation coil is driven by power amplifiers. Pick-up coils of both sections are connected differentially so in the case of testing material without σ phase the measured signal is close to zero. The σ phase presence is causing the nonzero differential output voltage. However, the amplitude of the output voltage is relatively low (a few millivolts). Therefore, a lock-in amplifier that is commonly used to detect and measure very small AC signals [6] was utilized. The block scheme of the measuring system is presented in Figure 3. The system enables to carry

Amplitude of the measured signal $|U(x, y)|$

Phase of the measured signal $\varphi(x, y)$

(a)

(b)

(c)

(d)

(e)
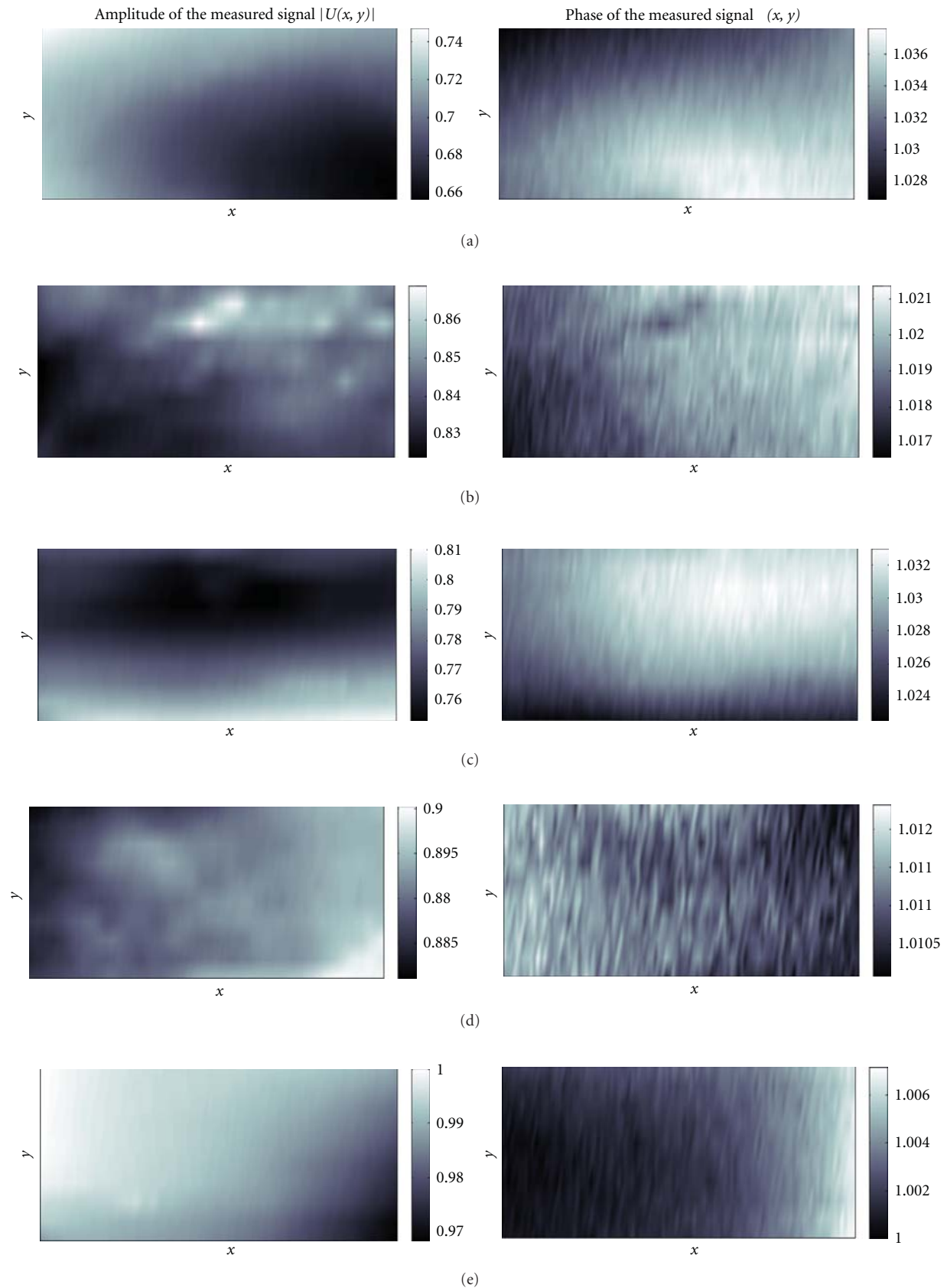
FIGURE 5: Results of two-dimensional scans obtained for samples: (a) S07 comprising of 0.7% of σ phase, (b) S19 comprising of 3.05% of σ phase, (c) S18 comprising of 3.2% of σ phase, (d) S02 comprising of 8.3% of σ phase, and (e) S10 comprising of 15% of σ phase.
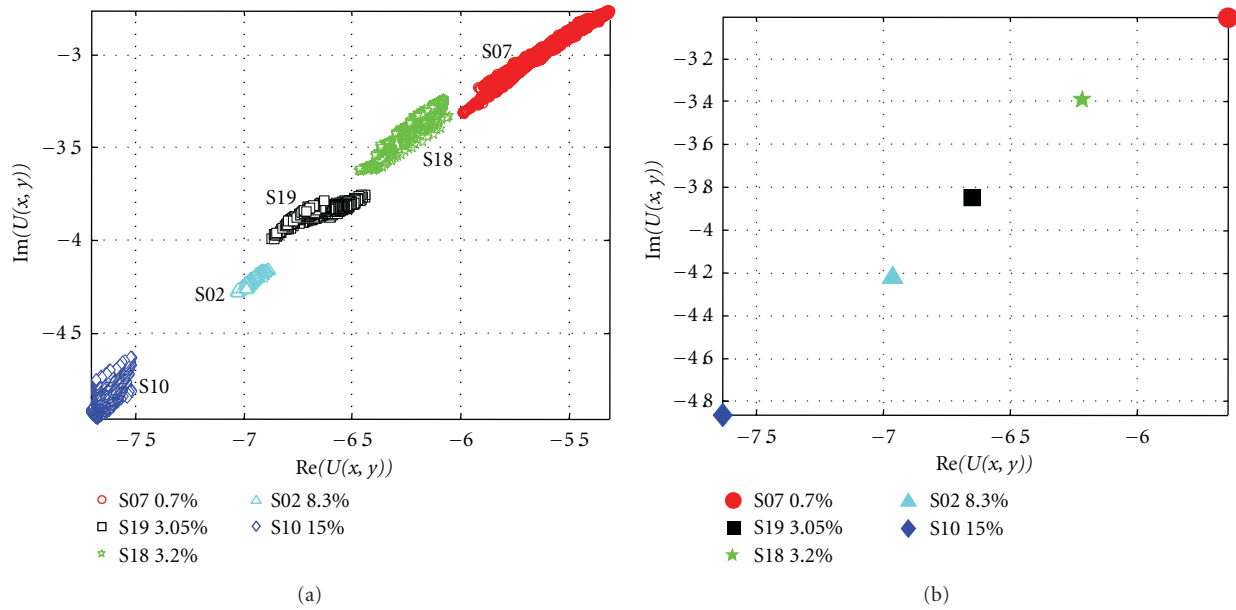
FIGURE 6: Results of two-dimensional scans obtained for samples comprising different amount of σ phase presented in the complex plain: (a) distributions of measured signals in selected areas for each sample, (b) mean values of results presented in plot (a).

on measurements using testing frequency ranging from 1 kHz up to 100 kHz. The main part of the system is a pick-up signal block where measured signal is extracted and amplified by a programmable lock-in amplifier. Signals generation and acquisition is carried out by multifunction data acquisition (DAQ) board. The DAQ device is controlled via USB interface by an embedded compact computer.

3. Testing Samples

Six DSS samples (specification UNS 31803) shown in Figure 4 were used to evaluate the proposed transducer. All samples were submitted to a preliminary solution heat treatment (Sol.) with the goal to obtain a balance of approximately 50% between both phases, ferrite (δ) and austenite (γ). The solution heat treatment was conducted at 1120°C during one hour, followed by water quenching. Five samples received further aging heat treatments (Table 1) which introduced different amounts of sigma phase (σ). The content of sigma phase was evaluated by utilizing scanning electron microscope (SEM) to different selected parts of the samples. To determine the amount of sigma phase, a small sample of DSS is placed into SEM. Fifty images are taken from different regions of the sample. Each image is processed using the commercial software ImagePro, and the phases are counted following the standard ASTM E1245-03. After the analysis of the 50 images, the mean and standard deviation value is extracted. One sample (S01) remained without aging and was used as a reference.

4. Results of Measurements

All samples were measured in the same way. The transducer was scanned over the sample's surface in two perpendicular directions over the area with dimensions 10×30 mm. Due to the large surface roughness, the transducer could not be in direct contact with the test sample, and lift-off had to be set. The impact of surface conditions on the results was verified using sample with only one side polished. Measured signal's parameters obtained for polished side with no lift-off and for unpolished side with lift-off of 0.5 mm were comparable, therefore further measurements were carried out for lift-off of 0.5 mm. During the movement of the transducer, the output signal was measured. Two-dimensional distributions of the signals' amplitude and phase are shown in Figure 5. The 2-D plots illustrate spatial distribution of the material properties. One can observe that all the samples are not uniform, and the achieved results vary between measuring points. This can be explained by the fact that the contents of sigma phase vary in the tested area of samples, even taking upon consideration the areas of a few square μm, which is much less than the dimensions of the transducer.

The scale of changes of the amount of sigma phase in samples was evaluated by the SEM technique. The standard deviation of the percentage of sigma phase obtained for different samples was reaching values even between 0.5% and 1%. Considering this, proper evaluation and then drawing a distinction between samples comprising a similar amount of sigma phase can be hard to achieve. That is confirmed by the results obtained for S19 (3.05%) and S18 (3.2%). Therefore, in order to maximize the possibility of proper evaluation of sigma phase, the results achieved in all measured points were averaged for each sample. In order to compare results, common plots in a complex plane are provided (Figure 6). The distribution of the measured values presented in Figure 6(a) proves that the samples with different amount of the sigma phase (σ) can be easily distinguished. The plot of averaged values (Figure 6(b)) shows that there is a linear

(a)

(b)

(c)

(d)

(e)

(f)

(g)

(h)
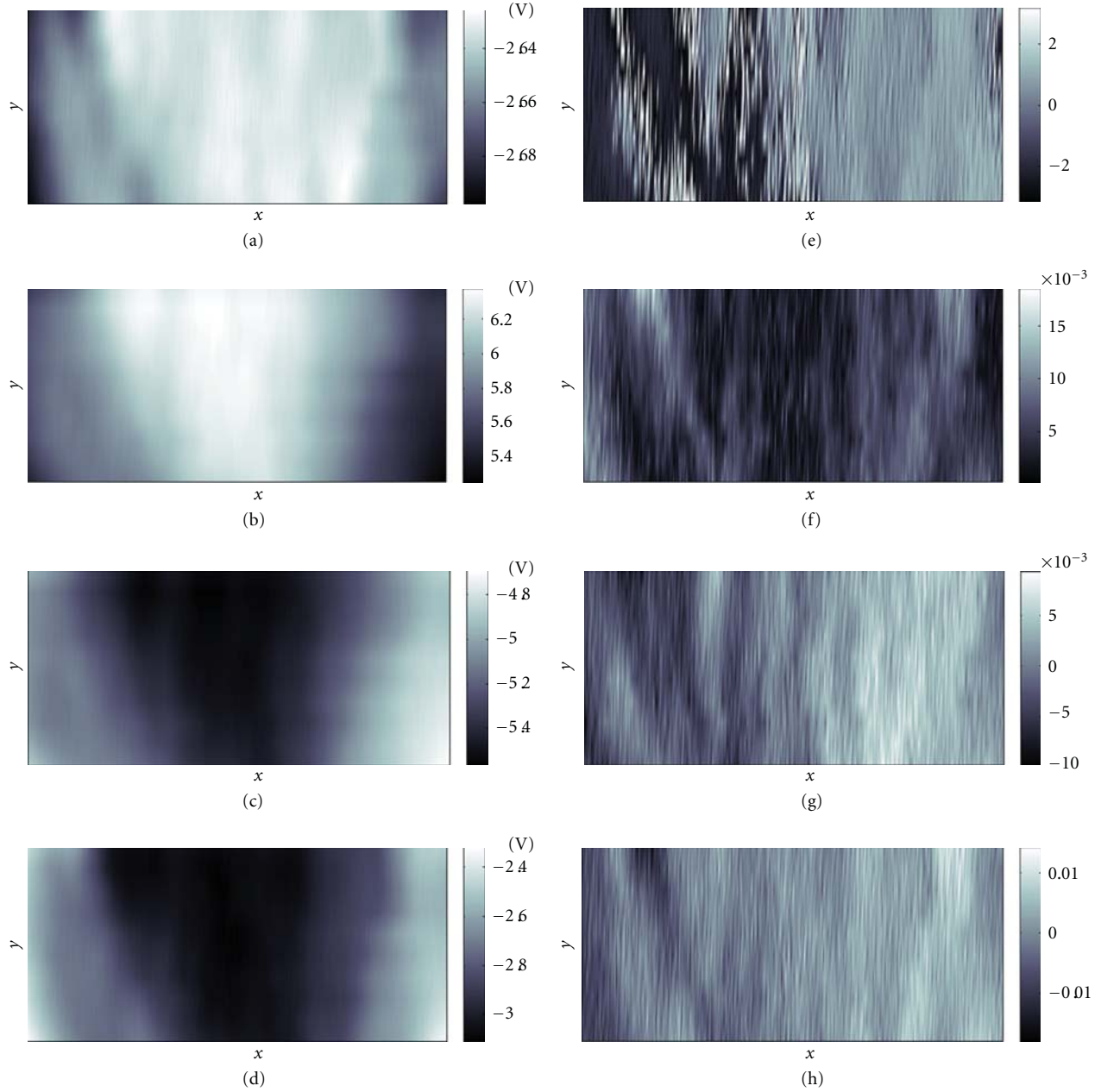
FIGURE 7: Results of two-dimensional scans obtained for sample with weld: (a) amplitude of measured signal $|U(x, y)|$, (b) phase of measured signal $\varphi(x, y)$, (c) real part of measured signal $\mathrm{Re}(U(x, y))$, (d) imaginary part of measured signal $\mathrm{Im}(U(x, y))$, (e) amplitude of gradient of measured signal $|\partial U(x, y)/\partial x|$, (f) phase of gradient of measured signal $\partial \varphi(x, y)/\partial x$, (g) real part of gradient of measured signal $\mathrm{Re}(\partial U(x, y)/\partial x)$, and (h) imaginary part of measured signal $\mathrm{Im}(\partial U(x, y)/\partial x)$.

TABLE 1: List of samples.

Sample	Heat treatment	Temperature [°C]	Time of treatment [h]	Percentage of austenite [%]	Percentage of ferrite [%]	Percentage of sigma phase [%]
01—ref. sample	Sol.	1200	1	44.56	55.44	0
07	Sol. + aging	1200 + 800	1 + 1/2	43.38	55.92	0.7
19	Sol. + aging	1200 + 800	1 + 3/4	44.8	52.1	3.05
18	Sol. + aging	1200 + 800	1 + 3/4	44.9	51.6	3.2
02	Sol. + aging	1200 + 800	1 + 1	45.76	45.88	8.3
10	Sol. + aging	1200 + 750	1 + 2	47.28	37.64	15

dependence between the imaginary and real part of the measured signal in the case of different content of sigma phase (σ). Similar relationship was observed in [7]. Some aspects of that relationship can be explained by the fact that sigma phase (σ) is nonmagnetic, and if its amount is growing, material is getting less magnetic which results in lower coil inductance. However, the relationship between the phases and its impact on measured signal is not straightforward and has to be further investigated.

The performance of the method and the transducer was verified by utilizing DSS sample with a weld. The results of measurements obtained for selected area of the sample are presented in Figure 7. In order to emphasize the impact of changes of the material properties for measured signal, a gradient filtration in x direction was carried out. One can observe that the changes of the material properties are clearly visible.

5. Conclusions

Presented results confirm that the proposed transducer and the whole system can be successfully used for evaluation of DSS and detection of sigma phase presence. The nearly linear dependence of the output signal on the amount of sigma phase creates opportunity of an adequate quantitative evaluation. Further works on the improvement of spatial resolution are necessary. High resolution is important especially in the case of the welds testing, where HAZ has a few mm. It is also necessary to calibrate the system with bigger amount of samples in order to achieve better repeatability of the evaluation results.

Acknowledgments

References

[1] W. Zhang, D. N. Zou, G. W. Fan, and J. Li, "Influence of aging time on sigma phase precipitation in SAF2507 super-duplex stainless steel," *Materials Science Forum*, vol. 620-622, pp. 355–358, 2009.

[2] Y. Han, D. N. Zou, W. Zhang, J. H. Yu, and Y. Y. Qiao, "Influence of sigma phase precipitation on pitting corrosion of 2507 super-duplex stainless steel," *Materials Science Forum*, vol. 658, pp. 380–383, 2010.

[3] J. M. A. Rebello, M. C. A. López, R. Sacramento, and K. S. De Assis, *Quantification of Sigma Phase Precipitation by Magnetic Non Destructive Testing*, Non-destructive Testing, Corrosion and Welding Laboratory, 2010.

[4] H. Sieurin and R. Sandström, "Sigma phase precipitation in duplex stainless steel 2205," *Materials Science and Engineering A*, vol. 444, no. 1-2, pp. 271–276, 2006.

[5] S. Topolska and J. Labanowski, "Effect of microstructure on impact toughness of duplex and superduplex stainless steels," *Journal of Achievements in Materials and Manufacturing Engineering*, vol. 36, no. 2, pp. 142–149, 2009.

[6] T. Chady, J. Kowalczyk, L. Nawos-Wysocki, G. Psuj, and I. Spychalski, "PLL based eddy current measuring system for inspection of outer flaws in titanium alloy plate," in *Electromagnetic Nondestructive Evaluation (XIV)*, T. Chady, S. Gratkowski, T. Takagi, and S. S. Udpa, Eds., vol. 35, pp. 249–255, IOS Press, 2011.

[7] E. I. Todorov, M. G. Lozev, N. D. Ames, and L. O. Skogh, "Correlation between NDT measurements and sigma phase contents in duplex stainless steels," *Review of Quantitative Nondestructive Evaluation*, vol. 1096, pp. 1259–1266, 2009.

Research Article

Terahertz and Thermal Testing of Glass-Fiber Reinforced Composites with Impact Damages

T. Chady, P. Lopato, and B. Szymanik

Department of Electrical and Computer Engineering, Faculty of Electrical Engineering, West Pomeranian University of Technology, Al. Piastów 17, 70-310 Szczecin, Poland

Correspondence should be addressed to T. Chady, tchady@zut.edu.pl

The studies on glass-fiber reinforced composites, due to their growing popularity and high diversity of industrial applications, are becoming an increasingly popular branch of the nondestructive testing. Mentioned composites are used, among other applications, in wind turbine blades and are exposed to various kinds of damages. The equipment reliability requirements force the development of accurate methods of their health monitoring. In this paper we present the study of composite samples with impact damages, using three methods: terahertz time domain inspection, active thermography with convective excitation, and active thermography with microwave excitation. The results of discrete Fourier transform of obtained time sequences of signals will be presented as well as some image processing of resulting amplitude and phase images. Proposed experimental methods combined with harmonic analysis are efficient tool of defects detection and allowed to detect flaws in examined specimens. Reader may find it interesting that in spite of differences in nature of applied experimental methods, one technique of signal processing (harmonic analysis) gave adequate and comparable results in each case.

1. Introduction

Polymer composite materials, because of their high strength to weight ratio and corrosion resistance, are more and more intensively used in various industries. One of the most important applications are hulls of ships and aircrafts, piping systems of liquid fuels, and wind turbine blades. All the mentioned structures are exposed to various environmental conditions, also mechanical impacts. The impact damages result in delaminations and significant weakening of the composite structure strength thus their detection is important issue. For this reason, impact damages should be evaluated using an appropriate technique. The ultrasonic testing, radiography, and shearography are common methods of composite materials nondestructive evaluation [1]. Because of nonconducting and nonmagnetic character of most polymer composites, a terahertz technique [2] can be applied in order to detect impact defects. Authors of [3] use time gating and peak value estimation to detect impact-induced delaminations. In case of our specimens,

the response of defect is too weak to utilize this method. However, a harmonic analysis proved to be more sensitive and allowed to detect minute delaminations. Also in [3], frequency-gated harmonic analysis was successfully applied to evaluation of Kevlar/Nomex honeycomb sandwich panel. In [4], similar processing scheme with the same results is utilized for transmission measurements. In this paper, some basic information about THz time domain inspection system will be presented. Then, the harmonic analysis of THz signal will be done using the results of glass-fiber-reinforced composites reflection arrangement inspection.

In the second part of this paper, the basics of active thermography with convection heating excitation and with microwave excitation will be presented. The pulse-phase thermography with discrete Fourier transform of thermogram sequences [5] will be applied to examine the glass-fiber-reinforced composite specimens. Some image processing of obtained amplitude images and phaseograms will be shown as well.
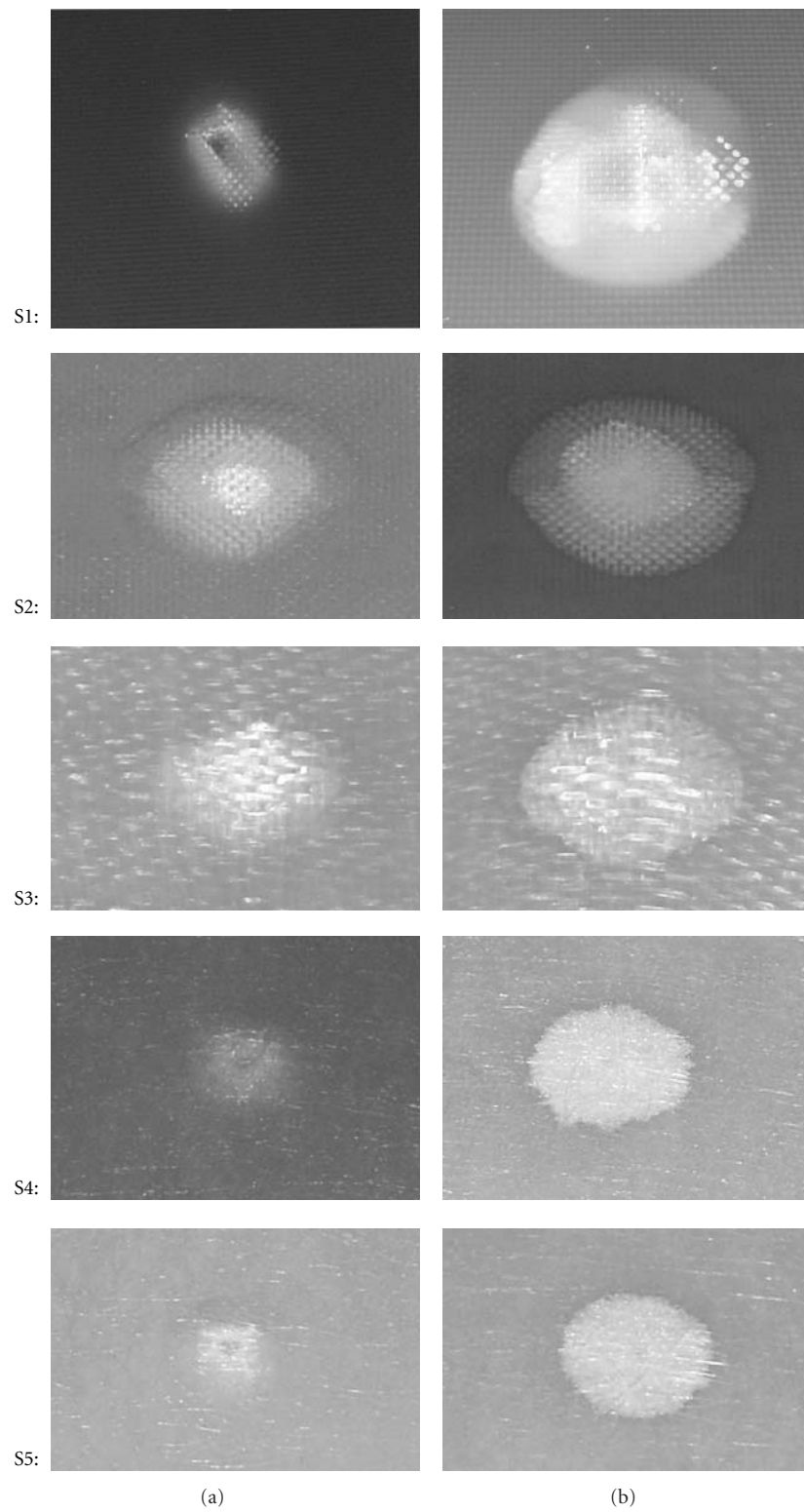
FIGURE 1: Photos of utilized impact damages in various glass-fibre-reinforced composite materials. Left: impact source side, right: opposite side.
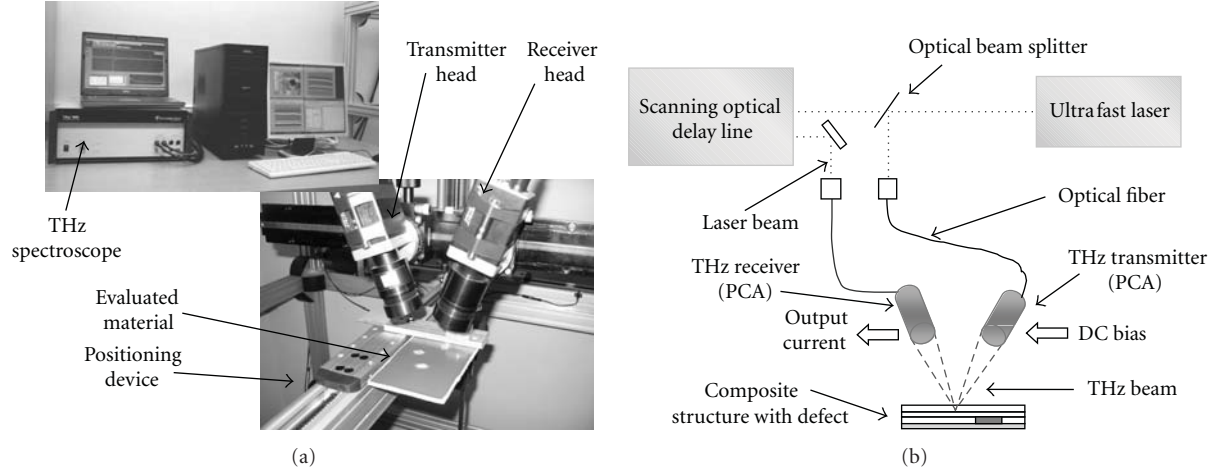
FIGURE 2: Photo (a) and simplified scheme (b) of pulsed terahertz measuring system.
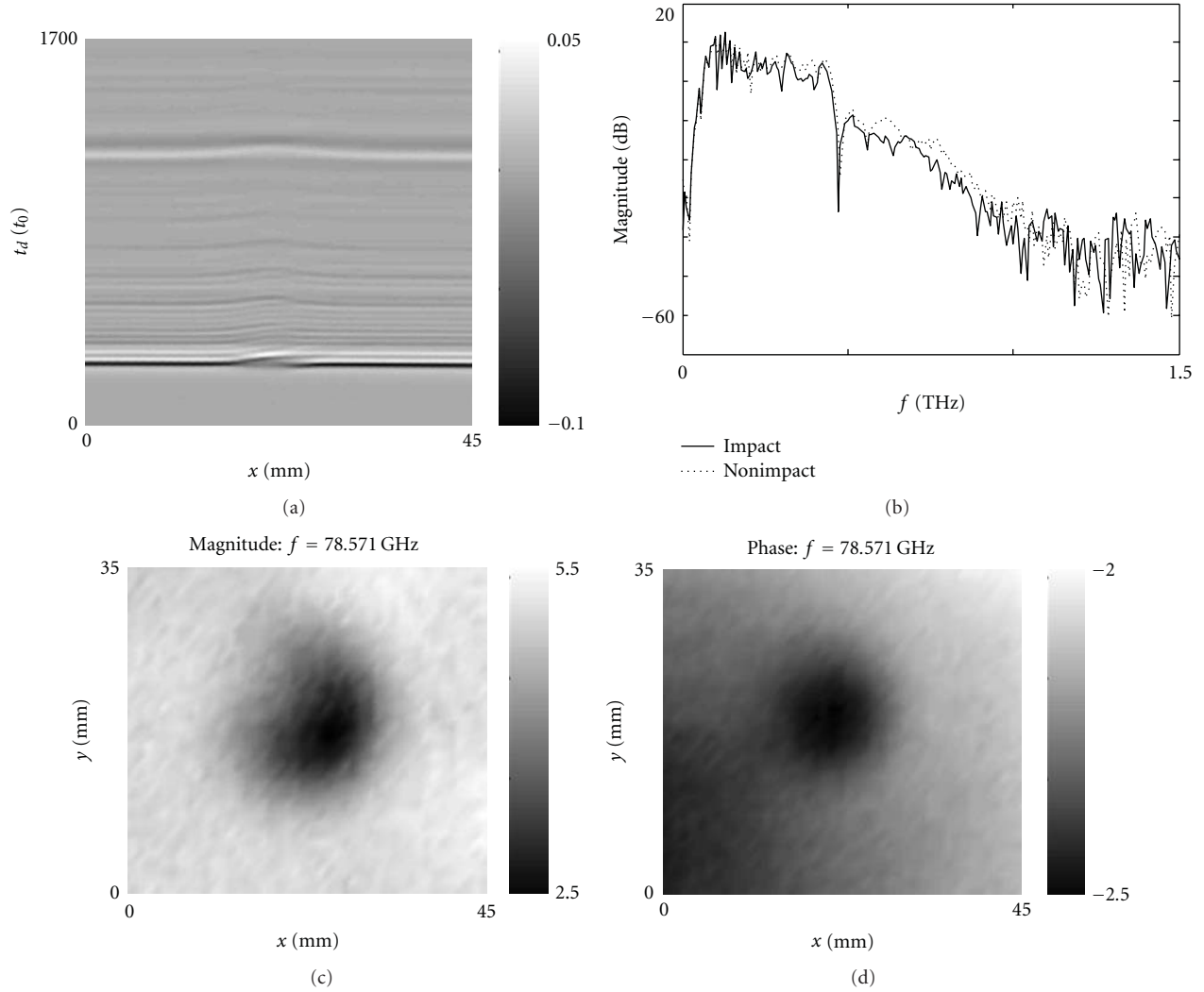
FIGURE 3: Results of S1 sample THz inspection: (a) raw B-scan signal, (b) frequency response of damaged and healthy material, (c) spatial distribution of measured waveform's magnitude in case of selected frequency, (d) distribution of phase.

(a)

(b)

Magnitude: $f = 78.571$ GHz

(c)

Phase: $f = 78.571$ GHz

(d)
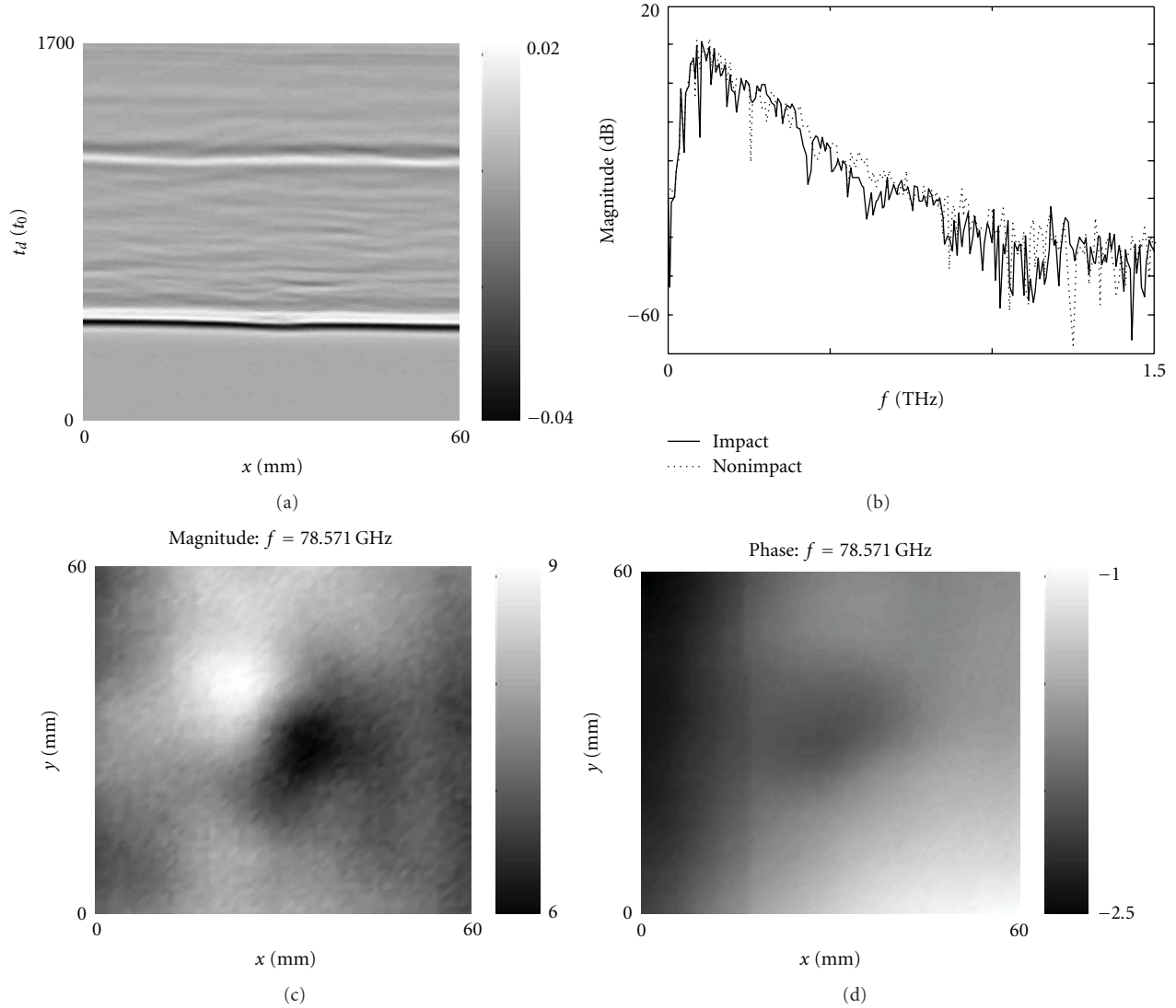
FIGURE 4: Results of S2 sample THz inspection: (a) raw B-scan signal, (b) frequency response of damaged and healthy material, (c) spatial distribution of measured waveform's magnitude in case of selected frequency, (d) distribution of phase.

2. Examined Composite Materials

Samples utilized in our experiments are presented in Figure 1. There are five types of glass-fiber-reinforced materials. Sample S1 is a commercially available material which consists of 26 plies of glass fiber fabric with regular oriented fibers. The rest of samples are dedicated materials designed and manufactured mainly for presented tests. In case of all samples, a polyester resin Polimal 109-32 K was utilized. Sample S2 consists of 26 plies of glass roving fabric with density of 170 g/m^2 and orientation setup $[0°/90°]_{13}$. Sample S3 consists of 10 plies of glass roving fabric with density of 430 g/m^2 and orientation setup $[0°/90°]_5$. Sample S4 consists of 6 plies of glass mat Vetrotex Unifilo 4750-138 with density of 450 g/m^2. The reinforcement of sample S5 is the same as in case of S4, but the resin was doped with synthetic rubber Hypro VTBNX 1300x33. All the composites were made by a hand layup method. After polymer matrix curing, the

polymer plates were cut out. The sample's thickness in each case was equal to 5 mm. The impact of 16 Joules energy was made with spherical-shaped impactor of 2 g mass.

3. Terahertz Time Domain Inspection

Pulsed terahertz NDT system based on the Tray-4000 spectroscope of Picometrix and its simplified scheme is presented in Figure 2. The main components of the system are a pair of photoconductive and fiber coupled transducers (transmitter and receiver), an ultra-fast laser, and an optical delay line.

The photoconductive antenna (PCA) based transmitter and receiver heads work in a reflection mode (as shown in Figure 2). An ultra-short THz pulse generated by the transmitting PCA is focused on an evaluated materials surface, reflected and picked up by the receiving PCA. On the basis of achieved signals, it is possible to obtain information

(a)

(b)

(c)

(d)

FIGURE 5: Results of S3 sample THz inspection: (a) raw B-scan signal, (b) frequency response of damaged and healthy material, (c) spatial distribution of measured waveform's magnitude in case of selected frequency, (d) distribution of phase.

about internal structure of the evaluated object (similar as in the ultrasonic testing). It is possible to detect any defect which disturbs distribution of refractive index, for example, inclusion, delamination, void, material inhomogeneities (fiber/matrix distribution), and internal interfaces between layers (in layered structures). Main advantages associated with terahertz technique are

(i) noncontact measurement in reflection and transmission arrangement,

(ii) nonionizing nature,

(iii) inner structure and spectral information is obtainable,

(iv) fraction of millimeter resolution.

Main disadvantages of terahertz technique are

(i) low power of THz emitters,

(ii) low speed of examination (need of raster scanning),

(iii) restriction to nonconductive materials (because of high frequency and skin effect).

4. Terahertz Time Domain Experiment's Regime and Results

The impact damaged samples were examined using pulsed terahertz technique in reflection arrangement as it was shown in Figure 2. Exemplary inspection results (B-scan signals) are presented in Figures 3(a)–7(a) (in case of all samples S1–S5). For each measuring point (x, y), a time domain response waveform consisting of 1792 samples was acquired. Sampling time step t_0 was equal to 78.1 fs, thus the resulting range of time delay in case of all measurements was 140 ps. Because of nature of the excitation, the response consists of pulses also. Two main pulses correspond to front
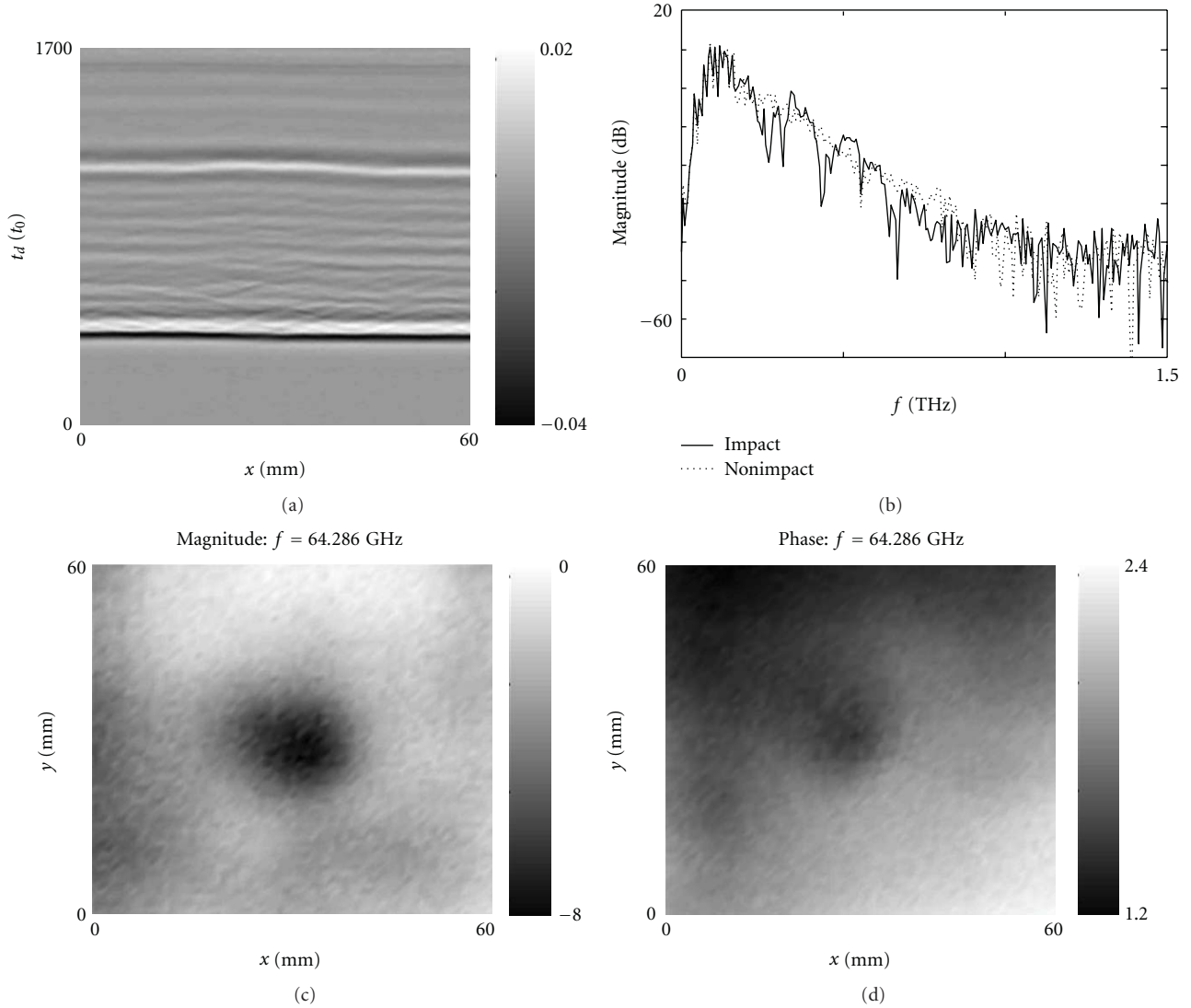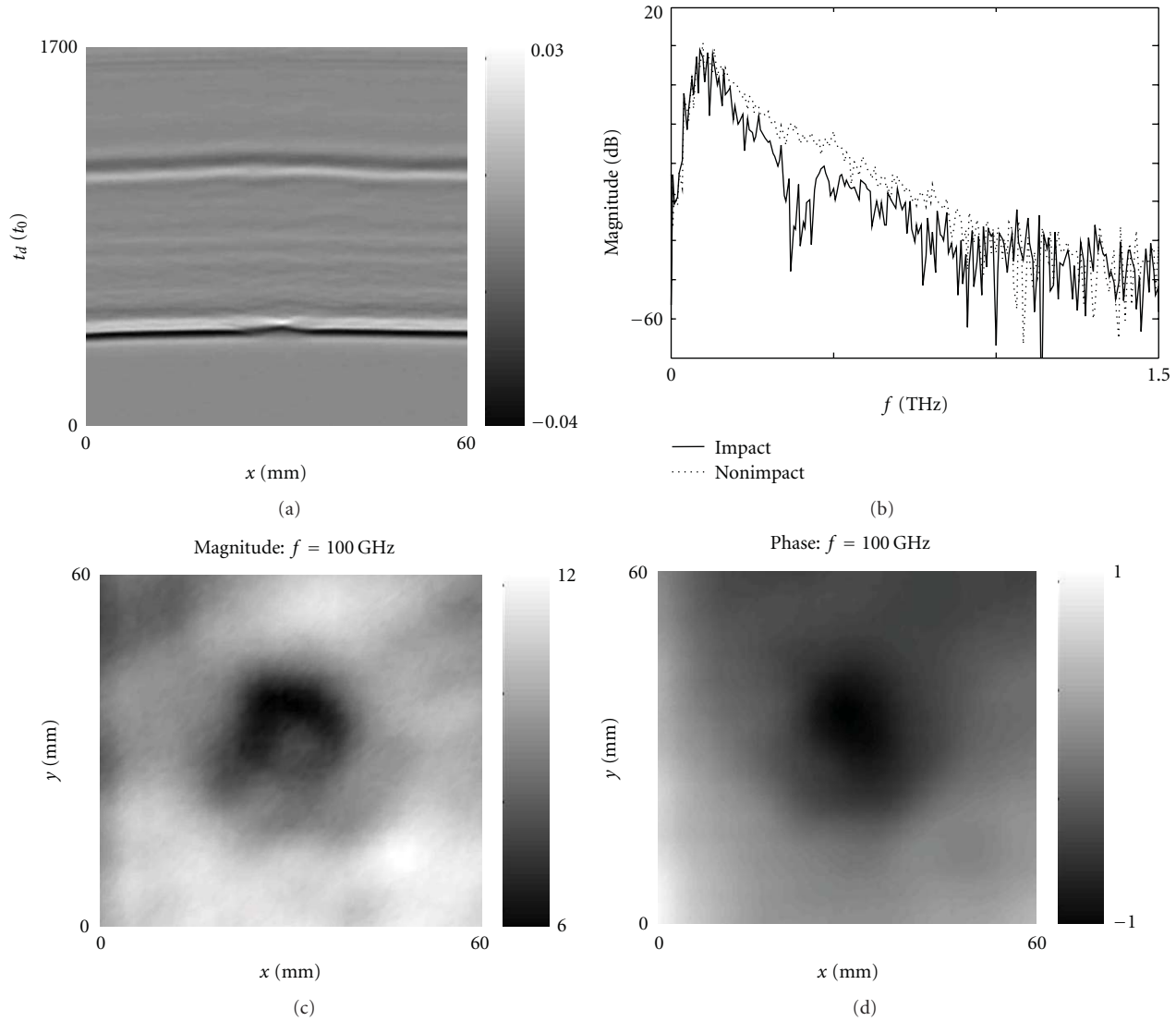
(a)

(b)

(c)

(d)

FIGURE 6: Results of S4 sample THz inspection: (a) raw B-scan signal, (b) frequency response of damaged and healthy material, (c) spatial distribution of measured waveform's magnitude in case of selected frequency, (d) distribution of phase.

(FSR) and back (BSR) surface reflections. One can observe FSR's in presented B-scans close to $t_d = 500$ and BSR's in the vicinity of $t_d = 1250$. Any additional pulse is caused by internal structure reflections. In case of layered materials (samples S1, S2, and S3), because of noticeable difference of resin and fabric refractive indices in terahertz domain, the interfaces between the layers are clearly visible directly in B-scan. The place where the surface material was exposed to mechanical forcing can be deformed upon impact. This surface deformation acts as a lens and causes local increase in amplitude of FSR. This effect is observable especially in case of samples S4 and S5. An influence of impact is clearly visible when inner structure (layers) are distinguishable. In B-scan of S1 and S3 samples, change of position of the inner layers and BSR can be seen directly. In case of other materials such visual analysis of measured signals is not sufficient.

We propose harmonic analysis of terahertz signals in order to obtain an information about impact damage position. Before this, all measured signals were median filtered in time domain and processed by Fourier transform. Frequency responses of damaged and healthy materials are presented and compared in Figures 3(b)–7(b) (in case of all samples S1–S5). The biggest differences between damaged and healthy areas are in 0.3–0.9 THz range. They are mainly associated with close-to-front surface changes in material and can be utilized in order to localize surface damage. Lower frequencies enable estimation of position and shape of impact caused defect in vicinity of back surface of the evaluated material. Spatial distributions of measured waveform's magnitude and phase in case of lower frequencies are shown in Figures 3(c)–7(c) and Figures 3(d)–7(d). In all

(a)

(b)

Magnitude: $f = 64.286$ GHz

Phase: $f = 64.286$ GHz

(c)

(d)
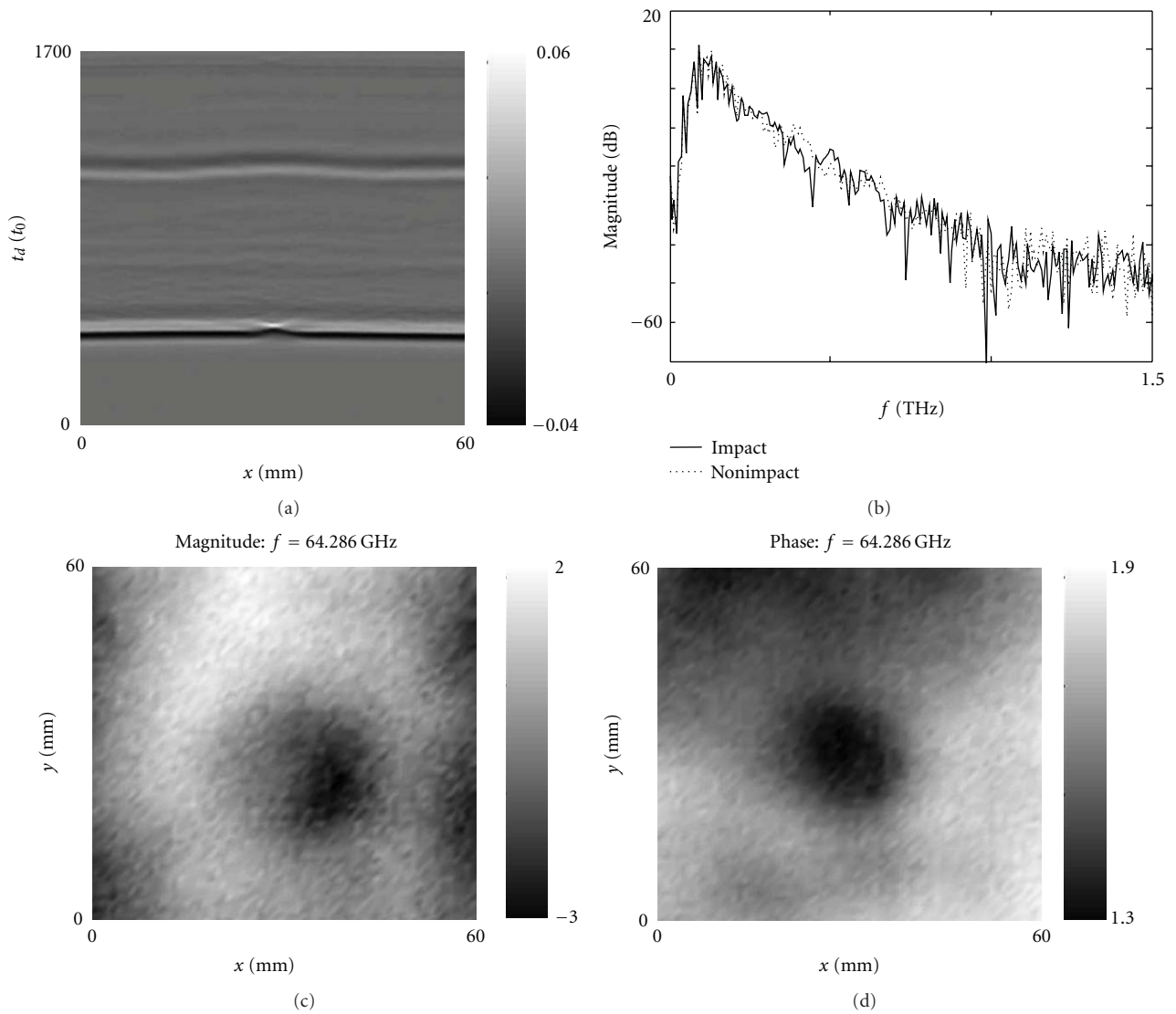
FIGURE 7: Results of S5 sample THz inspection: (a) raw B-scan signal, (b) frequency response of damaged and healthy material, (c) spatial distribution of measured waveform's magnitude in case of selected frequency, (d) distribution of phase.

(a)

(b)
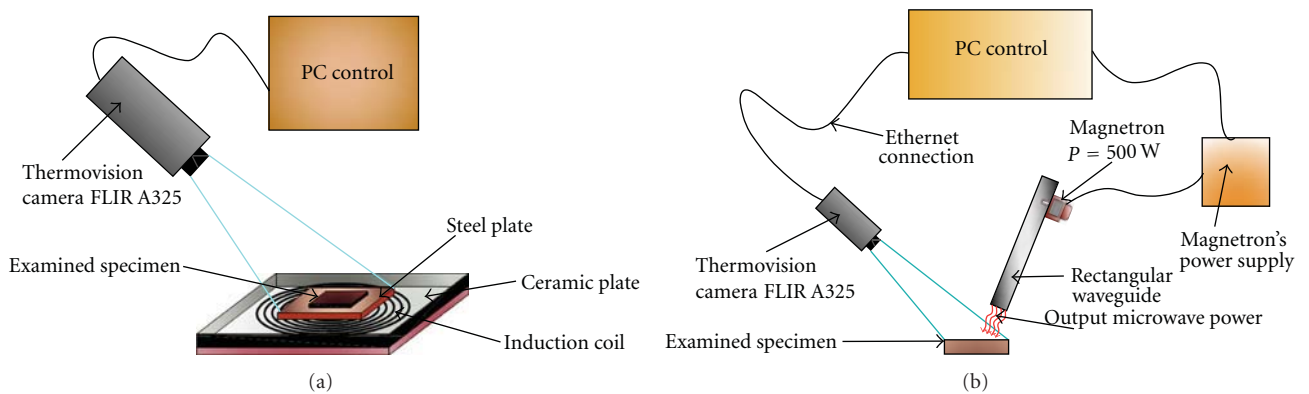
FIGURE 8: The method's scheme. (a) active thermography with convective excitation, (b) active thermography with microwave excitation.
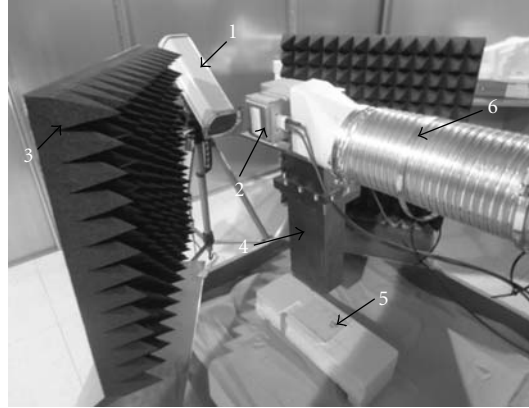
FIGURE 9: Experimental setup for active thermography with microwave excitation. (1) thermovision camera in protective housing, (2) magnetron, (3) absorbers, (4) rectangular waveguide, (5) examined sample, (6) magnetron's cooling system.

Thermogram sequence   Amplitude sequence   Phase sequence
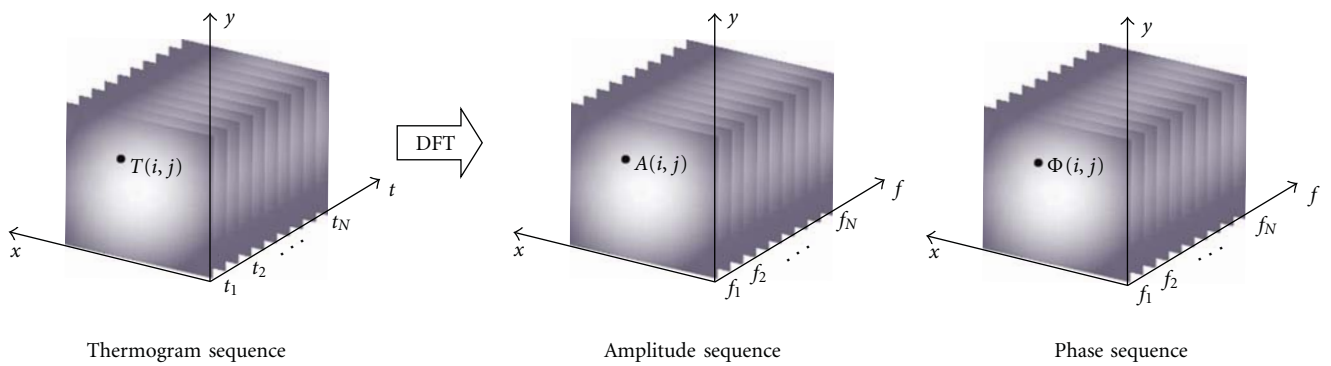
FIGURE 10: The discrete Fourier transform for thermogram sequence scheme.

(a)   (b)

(c)   (d)
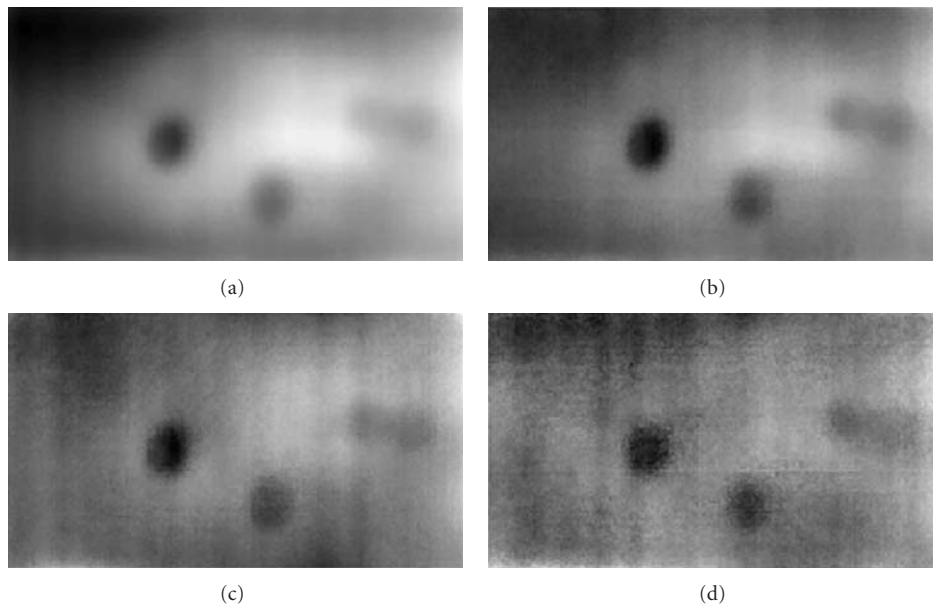
FIGURE 11: Obtained phaseograms for sample S1 (a) 0.018 Hz, (b) 0.036 Hz, (c) 0.054 Hz, (d) 0.072 Hz.

(a)

(b)

FIGURE 12: Image processing of chosen amplitude images and phaseograms for sample S1. (a) Amplitude image enhanced with median and standard deviation filtering, (b) phase enhanced with median filtering.

(a)

(b)

(c)

(d)
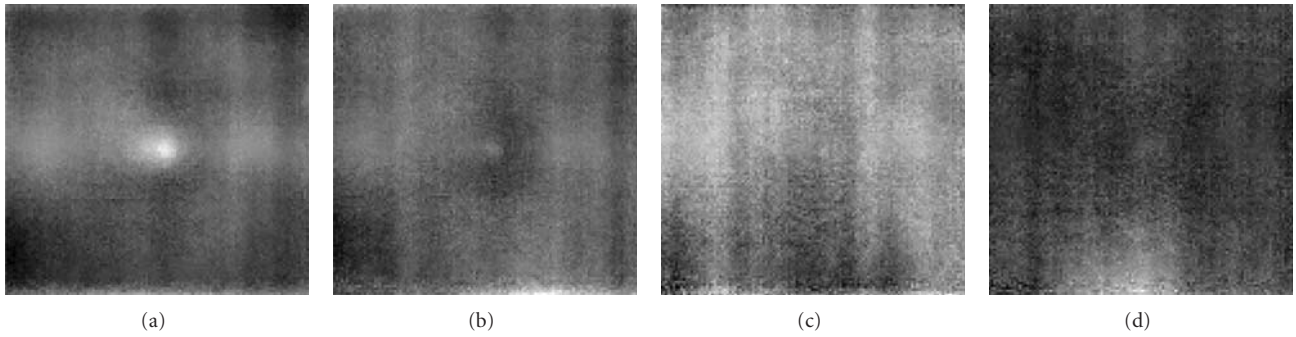
FIGURE 13: Obtained phaseograms for sample S2. (a) 0.018 Hz, (b) 0.036 Hz, (c) 0.054 Hz, (d) 0.072 Hz.

(a)

(b)
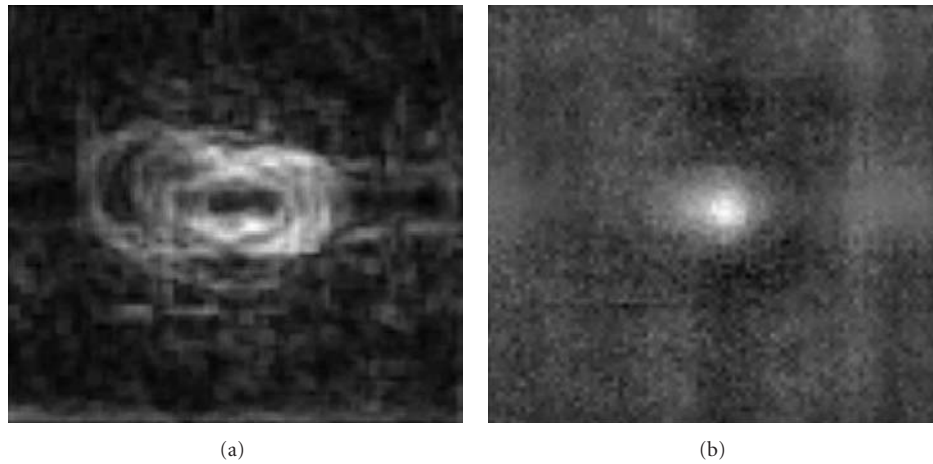
FIGURE 14: Image processing of chosen amplitude images and phaseograms for sample S2. (a) Amplitude image enhanced with median and standard deviation filtering, (b) phase enhanced with median filtering.

(a)

(b)

(c)

(d)
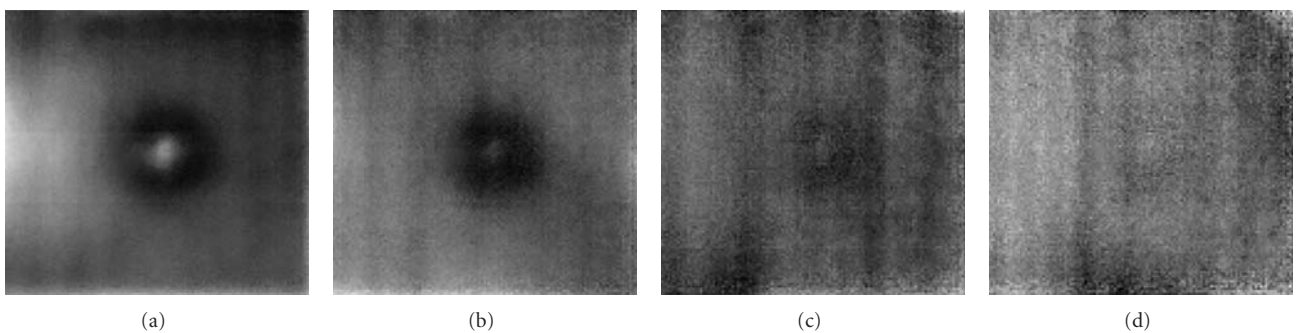
FIGURE 15: Obtained phaseograms for sample S3. (a) 0.018 Hz, (b) 0.036 Hz, (c) 0.054 Hz, (d) 0.072 Hz.

<div style="text-align:center">(a)　　　　　　　　　　　　　　　　　　(b)</div>
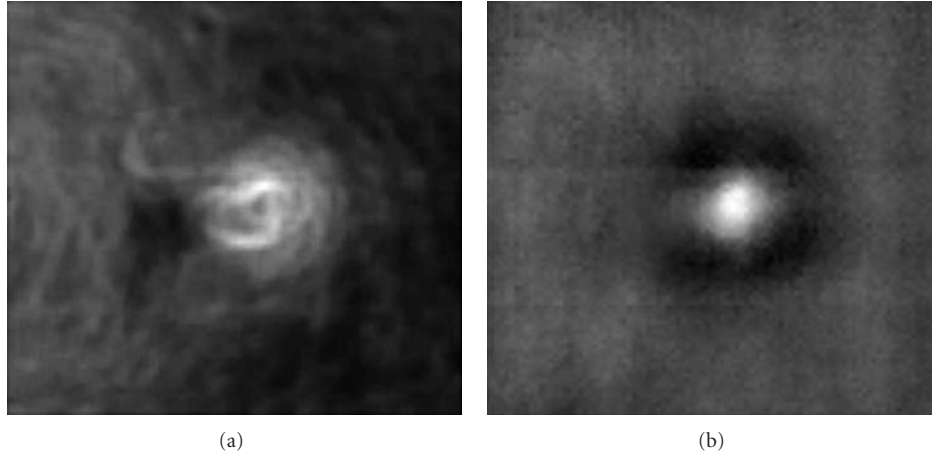
FIGURE 16: Image processing of chosen amplitude images and phaseograms for sample S3. (a) Amplitude image enhanced with median and standard deviation filtering, (b) phase enhanced with median filtering.

<div style="text-align:center">(a)　　　　　　　　　(b)　　　　　　　　　(c)　　　　　　　　　(d)</div>
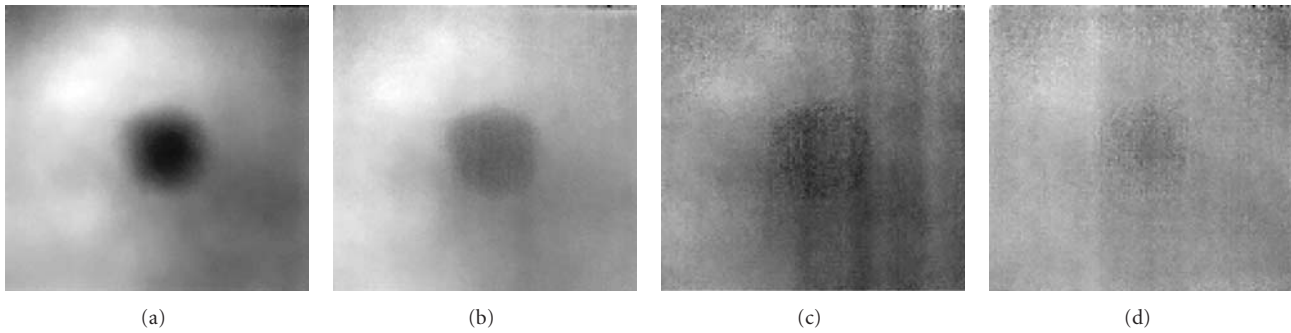
FIGURE 17: Obtained phaseograms for sample S4. (a) 0.018 Hz, (b) 0.036 Hz, (c) 0.054 Hz, (d) 0.072 Hz.

cases, localization of defect based on obtained distributions is possible.

In case of frequencies higher than 0.9 THz, because of very low SNR, signal contains no applicable information about defect (Figures 4, 5, and 6).

## 5. Active Thermography with Convection and Microwave Excitation

Composite samples with impact damages were investigated using active infrared thermography. As the excitation, we propose two energy sources: convective heat flow from inductively heated steel plate (contact method) and microwave heating (contactless method). In the convective heating, the composite sample is placed on the inductively heated steel plate (Figure 8(a)). The free flow of heat through the examined specimen can be then observed using thermovision camera. Defects are detected as (depending on the damage type) under- or overheated spots. The main disadvantage of this method is the requirement that the sample should be in contact with the heated steel plate, which can make problems for practical applications.

The active thermography with microwave excitation is the contactless method. In this technique, examined sample is heated by high power microwaves (500 W, working at the frequency 2.45 GHz). Heating phase is observed by the properly secured thermovision camera. A schematic drawing of the method is shown in Figure 8(b) whereas Figure 9 shows the designed laboratory setup.

Since in both techniques the heating phase can be observed, the pulsed phase thermography (PPT) could be applied. This method combines the experimental procedure used in pulsed thermography (PT), with signal analysis used in modulated thermography (MT) [6]. The thermograms' sequence is recorded, while the heat pulse is applied to examined specimen.

The analysis of obtained sequence is based on discrete Fourier transform (DFT), which allows to evaluate the output as the combination of phase and amplitude. The procedure scheme is presented in Figure 10.

The well-known Fourier Transform of each pixel in the thermogram sequence may be written as follows [7]:

$$F_n = \sum_{k=0}^{N-1} T(k)e^{-j2\pi ink/N} = \mathrm{Re}_n + \mathrm{Im}_n, \tag{1}$$

where n denotes the frequency increment, and Re and Im indicate the real and imaginary parts of transform. The

(a)   (b)
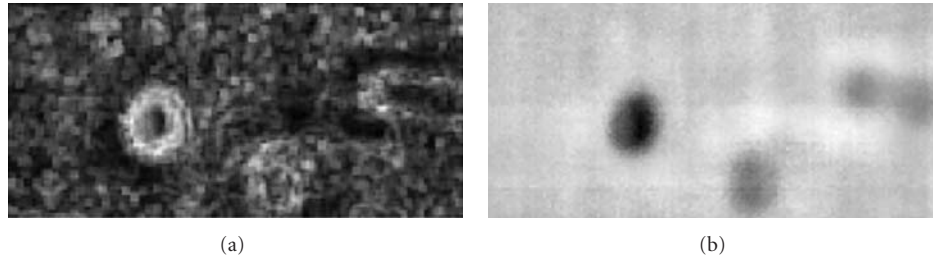
Figure 18: Image processing of chosen amplitude images and phaseograms for sample S4. (a) Amplitude image enhanced with median and standard deviation filtering, (b) phase enhanced with median filtering.
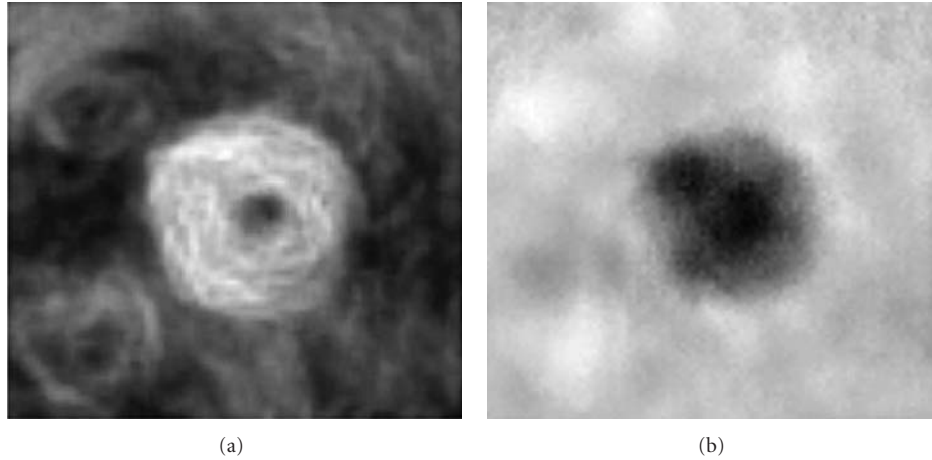

(a)   (b)   (c)   (d)
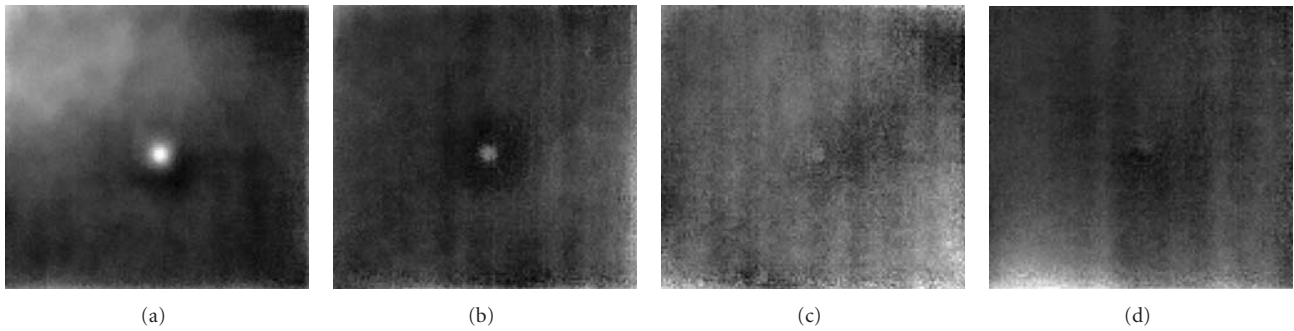
Figure 19: Obtained phaseograms for sample S5. (a) 0.018 Hz, (b) 0.036 Hz, (c) 0.054 Hz, (d) 0.072 Hz.

amplitude (A_n) and phase (ϕ_n) are computed using following formulas:

$$A_n = \sqrt{\mathrm{Re}_n^2 + \mathrm{Im}_n^2}, \qquad \Phi_n = \arctan \frac{\mathrm{Im}_n}{\mathrm{Re}_n}. \qquad (2)$$

Both amplitude images and phaseograms were used to obtain reliable results of specimens' evaluation.

5.1. Active Thermography with Convection Heating Experiment's Regime and Results.

In case of convection heating, all five samples were tested, using the same heating time and recording frequency. The observation time was set to 55 second, and recording frequency was 9 Hz, which allowed us to obtain 495 thermograms in one sequence. For every sample, the same procedure of signal processing was used: the DFT of thermograms sequence was performed, chosen amplitude images and phaseograms were then processed using median or standard deviation filter, to enhance the contrast between the background and defect.

The results (chosen phaseograms, and image processing of selected amplitude images and phaseograms) are shown in Figures 11–20.

It can be notice that best results for phase images of samples S2–S5 (Figures 13(a), 15(a), 17(a), and 19(a)) are obtained for frequency of 0.018 Hz, which was simultaneously the lowest available frequency in these experiments. In case of sample S1, the phaseogram for frequency of 0.036 Hz presents all the defects in most distinguishable way (Figure 11(b)). The median (for heating unevenness removal) and standard deviation (for defect enhancement) filtering of signal amplitude image gives in each case the information of defect location and size.

5.2. Active Thermography with Microwave Heating Experiment's Regime and Results.

Microwave-enhanced infrared thermography is a relatively new NDT method. Using microwaves as the energy source gives a possibility of volumetric heating of the material, which can significantly speed up the heat process. Moreover, this method is contactless. Unfortunately, the high power microwaves, needed to obtain visible temperature differences between the defect and the background, may cause damage to the thermovision camera. Therefore, additional protective housing is needed in this case. Special metallic mesh, used as camera lens protection, increases the noise level in obtained thermograms. The image processing of thermogram sequence is then more demanding and time consuming.

In case of microwave heating the observation time was set to 100 seconds, and recording frequency was set

(a)

(b)

FIGURE 20: Image processing of chosen amplitude images and phaseograms for sample S5. (a) Amplitude image enhanced with median and standard deviation filtering, (b) phase enhanced with median filtering.
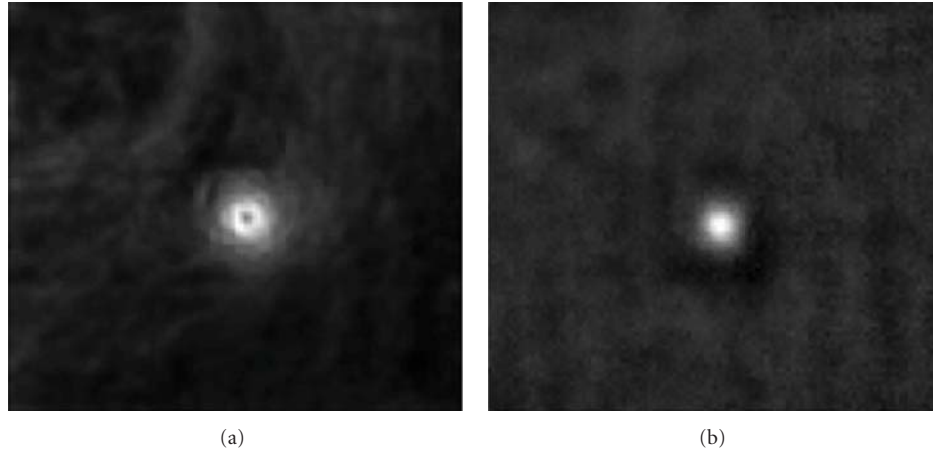

(a)

(b)

FIGURE 21: Obtained results for sample S2. (a) Chosen initial amplitude image, (b) amplitude image after several filtering procedures.

to 15 Hz, which allowed to obtain 1500 thermograms in one sequence. After the DFT procedure, chosen amplitude images were enhanced using procedure based on multiply filtering. Obtained results (only for samples S2 to S5) are promising (Figures 14–17), but obviously future work is needed to obtain more accurately outcome. Heating of sample S1 and obtained thermogram sequence analysis using DFT did not allow for damage detection, therefore, it was omitted in the presentation of the resulting images (Figures 21–24).

The image processing of available amplitude images was based on median filtering and contrast enhancement. Obtained results give the defect approximate location, but the information about flaws' size is not contained in resulting images.

Due to high noise level in the output thermograms, the research on improving the methodology of measurement should be continued. The time of heating extension in order to increase the temperature contrast between the background and defect as well as the sequence of thermograms recording frequency increment is, therefore, considered.

6. Conclusions

Both utilized methods of glass-fiber-reinforced composites examination enable detection of impact caused defects. The pulsed THz technique offers very wide and unique (compared to other common methods) abilities of inspection: high resolution, no need to use any additional coupling medium, availability of spectroscopic information, and finally a defect depth information is also provided. Simple harmonic analysis is sufficient tool in detection of damages caused by mechanical impacts in case of various kinds of materials.

Active infrared thermography is a fast (sometimes it allows real time monitoring of structures) and giving tangible results method. The convection excitation allows obtaining information about the location and size of the defect. The harmonic analysis of obtained thermograms' sequences for specimens S1–S5 (representing different types of composite material which may be found in practical usage) proved to be sufficient to obtain reliable results. In each case, the defect itself is clearly visible, moreover, additional analysis using standard devaition filtration, allowed

(a)   (b)

FIGURE 22: Obtained results for sample S3. (a) Chosen initial t amplitude image, (b) amplitude image after several filtering procedures.

(a)   (b)
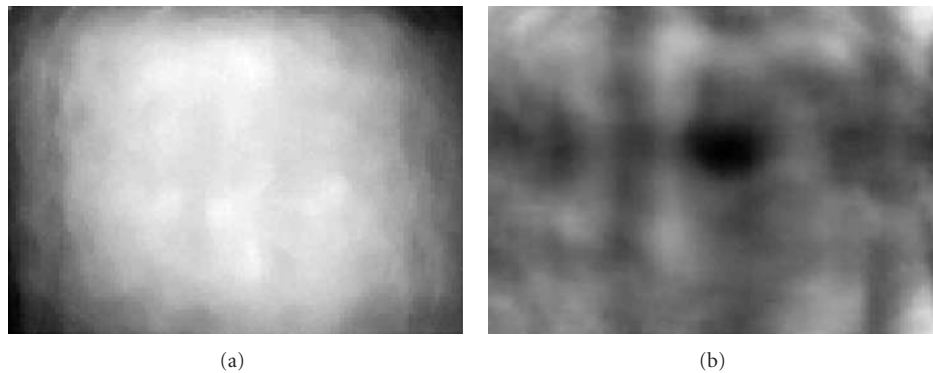
FIGURE 23: Obtained results for sample S4. (a) Chosen initial amplitude image, (b) amplitude image after several filtering procedures.

(a)   (b)
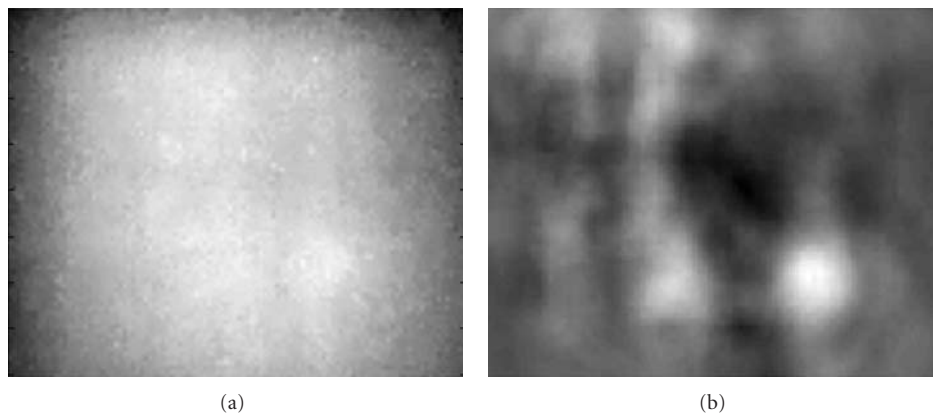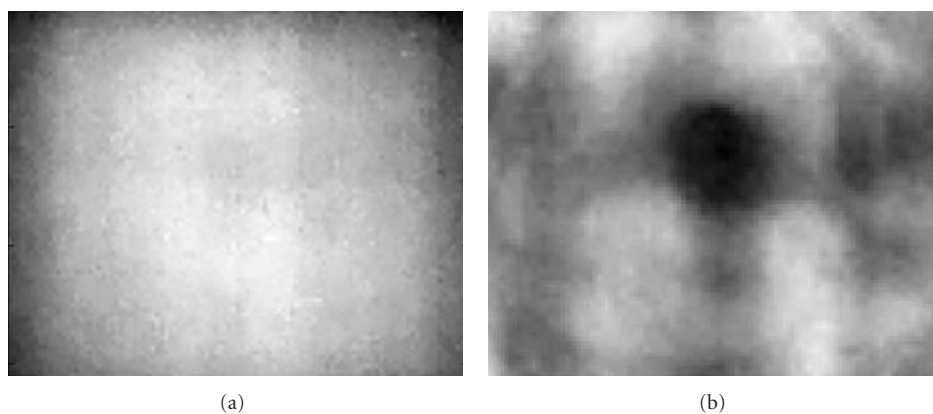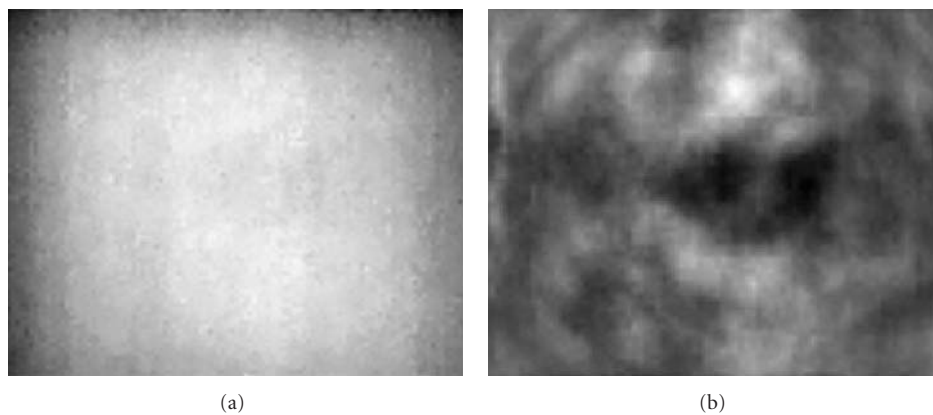
FIGURE 24: Obtained results for sample S5. (a) Chosen initial amplitude image, (b) amplitude image after several filtering procedures.

to visualize delamination arose in the vicinity of damage. The application of this method in practice, however, due to the fact that it requires contact with the heat source, can be sometimes difficult. The microwave excitation, on the other hand, is a contactless method. However, it requires additional thermovision camera protection, which causes significant increment of obtained thermograms noise level. Therefore, the received thermogram sequence image processing is much more difficult. The harmonic analysis in this case was connected with additional signal processing involving trend removal based on median filtering. Nevertheless, obtained results allow only to an approximate localization of the defect. The further development of the active infrared thermography with microwave excitation method, however, is highly warranted because of the ease of its industrial application, high speed, and the ability to simultaneous study of materials' large surfaces.

Each sample was examined using two different methods (i.e., THz imaging and active thermography with two energy sources), but the signal processing technique was chosen to be the same for data obtained with both utilized methods. Reader may notice that harmonic analysis allowed to detect the flaws in examined samples, and obtained results may be used to quantitative and qualitative evaluation of materials.

Acknowledgment

References

[1] A. Kapadia, *Non Destructive Testing of Composite Materials*, TWI Ltd.

[2] D. M. Mittleman, M. Gupta, R. Neelamani, R. G. Baraniuk, J. V. Rudd, and M. Koch, "Recent advances in terahertz imaging," *Applied Physics B*, vol. 68, no. 6, pp. 1085–1094, 1999.

[3] D. K. Hsu, K. H. Im, C. P. Chiou, and D. J. Barnard, "An exploration of the utilities of terahertz waves for the NDE of composites," in *Proceedings of the Review of Quantitative Nondestructive Evaluation*, vol. 30 of *AIP Conference Proceedings*, pp. 533–540, New York, NY, USA, 2011.

[4] F. Rutz, M. Koch, S. Khare, M. Moneke, H. Richter, and U. Ewert, "Terahertz quality control of polymeric products," *International Journal of Infrared and Millimeter Waves*, vol. 27, no. 4, pp. 547–556, 2006.

[5] X. Maldague and S. Marinetti, "Pulse phase infrared thermography," *Journal of Applied Physics*, vol. 79, no. 5, pp. 2694–2698, 1996.

[6] X. Maladegue, *Theory and Practice of Infrared Technology for Nondestructive Testing*, John Wiley and Sons, New York, NY, USA, 2001.

[7] S. Marinetti, Y. A. Plotnikov, W. P. Winfree, and A. Braggiotti, "Pulse phase thermography for defect detection and visualization," in *Nondestructive Evaluation of Aging Aircraft, Airports, and Aerospace Hardware III*, vol. 3586 of *Proceedings of SPIE*, pp. 230–238.

Research Article

Comparison of Nondestructive Testing Methods on Detection of Delaminations in Composites

Liang Cheng[1] and Gui Yun Tian[1, 2]

[1] *School of Electrical, Electronic and Computer Engineering, Newcastle University, Newcastle upon Tyne, NE1 7RU, UK*
[2] *School of Automation, Nanjing University of Aeronautics and Astronautics, Nanjing 210016, China*

Correspondence should be addressed to Liang Cheng, liang.cheng@ncl.ac.uk

Received 3 November 2011; Accepted 31 January 2012

Academic Editor: B. P. C. Rao

Delamination is one of the most common defects in carbon fibre reinforced plastic (CFRP) components, such as those used in aircraft and wind turbine blades. To detect delaminations, different NDT methods such as ultrasonic (UT), eddy current (EC) scanning, flash thermography, and recent developed pulsed-eddy-current-(PEC-) simulated thermography are conducted for comparison and evaluation of the new developed PEC thermography system at Nanjing University of Aeronautics and Astronautics (NUAA), China through UK-China collaboration. A PEC-stimulated thermography system is built at NUAA, extended from previous joint work between Newcastle and Bath Universities. Using these NDT systems, man-made, dedicated delaminations with varied diameters and depths are investigated and studied. Through this comparison, PEC-stumilated and flash thermography show relatively good indications of the shape of delaminations. The joint studies also show that PEC-stimulated thermography has unique advantage for fibre orientation evaluation.

1. Introduction

A composite material can be defined as a combination of two and more materials with very different mechanical, thermal, and electrical properties. Due to the low weight and high strength of composites, they are popular for use in aircraft and wind turbine blades. Delamination is one of the most common defects for composite materials. It leads to the degradation of mechanical properties and also causes the failure of the overall composite component. To detect delaminations and ensure the safe operation of composite components, nondestructive evaluation (NDE) techniques are used during both manufacturing and operation of the materials. For NDE of CFRP, a series of specific methods are in continuing development to increase the probability of fault detection at a high-confidence level.

The multilayered structure of CFRP allows the use of Lamb waves [1–4] with good results for the qualitative evaluation of CFRP materials. X-ray methods are also used [5], along with acoustic emission techniques [6, 7]. Because

carbon fibres are electrically conductive, for the nondestructive evaluation of CFRP, electromagnetic methods such as those based on eddy currents [8, 9] and microwaves [10] can be used.

An extremely promising technique is thermography, which has the advantage of good fault detection possibility along with the capacity to inspect a large area within a short time. Thermography is also applicable to a wide range of materials, including glass fibre, carbon fibre composites, and metallic materials, where specific excitation techniques are needed for each application. To inspect defects over a large scale and at large stand-off distances, integration of thermography and other NDE approaches have been investigated [11–15], for example, flash thermography [16–18], vibrothermography, sonic thermography, laser thermography, and pulsed-eddy-current-(PEC-) stimulated thermography.

In the case of CFRP, PEC-stimulated thermography can be applied with good results [19]. Carbon fibres present good electrical and thermal conductivity along the fibre to reach the required mechanical parameters; designers use

either several carbon fibres layers or separate carbon fibres woven together. In general, the fibres from a layer are preimpregnated with polymer resins, forming a lamina that can have uniaxial electrical and thermal anisotropy or biaxial in the case of woven satin carbon fibre. Moreover, CFRP composites will have higher electrical conductivity along the direction of carbon fibres and lower conductivity perpendicular to the fibres in the lamina plane and cross-layer.

PEC-stimulated thermography, combining PEC and thermography, involves the application of a high current electromagnetic pulse to the conductive material under inspection for a short period. In this paper, eddy currents will be induced in the material, leading to the heating of the material itself. The existence of any defects distorts the propagation of the eddy current leading to a variation in material temperature that can be emphasised with thermography. After the period of eddy current heating, the nonhomogeneities of CFRP in the cooling phase also affect the diffusion of heat. Therefore, the mixed phenomena of induction heating dominating in the heating phase and the diffusion of this dominating in the cooling phase and their specific behaviours are useful for the quantitative nondestructive evaluation of a given material's non-homogeneities. Based on recent development at Newcastle and Bath in collaboration with Rolls Royce and Alstom [19], a new low cost and portable PEC-stimulated thermography system is built at NUAA to evaluate the composites and metallic object used in wind or aerospace industry, particularly delamination in composite in this paper. PEC-stimulated thermography has been used to inspect metallic parts in previous studies [20–22]. The temperature distribution around a crack with different penetration depths using FEM modelling has been investigated in [21] and compared with experimental measurements on metallic materials. The results showed that lower temperatures are exhibited at the surface edge of a crack and higher temperatures at the bottom in nonmagnetic materials with a large penetration depth. From previous work in [23], PEC-stimulated thermography was proposed and extended from the surface detection of cracks in metallic parts to the detection of surface discontinuities in CFRP composites, via numerical simulation and experiments. However, other types of defects in composite materials were rarely investigated. Ramdane et al. [24] detected inserted delaminations using induction heating thermography. The experimental studies were undertaken in transmission mode (the inductor and infrared camera are on the different sides of the sample), which is normally not applicable in the in situ inspection. Moreover, the inspection period is around 80 seconds.

In this paper, delaminations within CFRP composites are investigated using PEC-stimulated thermography in reflection mode (the inductor and infrared camera are on the same side of the sample) aiming to reduce the inspection period significantly. In addition, the PEC-stimulated thermography results are compared with other widely used methods such as ultrasonic and flash thermography. The rest of the paper is organised as follows. Section 2 introduces the samples
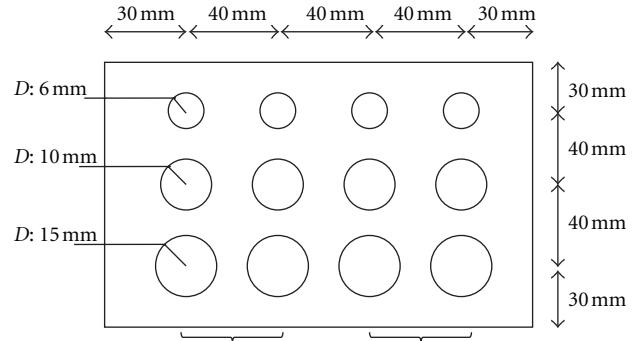
FIGURE 1: Sample layouts with man-made delaminations.

under test; in Section 3, the four experimental systems—PEC stimulated thermography, flash thermography, UT/EC scanning system are illustrated; in Section 4, experimental results using individual systems are reported and compared. Section 5 summarises the work and looks forward towards future work.

2. Samples Preparation

20-layered CFRP samples (CYCOM970/T300) are used. The dimensions of the samples are $180 \times 140 \times 3.1 \text{ mm}^3$. The man-made delaminations are manufactured by inserting a two-layered polytetrafluoroethylene film (of thickness 0.1 mm for each layer) between two fibre layers. The diameters D of the delaminations are 6 mm, 10 mm, and 15 mm, respectively and the delaminations are manufactured at the interface of 1st-2nd, 2nd-3rd, 5th-6th, 6th-7th, 9th-10th, and 10th-11th layers, respectively.

The sample layouts with delaminations are shown in Figure 1. Delaminations with 3 different diameters and 6 different depths (155 μm, 310 μm, 775 μm, 930 μm, 1395 μm, and 1550 μm, resp.) are manufactured in three samples. Samples 1–3 are manufactured by Beijing Institute of Aeronautical Material.

3. Experiment Systems

To investigate the CFRP samples with man-made delaminations, four experimental systems are used at NUAA, which are PEC-stimulated thermography, flash thermography, and UT and EC scanning systems.

3.1. PEC-Stimulated Thermography System. Figure 2(a) shows the PEC-stimulated thermography system setup. HB-X5K high frequency heater with a work head linked to a coil from Wuxi Gaopin Technology Co., Ltd is used for pulsed eddy current excitation at NUAA. The heater provides a maximal 2 kW output at 320 kHz. The diameter of copper hollow is 2.08 mm and the outer diameter of circular coil
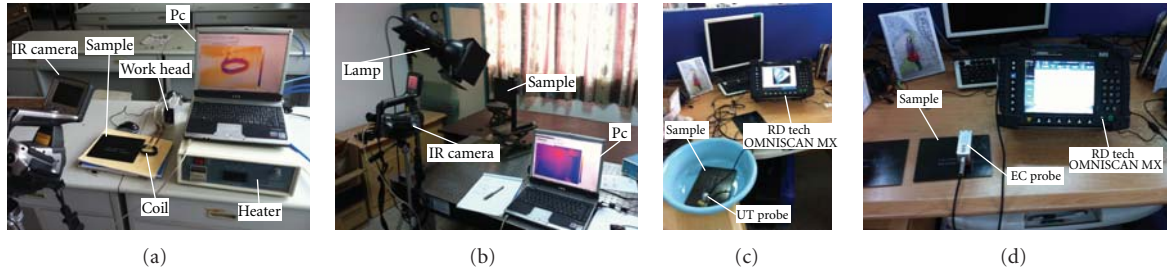
(a)   (b)   (c)   (d)

Figure 2: Experimental systems at NUAA: (a) PEC-stimulated thermography; (b) flash thermography; (c) UT scan; (d) EC scan.

(a)   (b)   (c)   (d)
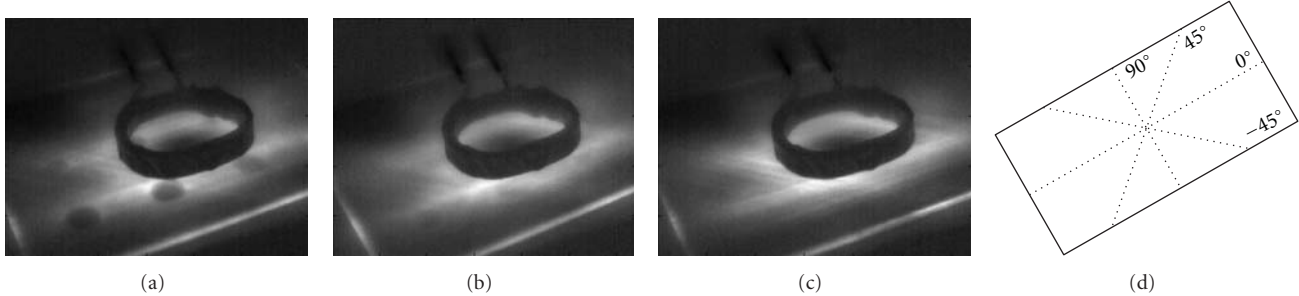
Figure 3: Thermal images at maximum heating (1 s): (a) sample 1; (b) sample 2; (c) sample 3; (d) fibre orientation definition.

is approximately 50 mm. A Flir ThermaCAM S65 is used to record thermal images and videos. The IR camera has a maximum full frame rate of 50 Hz, providing 1 frame every 20 ms. In contrast to the system built at Newcastle-Bath universities, the low-end IR camera with lower frame rates of 50 Hz comparing to 383 Hz in previous work, a battery and thermal video memory card is used at NUAA. Hopefully, this system can be suitable for offshore inspection. Therefore, without a water-cooling system for the coil, the recording period for one inspection is investigated to avoid the overheating on coil to affect the results.

3.2. Flash Thermography System.
A flash lamp with 1 kW output power is used as heat source. A switch control unit is applied to control the heating duration from the lamp, as shown in Figure 2(b). The Flir ThermaCAM S65 is used to record thermal images and videos.

3.3. Ultrasonic and Eddy Current Scanning System.
Ultrasonic and eddy current scanning using RD tech OMNISCAN MX on the samples are conducted at NUAA. It can be used in phased array acquisition module for UT scanning and eddy cureent array acquisition module for EC scanning. The ultrasonic probe, RD tech SA1-N45S (4 by 4 sensor array in the area of 30 mm × 30 mm), works at 5 MHz. The probe's refracted angle is 45° for angle beam inspection from 30° to 70° using shear wave. The sound velocity in the sample is approximately 3100 m/s; EC array probe, RD tech SAA-056-005-016 is used for EC scanning. The EC probe consists of 8-by-2-coil array, working from 1 kHz to 25 kHz with 3.5 mm spatial resolution. The UT and EC scan system are shown in Figures 2(c) and 2(d), respectively.

4. Experimental Results

4.1. PEC-Stimulated Thermography Results.
One-second heating period followed by two-second cooling is applied when the maximum power output of 2 kW. The 15 mm diameter delaminations in samples 1, 2, and 3 are investigated. Delaminations at 155 μm and 310 μm deep can be seen as dark circles in Figure 3(a). In Figure 3(b), the delaminations at 775 μm and 930 μm deep are observed on the lower left and right to the coil, respectively. Delaminations at 1395 μm and 1550 μm deep in sample 3 are not observed in raw thermal images/videos.

Delaminations lead little distortion on eddy current distribution since eddy currents parallel to the layers have little interaction with the delaminations, which is not sensitive enough for EC scanning system reported in Section 4.4. The heat is generated mainly in 0° and −45° (the direction is defined as shown in Figure 3(d) by the eddy currents induced by the inductor and they propagate in these two directions). Since the electric and thermal conductivities are largest along the fibre orientation, it can be known that the fibre orientations in 1st and 2nd layers are −45° and 0°. The delamination, as a thermal barrier, hinders heat propagation mainly in 0° and −45° directions, which results in a hot spot on the delamination edge and a cool spot on the delamination region. Comparing the results from eddy current scanning discussed in Section 4.4, it can be seen that the heat diffusion is the main cause of heat generation at delaminations using PEC-stimulated thermography, allowing us to detect fibre breakage through these thermal images in advance. In addition, heat diffusion along fibres in each layer is evaluated using PEC-stimulated thermography.
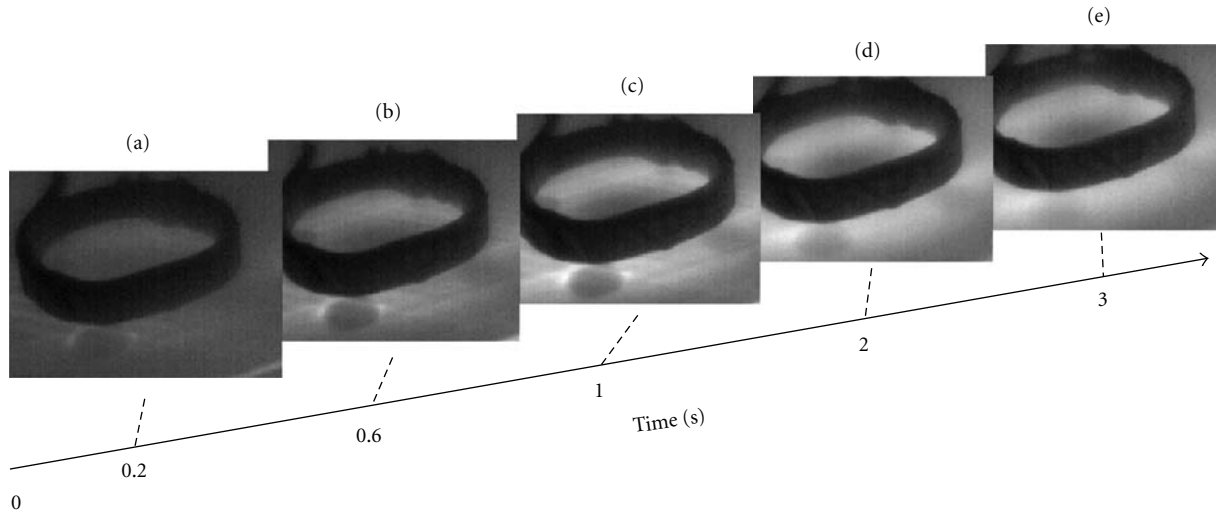
FIGURE 4: Thermal images for sample 1 at (a) 0.2 s; (b) 0.6 s; (c) 1 s; (d) 2 s; (e) 3 s.

In Figure 4, the thermal images at different times of heating or cooling phase are shown. At the beginning of heating (0.2 s), the edge of 155 μm deep delamination at lower left to the coil is highlighted, whilst the 310 μm deep delamination at the right bottom is not visible (Figure 4(a)). And as heating time increases, the contrast between delamination and sound area increases and the 310 μm deep delamination can be noticed (Figure 4(b)). Till the maximum heating (1 s), the contrast between delaminations and sound area becomes the biggest (Figure 4(c)). After that, the heat diffusion in cooling phase blurs the images (Figures 4(d) and 4(e)). In Figure 4, it shows the shallower delamination can be observed earlier and the temperature contrast is larger. Different layer structure and fibre orientation can be easily visualised through the video sequences, which is in contrast to the surface inspection using flash thermography results below.

4.2. Flash Thermography Results. The temperature images using flash thermography for samples 1, 2, and 3 are shown in Figures 5(a)–5(c), respectively, after a period of 5-second heating. From these results, delaminations in both samples 1 and 2 are observed but are not in sample 3. Due to the surface heating by flash thermography, heat propagates from the surface to the rear side. Delaminations, as thermal barriers, stop heat diffusion and reflect the heat back to the surface, which results in higher temperatures at delaminations than in nondefected regions. Therefore, flash thermography provides heat diffusion information in the depth direction rather than in the direction of fibre orientations in each layer using PEC-stimulated thermography.

4.3. Ultrasonic Scanning Results. The reflected ultrasonic signals and C-scan images on each delamination with 15 mm diameter and varied depths are shown in Figure 6. The probe's refracted angle is 45° for angle beam inspection from 30° to 70° using shear wave. In Figure 6(a), we can observe

many reflections in the nondefected region, which is caused by the multilayer structure of CFRP. The delaminations are identified by high reflection amplitude of ultrasound signals and shown as red regions in the images of interfaces of delamination and CFRP materials, as shown in Figures 6(b)–6(g). Due to the thin-layered structure, UT does not provide accurate depth information: the detected depths of delaminations do not agree with the actual values, which can be seen in Figure 6(h). Besides, the measured diameters of the delaminations vary at different depths or positions, which lead to inaccurate indications of the dimension and location of the delaminations. The experiment shows the limitations of UT for composite materials that (1) multiple reflection and scattering in composites; (2) large penetration and scattering loss; (3) inaccurate measurement for thin sample; (4) contact and liquid coupling are required.

To achieve better visualisation of the defects, guided wave C-scans using a phase array can reduce the multiple reflections and scattering for accurate depth measurement. However, the scanning time and data amount could increase significantly, which does not satisfy the requirement for online monitoring or structural health monitoring, compared with PEC-stimulated or flash thermography.

4.4. Eddy Current Scanning Results. The eddy current scanning image for sample 1 is shown in Figure 7. The EC probe consists of 8-by-2-coil array, working from 1 kHz to 25 kHz with 3.5 mm spatial resolution. No significant patterns of delaminations are observed on the samples. Results show that the sensitivity of the EC scanning system is not high enough to detect the eddy currents at the delamination of the composite with low conductivity.

4.5. Comparison and Discussion

(1) Detection Ability for Detected Depth. From the experiments, the ultrasonic scanning approach detects the delaminations in all of the samples; PEC-stimulated thermography

(a)   (b)   (c)
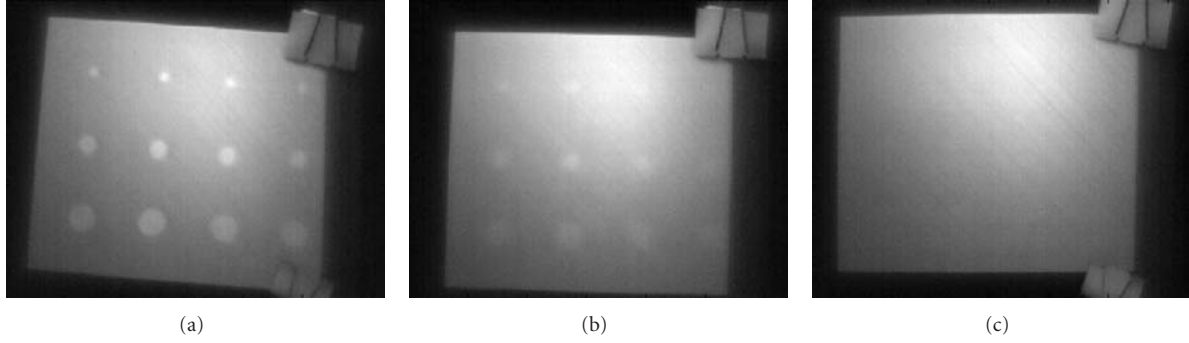
FIGURE 5: Flash thermography images at maximum heating (5 seconds): (a) sample 1; (b) sample 2; (c) sample 3.

(a)   (b)   (c)   (d)

(e)   (f)   (g)   (h)
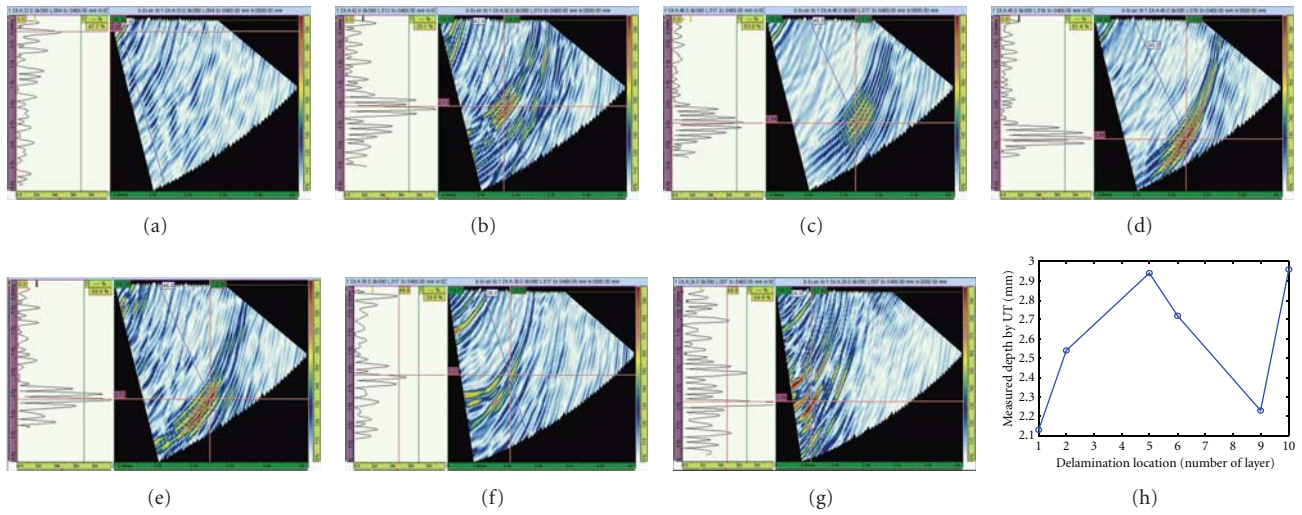
FIGURE 6: UT scanning results: (a) no delamination; (b) 155 μm deep delamination; (c) 310 μm deep delamination, (d) 775 μm deep delamination; (e) 930 μm deep delamination; (f) 1395 μm deep delamination; (g) 1550 μm deep delamination; (h) actual and measured delamination depth.
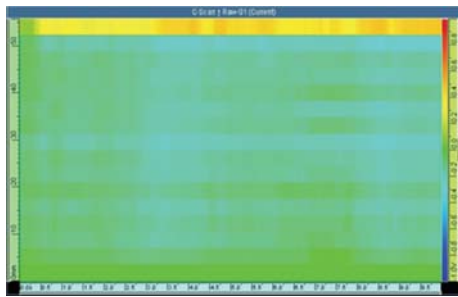
FIGURE 7: EC scanning image of sample 1.

and flash thermography detect delaminations in samples 1 and 2 only, while EC scanning detected no delaminations. Therefore, UT scanning has the best detection ability amongst the four methods.
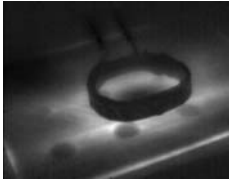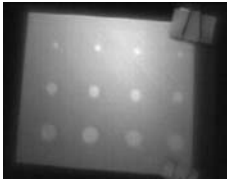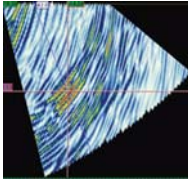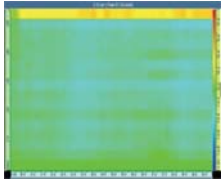
(2) Fibre Orientation. PEC-stimulated thermography can be used to observe fibre orientations through thermal images. The highlighted lines in the sample surface indicate the fibres

in the surface and subsurface layers. UT scanning and flash thermography both fail to show fibre orientation.

(3) Visualisation of Defects. PEC-stimulated thermography and flash thermography can provide good visualisation of a defect, allowing us to know its shape and dimensions (except thickness). Although UT scanning can also provide imaging by the way of a reconstruction algorithm, it is time-consuming and the image suffers from massive attenuation, multiple reflection, and scattering of the ultrasound waves.

(4) Inspection Time and Cost. PEC-stimulated thermography and flash thermography can provide the inspection within second scale to observe defects, whilst UT scanning requires minutes or hours with a large amount of data. These two thermographic methods are superior to satisfy the requirement for online monitoring or structural health monitoring. Besides, the cost of UT scanning system and probe itself is much higher than PEC-stimulated thermography or flash thermography.

TABLE 1: Comparison of PEC-stimulated thermography, flash thermography, and UT/EC scanning.

	PEC stimulated thermography	Flash thermography	UT scanning	EC scanning
Image for sample 1				
Detected depth	Up to 930 μm deep	Up to 930 μm deep	Up to 1550 μm deep	None
Fibre orientation	Good	No	No	—
Defect visualisation	Good	Good	Not good	—
Inspection time	~Seconds	~Seconds	~Minutes to hours	—
Cost	Low	Low	High	—

The comparison of these four approaches investigated is summarised in Table 1.

5. Conclusion and Future Work

In this paper, man-made delaminations in samples 1 and 2 at 155 μm, 310 μm, 775 μm, and 930 μm deep have been observed through the new developed PEC-stimulated thermography at NUAA system. However, deeper delaminations in sample 3 (1395 μm and 1550 μm deep) could not be seen clearly from the raw thermal videos. Both UT/EC scanning and flash thermography have also been carried out at NUAA for comparison. Results showed (1) only enables PEC-stimulated thermography to observe the fibre orientation for surface and subsurface layers, giving the potential for minor defect detection for example, fibre breakage; (2) although PEC-stimulated thermography and flash thermography did not detect the delamination deeper than 930 μm, they offer rapid inspection and better visualisation of delaminations from transient thermal images/videos.

The UT experiment shows the limitations of this approach for composite materials, due to (1) multiple reflections and scattering in composites, (2) inaccurate measurement for thin samples, (3) liquid coupling is required. PEC-stimulated thermography and flash thermography can be considered as two powerful approaches for delamination detection. In concern with fibre orientation evaluation and other typical defects in composite materials, for example, impact damages, cracks, PEC-stimulated thermography is more sensitive to those defects, especially cracks [23]. Therefore, PEC-stimulated thermography with low specification of camera has been proven as a good candidate for CFRP delamination detection, where thermal and electrical conductivity are evaluated. Different defects can be evaluated using PEC-stimulated thermography systems in the future.

In future work, more powerful excitation for deeper delamination detection: pulse width, inductor geometry, and directions for PEC-stimulated thermography will be investigated to detect deeper delaminations. Post-image/video processing to enhance the contract of delamination including removal of direct heating from excitation coils and background in the images/videos for thermography and feature extraction for the transient image response and patterns will be further considered and developed.

References

[1] T. E. Michaels and B. D. Davidson, "Ultrasonic inspection detects hidden damage in composites," *Advanced Materials and Processes*, vol. 143, no. 3, pp. 34–38, 1993.

[2] H. Kocznarech, "Ultrasonic detection of damage in carbon fibre reinforced plastics," *Journal of Composite Materials*, vol. 29, pp. 59–95, 1995.

[3] D. E. Chimenti and A. H. Nayfeh, "Leaky Lamb waves in fibrous composite laminates," *Journal of Applied Physics*, vol. 58, no. 12, pp. 4531–4538, 1985.

[4] S. H. Rhee, J. K. Lee, and J. J. Lee, "The group velocity variation of Lamb wave in fiber reinforced composite plate," *Ultrasonics*, vol. 47, no. 1–4, pp. 55–63, 2007.

[5] E. Jasiüniené, R. Raišutis, R. Šliteris et al., "NDT of wind turbine blades using adapted ultrasonic and radiographic techniques," *Insight*, vol. 51, no. 9, pp. 477–483, 2009.

[6] A. Ghoshal, W. N. Martin, M. J. Schulz, A. Chattopadhyay, W. H. Prosser, and H. S. Kim, "Health monitoring of composite plates using acoustic wave propagation, continuous sensors and wavelet analysis," *Journal of Reinforced Plastics and Composites*, vol. 26, no. 1, pp. 95–112, 2007.

[7] M. Giordano, A. Calabro, C. Esposito, A. D'Amore, and L. Nicolais, "An acoustic-emission characterization of the failure modes in polymer-composite materials," *Composites Science and Technology*, vol. 58, no. 12, pp. 1923–1928, 1998.

[8] A. Sophian, G. Y. Tian, D. Taylor, and J. Rudlin, "Electromagnetic and eddy current NDT: a review," *Insight*, vol. 43, no. 5, pp. 302–306, 2001.

[9] R. Grimberg, D. Prémel, A. Savin, Y. Le Bihan, and D. Placko, "Eddy current holography evaluation of delamination in carbon-epoxy composites," *Insight*, vol. 43, no. 4, pp. 260–264, 2001.

[10] S. Kharkovsky, J. T. Case, M. A. Abou-Khousa, R. Zoughi, and F. L. Hepburn, "Millimeter-wave detection of localized anomalies in the space shuttle external fuel tank insulating foam," *IEEE Transactions on Instrumentation and Measurement*, vol. 55, no. 4, pp. 1250–1257, 2006.

[11] C. Ibarra-Castanedo, J. M. Piau, S. Guilbert et al., "Comparative study of active thermography techniques for the nondestructive evaluation of honeycomb structures," *Research in Nondestructive Evaluation*, vol. 20, no. 1, pp. 1–31, 2009.

[12] N. P. Avdelidis and D. P. Almond, "Through skin sensing assessment of aircraft structures using pulsed thermography," *NDT and E International*, vol. 37, no. 5, pp. 353–359, 2004.

[13] N. P. Avdelidis, C. Ibarra-Castanedo, X. Maldague, Z. P. Marioli-Riga, and D. P. Almond, "A thermographic comparison study for the assessment of composite patches," *Infrared Physics and Technology*, vol. 45, no. 4, pp. 291–299, 2004.

[14] G. Busse and P. Eyerer, "Thermal wave remote and nondestructive inspection of polymers," *Applied Physics Letters*, vol. 43, no. 4, pp. 355–357, 1983.

[15] R. Mulaveesala and V. S. Ghali, "Cross-correlation-based approach for thermal non-destructive characterisation of carbon fibre reinforced plastics," *Insight*, vol. 53, no. 1, pp. 34–36, 2011.

[16] N. P. Avdelidis, B. C. Hawtin, and D. P. Almond, "Transient thermography in the assessment of defects of aircraft composites," *NDT and E International*, vol. 36, no. 6, pp. 433–439, 2003.

[17] S. M. Shepard, J. Hou, J. R. Lhota, and J. M. Golden, "Automated processing of thermographic derivatives for quality assurance," *Optical Engineering*, vol. 46, no. 5, Article ID 051008, 2007.

[18] V. P. Vavilov, D. A. Nesteruk, and V. S. Khorev, "IR thermographic NDT research at Tomsk Polytechnic University, Siberia, Russia," in *50th Annual Conference of The British Institute of Non-Destructive Testing*, Telford, UK, 2011.

[19] I. Zainal Abidin, G. Yun Tian, J. Wilson, S. Yang, and D. Almond, "Quantitative evaluation of angular defects by pulsed eddy current thermography," *NDT and E International*, vol. 43, no. 7, pp. 537–546, 2010.

[20] M. Noethen, K. J. Wolter, and N. Meyendorf, "Surface crack detection in ferritic and austenitic steel components using inductive heated thermography," in *33rd International Spring Seminar on Electronics Technology (ISSE '10)*, pp. 249–254, May 2010.

[21] B. Oswald-Tranta and G. Wally, "Thermo-inductive surface crack detection in metallic materials," in *9th European Conference on NDT*, Berlin, Germany, 2006.

[22] S. Yang, G. Y. Tian, I. Z. Abidin, and J. Wilson, "Simulation of edge cracks using pulsed eddy current stimulated thermography," *Journal of Dynamic Systems, Measurement and Control*, vol. 133, no. 1, Article ID 011008, 2011.

[23] L. Cheng and G. Y. Tian, "Surface crack detection for carbon fiber reinforced plastic (CFRP) materials using pulsed eddy current thermography," *IEEE Sensors Journal*, vol. 11, no. 12, pp. 3261–3268, 2011.

[24] B. Ramdane, D. Trichet, M. Belkadi, and J. Fouladgar, "3-D numerical modeling of the thermo-inductive technique using shell elements," *IEEE Transactions on Magnetics*, vol. 46, no. 8, Article ID 5512872, pp. 3037–3040, 2010.

Research Article

Development of a Nondestructive Impulse Device and Damage Model for Unreinforced Concrete

Shane D. Boone, Paul J. Barr, James A. Bay, and Marvin W. Halling

Department of Civil and Environmental Engineering, Utah State University, 4110 Old Main Hill, Logan, UT 84332-4110, USA

Correspondence should be addressed to Paul J. Barr, paul.barr@usu.edu

Unconstrained compression waves were measured using a newly developed, nondestructive, short impulse excitation device developed for long-term structural health monitoring. The measurements, using this innovative device, were used to determine the variation in the first longitudinal modal frequency as a function of loading magnitude and loading cycles to failure of various concrete mixes. Longitudinal frequency and cumulative energy variations were found to be a function of concrete compressive strength. These results imply that higher-strength concrete more easily absorbs energy and restricts the growth of microcracks. Based on the results, a new damage model is proposed that was shown to correlate with measured values to within 7%. This proposed model was found to have a closer correlation than Miner's hypothesis and damage index models from other reviewed research.

1. Introduction

Testing methods that determine the in-place physical properties of concrete structures are important tools for engineers to quantify their capacity and long-term performance. Code-based procedures that result in the evaluation of the integrity of existing structures depend on accurate material properties to correctly determine the condition of these structures. Currently, there are many such methods (i.e., stress wave propagation methods) in existence that allow engineers to determine these material properties. However, these tools and techniques have been developed based on the assumption that dynamic material measurements are not affected by the inherent stress history applied to structures due to self-weight, super-imposed dead loads, and live loads. Such loading causes fatigue and damage in the form of microcracking that can change the long-term structural health with regard to wave propagation. These long-term changes in the propagation velocities of stress waves must be clearly understood so that nondestructive measurements of existing structures are not only quantitative but also correctly analyzed.

In the case of a heterogeneous material like concrete, the assumption that it is homogenous is accepted in order for the basic theories and techniques of stress wave propagation methods to be applicable. However, the measured stress waves are typically too large in length to determine properties such as porosity, interfacial bond quality between aggregate and matrix material, or the presence of microcracks. Instead, the wave characteristics measured during these tests represent the average physical properties of the concrete structure or specimen analyzed (i.e., a homogenous measurement).

When concrete is loaded with any significant amount of stress, tensile stresses are produced and microcracks form. Stress, in this case, can result from any type of loading, including those induced during the curing process such as bleeding, settling of grout, and shrinkage. These stress-induced cracks typically initiate around the aggregate-to-matrix interfaces and then progress as additional loads are applied. It is this microcrack growth and coalescence that causes the failure of concrete [1]. Because the accumulation of microcracks leads to the failure of concrete, it is reasonable to assume that the accumulation of these cracks is a good indicator of damage.

Several methods have been developed to predict the damage in concrete structures due to loading. The majority of these models use energy-related damage indicators to

quantitatively assess the damage in such structures [2–5]. Also, other researchers [6] have developed relationships for the calculation of fatigue of unreinforced concrete to incorporate indicators such as stress versus number of cycles, ratio of minimum to maximum stress, and rate of loading. Other predictive models have used various indicators such as splitting tensile strength [7], stress-strain relationships [8–10], and strain-cycle relationships [11].

As cycling and fatigue loading is applied to concrete, the primary reason for a decrease in the structural-related properties is the continuous microcrack growth. Thus, research interest to investigate procedures to measure the growth of these cracks has been conducted [12–14]. All of these studies have incorporated nondestructive testing (NDT) techniques to quantify crack growth as a function of loading cycles. Measurements of pulse velocity, acoustic emission, and ultrasonic wave attenuation are methods that have been used to determine the growth of microcracks. All of these methods use similar techniques that initially excite the specimens and subsequently measure the elastic wave characteristics of the material during and after the specified loading cycles. The free-free resonant column (FFRC) method has traditionally been used to quantify damage in terms of the fundamental longitudinal, transverse, and torsional frequencies as well as damping [15]. The results from all of the NDT research indicate that measurements of elastic wave properties are a good indicator of damage in concrete.

A more recent study [16] indicates that the elastic properties of the material are dependent not only on the growth of microcracks but also on the closing of microcracks. Some researcheres [16] have shown in a feasibility study that surface wave velocities propagating parallel to the direction of loading demonstrate a distinct stress sensitive behavior. During this study, surface wave velocities were measured while concrete specimens were uniaxially loaded to 35% and 80% of the ultimate compressive strength. Results indicate that as stress levels increase, microcracks in the specimens close and the surface wave velocities increase.

There is also an anisotropic behavior of elastic waves in loaded concrete specimens that depends on the direction of loading relative to the direction of wave propagation [16]. Thus, the presence of microcracks forming in the same direction of loading can be measured by determining the changes in stress wave propagation in that direction.

Studies that have used the FFRC method to monitor the decrease in fundamental longitudinal, transverse, and torsional frequencies have shown that for a specific concrete mix, these natural frequencies decrease [15]. However, a trend to quantify this reduction has not been determined. It is the goal of this study to develop a nondestructive, easily employed, impulse device that can be used to determine whether a general trend exists between parameters such as the first longitudinal modal frequency as a function of applied load. This relationship will be investigated as a function of concrete compressive strength. The nondestructive impulse device and measured data will provide engineers a new tool to continue the development of the understanding of long-term, structural health monitoring of concrete subjected to repeated loading.

In order to obtain the necessary data, the variations in longitudinal compression wave velocity and energy absorption of a variety of concrete specimens subjected to fatigue loading conditions were investigated. The details of the newly developed nondestructive device, concrete mixes, instrumentation, experimental setup, and the methods of measurement and analysis are provided. The theoretical background applying to wave propagation in elastic solid media is briefly discussed. The measurement results of the changes in dynamic properties as well as the cumulative energy absorbed during cyclic loading of several concrete mixes are presented and a new relationship to predict damage accumulation is developed and compared with existing relationships. This newly proposed relationship is shown to more accurately predict the behavior between damage and fatigue loading in comparison to previously developed relationships.

2. Instrumentation Development

In order to be able to obtain frequency measurements more efficiently during the concrete testing, a new nondestructive excitation device was developed. There were several iterations of the design during the development of the new excitation device. However, throughout all the iterations the core design philosophy remained consistent. When a copper coil is subjected to a voltage, a magnetic field is produced. By placing a series of magnets within this copper coil, the magnets are forced to move directly with the change in voltage. When the magnets reside in a free boundary condition, they move up and down within the coil. However, when one or more of the boundary conditions are fixed, they exert an impulse on that fixed-end surface. By placing a spring loaded series of magnets within a copper coil, the free end of the magnets can be set against a surface in order to exert a short-duration impulse force against it. Thus, it was decided to build a device to produce short duration impulse forces using these concepts. The core design consisted of a spring-loaded series of magnets surrounded by a copper wire coil.

Originally, the coil and magnets were fitted into a PVC housing to provide the coil and springs a fixed position. This housing was intended to sit flush against one end of the concrete cylinder to force the magnets against the concrete surface as it was loaded cyclically. This would ensure that the impulses produced by the movements of the magnets would exert a force onto the cylinder. Because the PVC housing could not support the applied loads to which it was subjected during the tests, a specialized aluminum end plate was fabricated to allow the device to sit on the end of the concrete specimen during compression tests. A similar aluminum end plate was fabricated so that a unidirectional accelerometer could be mounted on the opposite end to measure the wave propagation created by the excitation device. These end plates were designed so that they would work with a typical end capping plate used during standard concrete specimen compression tests. However, there was a hole in the center of each end plate where the device sat during compression tests.

It was quickly discovered that the PVC housing simply was not rigid enough to provide adequate protection for the magnetic coil. The neoprene pads that are typically placed

FIGURE 1: Final design of the excitation device.

FIGURE 2: Final configuration for the experiment (LVDT on right, excitation device on left, concrete cylinder fitted with an extensometer yolk, and capped specialized aluminum end plates; the accelerometer was mounted on top of cylinder inside the end plate).

in the end capping plates were continuously compressing the PVC housing during the compression tests causing the entire device to be crushed. Therefore, the design was reduced in size to avoid being crushed by the neoprene pads. The new design consisted of two small steel plates connected to a series of magnets surrounded by a small copper coil. The entire assembly was then protected with a thin plastic tube. The plastic tube restricted the movement of the copper coil; however, and the modified design was disregarded.

The original design was then modified to include a stronger housing. Several copper coils were made and fit into aluminum and steel tube housings. However, the end of the coils was continuously crushed during the compression tests. A coil was then fit into a steel housing and potted with epoxy for protection. This design worked adequately initially, but due to the creep of the epoxy, the coil crushed inwards under load towards the spring-loaded magnet assembly and the magnets were not able to freely move. Finally, an aluminum tube was placed on the interior of a magnetic copper coil that was housed in a steel tube. The entire assembly was potted with 17.2 MPa (2500 psi) epoxy. The steel housing was comprised of a hollowed out 38.1 mm (1.5 in.) circular steel member. The walls of the housing were 5 mm (0.2 in.) thick. The aluminum tube had a 13 mm (0.5 in.) outer diameter and the walls were approximately 1.7 mm (0.1 in.) thick. The epoxy potting extended approximately 8 mm (0.3 in.) from the top of the steel housing making the entire structure approximately 41 mm (1.6 in.). The magnetic core was comprised of three 6 mm × 5 mm (0.3 in. × 0.2 in.) neodymium magnets wrapped and fitted in shrink tube. This final design of the excitation device allowed continuous measurements while the specimen was being subjected to cyclic loads. The final design is shown in Figure 1.

Because of the intense pressures associated with the cyclic compression tests, it was discovered that the recorded data also included a great deal of background noise. As a result, it was very difficult to interpret the correct longitudinal frequencies and associated half power bandwidths. An experiment to mount the excitation device on the side of the specimen was conducted, and it was found that adequate energy
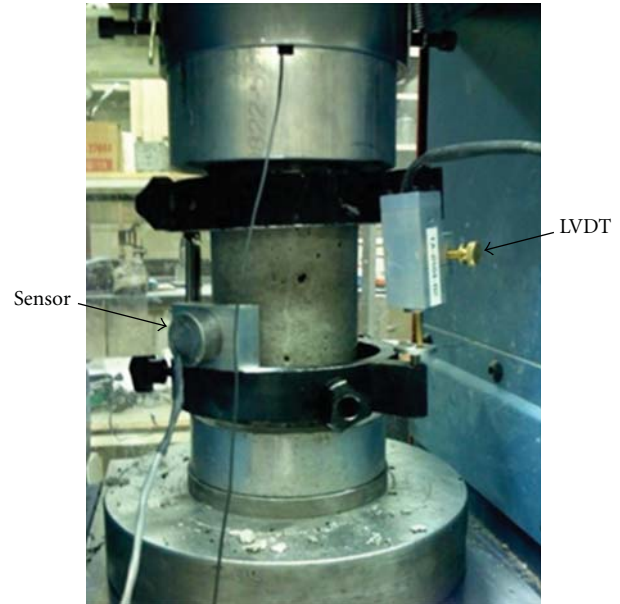
was produced in the longitudinal direction to allow for this configuration. Another benefit of this side attachment was that the device could be attached to concrete specimens other than cylinders to monitor the structural health. The excitation device was placed into an aluminum housing to increase the long-term durability. Figure 2 shows the excitation device attached to the side of a concrete cylinder along with an extensometer to measure static axial stress-strain behavior during the cyclic tests. This configuration was used throughout all the testing.

3. Experiment

A compression machine controlled by a servo unit capable of loading and unloading the concrete specimens at regulated rates was used to apply the predetermined force to the cylinders at specified percentages of their ultimate compression strength. Simultaneously, the linear voltage displacement transducer (LVDT) on the extensometer-measured changes in axial length that was used to calculate strain. From this data, load-deflection hysteretic curves were created so that a comparison between changes in fundamental frequency and energy dissipation could be obtained. Before and after each loading cycle, the excitation device was turned on and readings of the first longitudinal modal frequency and the half power bandwidth were measured. Each concrete cylinder was then immediately reloaded. Cylinders were repeatedly tested in this manner until failure.

In all, five concrete mixes were tested which included the effects of multiple aggregate types, water-to-cement ratios, and different cement types. This variation in concrete mixes

TABLE 1: Mix designs for 0.5 cubic feet and 28-day compressive strengths.

Mix	Cement (lbs.)	Fly Ash (lbs.)	Course aggregate (lbs.)	Fine aggregate (lbs.)	Water (lbs.)	w/c ratio	f_c' (psi)
Low strength	9.5	0.0	0.0	70.0	4.9	0.51	1880
Low/medium strength	12.6	0.0	38.6	34.0	5.4	0.43	3800
Medium strength	10.3	1.9	25.1	29.7	5.0	0.48	5350
Medium/high strength	13.2	3.3	29.4	19.0	5.2	0.39	8920
High strength	Proprietary						12560

was chosen in order to measure changes in concrete properties representing a wide range of compressive strengths. The concrete designs ranged in mix proportions and had 28-day compressive strengths ranging from 13.0 to 86.6 MPa (1880 to 12560 psi) (Table 1). Concrete specimens were 100 mm × 200 mm and 151 mm × 301 mm (4 in. × 8 in. and 6 in. × 12 in.) cylinders.

Typical stress-strain curves plotted from measurements of the concrete specimens, when loaded in compression, are assumed to be approximately linear up to roughly 40% of the compressive strength. Thus, cylinders were cyclically tested at loads ranging from 50% to 90% of the compressive strength to allow for a broad testing range of the concrete specimens. In order to produce an ideal experiment, several criteria were established. First, the specimens were loaded to a range at which the measured stress-strain curve became nonlinear, ensuring some type of irreversible damage. Secondly, the desired range of cycles was set to be more than 5, but less than 100. This was to ensure an efficient experiment. Finally, the desired failure would occur gradually, rather than during a single cycle. This final criterion was put into place in an effort to quantify the final stages of damage before failure.

After testing several specimens, it was decided that the most effective and efficient experiment would be as follows. Four cylinders from each strength class were loaded cyclically with an initial load at 80% of their respective ultimate compressive strength. The load was increased each cycle in 1% increments up to 90%. Once the 90% mark was reached, the cylinders were loaded cyclically at that magnitude until failure. This experimentation procedure was selected because it allowed for the results of four cylinders from each strength class to be averaged, exceeding the recommended statistical requirement of three cylinders set forth by ASTM C39. Additionally, it was found that loading the cylinders cyclically at magnitudes less than 80% of the ultimate compressive strength did not induce a very large change in the baseline first mode longitudinal frequency. After each cycle, longitudinal frequencies were measured using the newly developed excitation device, acceleration transducer, and digital signal analyzer.

In addition to monitoring the longitudinal frequency, an extensometer with an LVDT was used to measure the axial displacement of the concrete samples as they were cyclically loaded. These load and displacement measurements were subsequently used to produce hysteretic curves that allowed for the calculation of the energy absorbed by the concrete specimen during each cycle.

4. Results

Changes in the fundamental frequency were used to quantify damage accumulation, as the concrete specimens were cyclically loaded to failure. The fundamental frequency of each specimen was calculated based on the principle that when an excitation is produced at a point on an elastic medium, waves radiate from the point where the disturbance occurred in all directions. At great distances from this point of disturbance, however, it may be assumed that all particles are moving either parallel to the direction of the wave propagation or perpendicular to that direction. The particles that are moved in a parallel manner are moved by waves of dilation and produce longitudinal waves [17]. The relationship between the rod (parallel) wave velocity and the properties of the concrete can be described using (1);

$$V_{\text{Rod}} = \frac{V_p}{\sqrt{1 - \nu/((1 + \nu)(1 - 2\nu))}} = \sqrt{\frac{E_d}{\rho}}, \tag{1}$$

where V_{Rod} is the rod wave velocity, V_p is the compression wave velocity of the material, ν is the poison's ratio, E_d is the dynamic Young's modulus of the concrete, and ρ is the mass density of concrete.

Because (1) shows that the rod-wave velocity is dependent on the dynamic modulus of elasticity, E_d, it is apparent that as the stiffness of a material deteriorates (microcracks grow), the rod-wave velocity will also decrease. When a disturbance is produced on a known cross-section and length, l, the first longitudinal modal frequency (rod-wave velocity) can be described as [18]

$$V_{\text{Rod}} = f_l \lambda, \tag{2}$$

where f_l is the first longitudinal modal frequency, and λ is the wavelength, $2l$.

Thus, by measuring the first longitudinal modal frequency of a specimen, the stiffness of that material (E_d) can be determined. Also, as the stiffness varies due to an increase in the number and growth of the microcracks, this variation can be quantified by measuring the first longitudinal modal frequency.
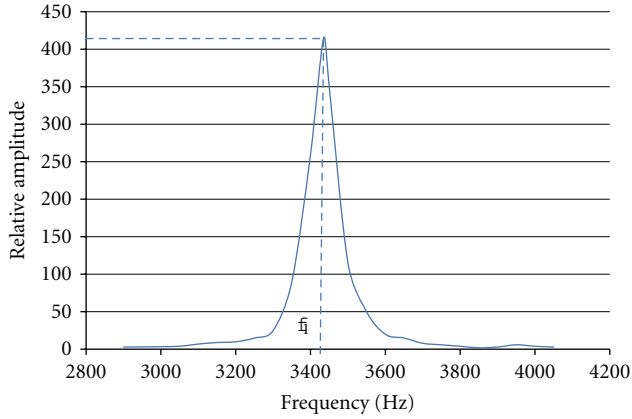
FIGURE 3: Typical frequency plot and the half power bandwidth.

FIGURE 4: First longitudinal modal frequency as a function of percentage failure.

TABLE 2: Frequency divided by initial frequency.

Mix	f_i/f_o
Low strength	89.11%
Low/medium strength	90.36%
Medium strength 1	90.13%
Medium/high strength	92.53%
High strength	93.30%

Measurements of the first longitudinal modal frequencies were recorded at the end of each cycle on every concrete specimen. Simultaneously, load and deflection measurements were recorded using the extensometer and LVDT during each cycle. Initial, undamaged frequencies, f_o, were measured before any loading occurred and was used as baseline data. The percent decrease in frequency was determined by dividing each subsequent measured frequency, f_i, by this initial frequency. The percentage of failure was taken as the cycle number divided by the total number of cycles required for failure.

A typical frequency versus amplitude plot is presented in Figure 3. As displayed in Figure 3, there was little background noise due to the efficiency of the new nondestructive impulse device. This figure also shows the location of the first longitudinal modal frequency, f_i, for use in (2). Based on the output from these plots, the first longitudinal modal frequency could be determined for each concrete specimen. Measured frequencies were plotted against the percentage of failure. Figure 4 presents the general trend of decreasing frequencies as a function of damage (increase in microcracks) for each of the examined concrete mixes. The individual mixes exhibit varying rates of decrease in longitudinal frequency. The values of these variations are listed in Table 2. The data indicates that as concrete compressive strength and therefore tensile strength increase, the percentage loss of first longitudinal modal frequency due to cyclic loading generally decreases. This is presumably due to the increased concrete strength and the inherent reduction in microcracking associated with an increase in tensile strength and stiffness. A discrepancy arises when comparing the low/medium strength and medium strength 1 concrete mixes. Although these two concrete mixes vary in compressive strength by 10.7 MPa (1550 psi), the stronger of the mixes exhibited a higher percentage loss of the first mode longitudinal frequency. After further investigation, it can be noticed that the mixes are very different and that the w/c ratio of the stronger concrete is higher than the weaker concrete. This discrepancy indicates that not only the strength but also the mix ratios could be a factor in the decrease in dynamic properties.

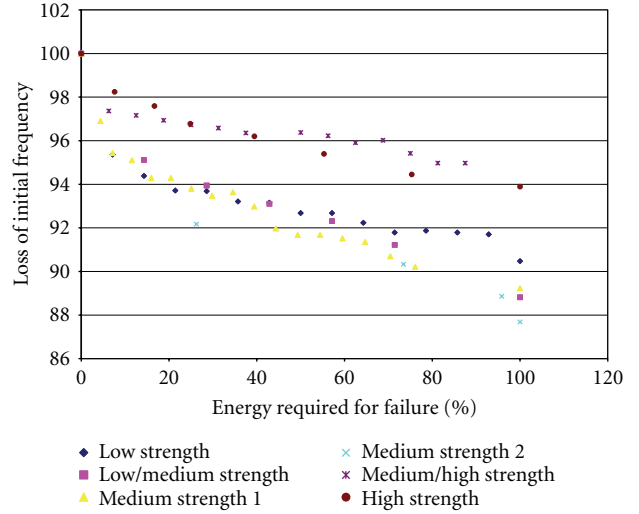Examination of Figure 4 shows that the longitudinal frequency of any of the concrete mixes decreases as a function of increasing loading. This decrease in fundamental frequency is believed to be a result of microcracks developing in the concrete paste resulting in the degradation of stiffness in the material. As the specimens continued to be cyclically loaded, microcrack growth continued, the concrete became more fatigued, and the longitudinal frequency continued to decrease. Eventually, the coalescence of the microcracks reached a point at which the concrete specimen failed. Figure 4 shows that a trend between the decrease in longitudinal frequency with applied loading and concrete strength is consistent. This conclusion is further supported by the average decrease in longitudinal frequency presented in Table 2. These percent decreases represent the average amount of frequency loss measured on the four cylinders from each concrete mix at the point of failure.

The amount of absorbed energy experienced by the concrete during each cycle was calculated from the hysteretic curves measured using the LVDT and extensometer instrumentation. The hysteretic curve represents the amount of axial deflection that is measured for a specific axial load. By measuring the area within the curve, the amount of absorbed energy was quantified for each load cycle. Figure 5 presents the measured energy for each concrete mix as a function of applied load (cumulative damage). The parabolic curve presented indicates that the damage index is nonlinear as predicted by Minor's hypothesis, but of a higher order. The values for the total cumulative energy for each concrete mix
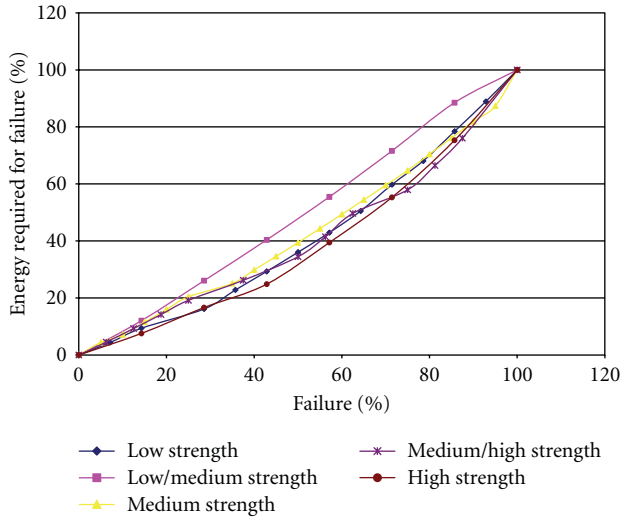
FIGURE 5: Cumulative energy percentage required as a function of damage.

FIGURE 6: Change in frequency response as a function of compressive strength.

TABLE 3: Average values of total energy increase per concrete strength.

Mix	Average total cumulative energy (ft.-lb.)
Low strength	1262
Low/medium	2318
Medium strength 1	2925
Medium/high strength	2684
High strength	3528

are presented in Table 3. This data indicates that as the concrete strength and associated stiffness increase per mix, the amount of energy ultimately required to cause failure also increases. The compressive strength increase in concrete mixes is typically associated with an increase in strength of the concrete paste. Thus, as the strength of the matrix material increases, the amount of energy required to expand the microcracks that form at the boundary between the matrix material and the aggregate increases. This trend is evident due to the general increase of total cumulative energy required to cause failure presented in Table 3. Again, there is a discrepancy when comparing the low/medium strength and medium strength 1 concrete mixes that is possibly due to specific effects of individual mix ratios.

Thus, as concrete strength increases, the total amount of required energy absorption to cause failure increases. This relationship demonstrates that higher-strength concrete mixes have the ability to absorb more energy during their service life (Table 3). This implies that as the bond between the concrete paste and aggregate increases due to increased concrete strength, more energy is absorbed in modes other than the formation of microcracks.

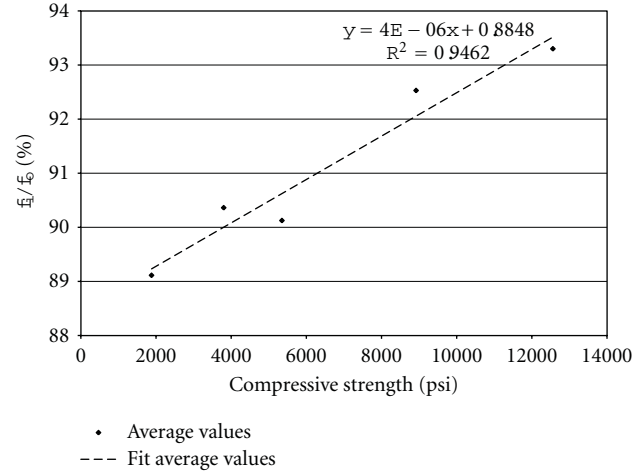Figure 6 presents the total average percentage loss of initial frequency as a function of concrete compressive strength. Each data point represents the average of the total loss measured from the four cylinders tested from each compressive strength class at failure. Within each compressive strength class, total frequency loss differed by a maximum of 3.5%. When these values were plotted as a function of compressive strength, a correlation factor of 0.95 was determined. These results indicate that as microcracks develop and grow as loading increases, the first longitudinal modal frequency decreases and is an excellent indicator of damage in concrete specimens as a function of concrete compressive strength.

Figure 7 presents the measured trends of total cumulative energy required to fail a concrete specimen of specific strength. With each ensuing cycle, more damage occurred in the concrete. By measuring the total amount of energy absorbed during all cycles, the total amount of energy that can be absorbed by a specific strength concrete can be determined. Once again, each data point represents the average cumulative energy absorbed from the measurements on the four cylinders from each strength class. The general trend indicates that as compressive strength increases, the total amount of energy required to fail a specimen increases. Within each compressive strength class, cumulative energy absorption differed by a maximum of 11%. When these values are plotted as a function of concrete compressive strength, a correlation factor of 0.75 was obtained.

Finally, the total amount of energy calculated from each measured hysteretic curve is plotted as a function of percentage of failure (Figure 8). The percentage of failure was calculated by dividing the number of current cycles, N, by the total number of cycles required to fail the cylinder, N_f. This plot presents the determined energy from the extensometer and LVDT from each cycle on all concrete specimens. The trend for the data is exponential, which indicates that it requires less energy (loads) to develop small values of damage (cracks). However, as indicated by the exponential trend of the data, higher amounts of energy are required to induce additional damage. With a correlation of coefficient for all data of 0.95, this plot illustrates that the amount of energy
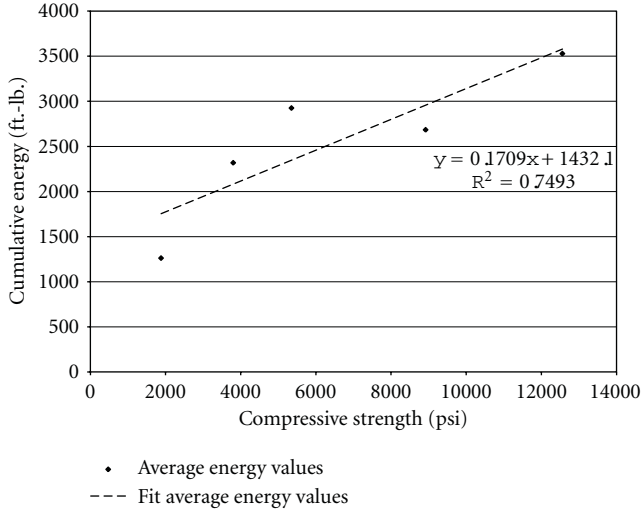
Figure 7: Cumulative energy required for failure as a function of compressive strength.
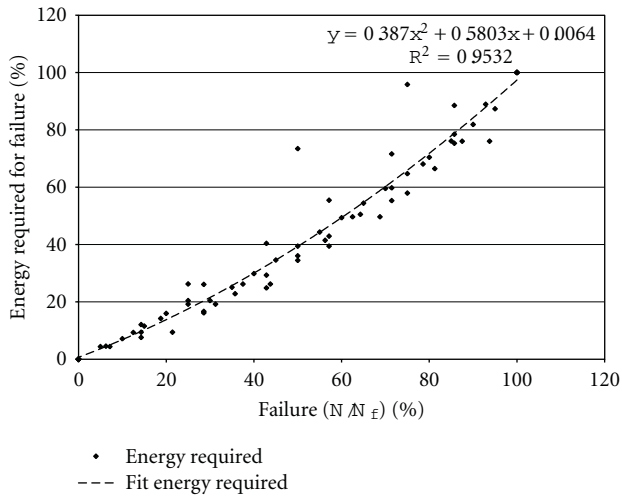

Figure 8: Percentage of total cumulative energy as a function of percentage of failure.

absorbed by a concrete specimen can be used an excellent indicator of damage accumulation.

5. Proposed Damage Model

Based on the research results, it was concluded that both changes in fundamental frequency and absorbed energy were excellent indicators of damage accumulation in unreinforced concrete specimens. Thus, both contributing factors were combined to determine a proposed damage model.

Combining the results presented in Figures 6 through 8, an indicator of damage can be developed as functions of compressive strength, energy, and frequency variation for unreinforced concrete. For the explanation provided hereinafter, some rounding occurred while going from scientific

notation. From the fitted trend line presented in Figure 8, (3) was developed as

$$\frac{E_i}{E_f} = 0.39D^2 + 0.58D, \tag{3}$$

where E_i is the energy measurement at cycle i, E_f is the total cumulative energy required for failure of the specimen, and D is the percentage of damage.

From the fitted trend line in Figure 7, (4) was listed as

$$E_f = 0.17f_c' + 1500, \tag{4}$$

where f_c' is the the compressive strength of the specimen.

Finally, from the trend line presented in Figure 6, (5) was listed as

$$\frac{f_i}{f_o} = 4 \times 10^{-6} f_c' + 0.89, \tag{5}$$

where f_o is the initial frequency, and f_i is the frequency measurement after cycle i.

Equation (5) can be solved in terms of $f_c' =$ as (6):

$$f_c' = \frac{(f_i/f_o) - 0.89}{4 \times 10^{-6}}, \tag{6}$$

and by substituting (6) into (4), the following relationship was obtained as (7):

$$E_f = 45900\left[(f_i/f_o) - 0.89\right] + 1280. \tag{7}$$

Substituting (7) into (3), an equation to determine the percent damage of a concrete specimen based on the measured first longitudinal modal frequency and hysteretic energy is

$$\frac{E_i}{45900\left[(f_i/f_0) - 0.89\right] + 1280} = 0.39D^2 + 0.58D. \tag{8}$$

Finally, solving (8) in terms of damage, the proposed damage relationship is

$$D =$$

$$\frac{0.0075\left[\sqrt{E_i + 9690\left((f_i/f_0) - 0.86\right)} - 99.90\sqrt{(f_i/f_0) - 0.86}\right]}{\sqrt{(f_i/f_0) - 0.86}}. \tag{9}$$

Using the proposed relationship and measured values of energy and frequencies, Figure 9 presents a precise comparison between the newly proposed damage relationship calculated using (9) and the cyclic failure ratio. In Figure 9, the damage index calculated and presented on the y-axis presents calculated data based on the data measured at a specific cycle. This damage index is then plotted per cyclic ratio to failure (N/N_f displayed on the x-axis). The data in Figure 9 exhibits a parabolic trend indicating that more damage is required during later cycles of loading. This ideology is consistent with the fact that microcracks first form during initial stages of damage, and then grow exponentially towards
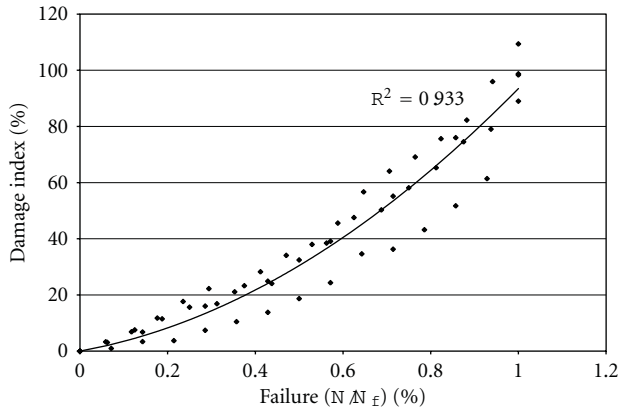
FIGURE 9: Damage calculated by (9) as a function of the percentage of failure calculated from measured values.

FIGURE 10: Damage calculated from proposed equation compared with other known damage indices.

failure. Thus, early stages of cyclic loading are associated with lower values of damage and as more loading cycles are applied, an exponential increase in damage is induced upon the specimen. Figure 10 presents a comparison of the damage index calculated using the proposed relationship in addition to several other previously proposed relationships as a function of the percentage of failure. Values calculated with the proposed model correlate to within 6.7% of measured values. Other studies present damage indices that generally increase as a function of percentage of failure. Of these, Miner's hypothesis is the crudest predicting the relationship as purely linear. Gao and Hsu [8] found that the trend was logarithmic but found that at low percentages of failure, the damage index was also relatively low. Finally, Suaris et al. [13] found that there was initial jump in damage at low failure percentage and then a logarithmic increase at mid-to-high levels of failure percentage. The newly proposed relationship (9) demonstrates an exponential trend and differs by a maximum 20%, 54%, and 12%, with Miner's hypothesis, Gao and Hsu [8], and Suaris et al. [13], respectively. Miner's hypothesis values differ from the measured data by a maximum of 24% and an average of 17%. Values using the relationship proposed by Gao and Hsu [8] differ from the measured data by a maximum of 47% and an average of 23%. Finally, values calculated using the equation suggested by Suaris et al. [13] differ from the measured values by a maximum of 13% and an average of 8%. Values calculated using (9) correlate with measured data within 7% indicating that the proposed method is more accurate in predicting the amount of damage induced on cyclically loaded unreinforced concrete specimen in comparison to previous research.

6. Conclusions

The long-term, structural health of concrete structures is difficult to quantify. To assist engineers, a new nondestructive, short impulse sensor was developed as part of this research that allowed for automated measurements of unconstrained compression waves through unreinforced concrete specimens subjected to repetitive compressive loading scenarios. This newly developed sensor was used to determine the
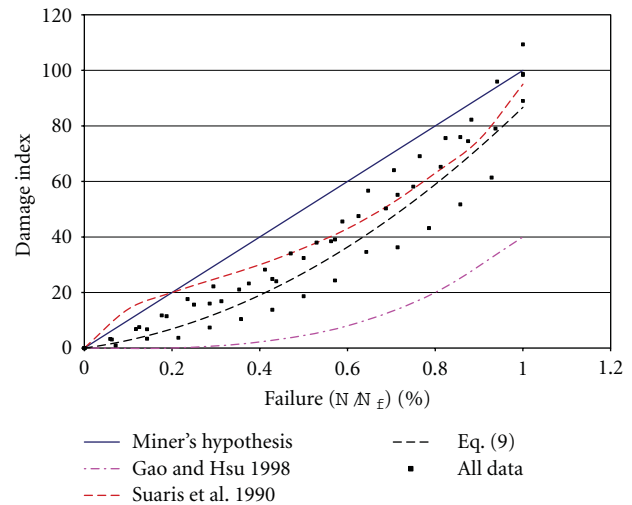
changes in the first longitudinal modal frequency and damping ratio as a function of cyclic loading to failure. The amount of energy absorbed by individual concrete specimens was calculated based on area of hysteretic curves measured during each cyclic load test. Several concrete mixes were sampled to include a wide range of compressive strengths. The results were used to develop an empirical relationship for damage accumulation. Results indicate the following.

(1) The newly developed short impulse excitation sensor allowed the automated process of accurate measuring unconstrained compression waves through concrete specimens under cyclic compressive loading scenarios to be very efficient and effective.

(2) After a series of cyclically applied compressive loads to failure, the first longitudinal modal frequencies were shown to decrease to a range of 88.5% to 93.3% of their initial, undamaged frequency. In general, higher-strength concretes exhibited less percentage loss of initial frequency at failure.

(3) Using the newly developed sensor, the measurements of total cumulative energy were shown to correlate with percentages of failure to within 4.7%. Also, higher-strength concretes exhibited an ability to absorb more energy at failure presumably due to the stronger concrete paste.

(4) A proposed, empirically derived, damage model was developed as a function of compressive strength, frequency, and energy. This proposed empirical relationship was shown to correlate with measured values to within 7%. Furthermore, the proposed relationship was shown to have a closer correlation than Miner's hypothesis and damage index models proposed from other reviewed research.

(5) The use of this new sensor has potential to be used on any type of concrete structure including, but not

limited to, beams, slabs, and columns. Further testing should be performed to determine its best applications.

References

[1] A. M. Neville, *Properties of Concrete*, Pearson Education Limited, 4th edition, 1996.

[2] P. S. Rao, B. S. Sarma, N. Lakshmanan, and F. Stangenberg, "Damage model for reinforced concrete elements under cyclic loading," *ACI Materials Journal*, vol. 95, no. 6, pp. 682–690, 1998.

[3] B. Garstka, W. B. Kratzig, and F. Stangenberg, "Damage assessment in cyclically loaded reinforced concrete members," in *Proceedings of the 2nd Cyclically Loaded Reinforced Concrete Members. Structural Dynamics (EURODYN '93)*, pp. 121–128, June 1993.

[4] K. Sadeghi, J. Lamirault, and J. G. Sieffert, "Damage indicator improvement applied on R/C structures subjected to cyclic loading," in *Proceedings of the 2nd Cyclically Loaded Reinforced Concrete Members. Structural Dynamics (EURODYN '93)*, pp. 129–136, June 1993.

[5] Y. J. Park and A. H. S. Ang, "Mechanistic seismic damage model for reinforced concrete," *ASCE Journal of Structural Engineering*, vol. 111, no. 4, pp. 722–739, 1985.

[6] T. T. C. Hsu, "Fatigue of Plain Concrete," *Journal of the American Concrete Institute*, vol. 78, no. 4, pp. 292–305, 1981.

[7] R. Gettu, A. Aguado, and M. O. F. Oliveira, "Damage in high-strength concrete due to monotonic and cyclic compression—a study based on splitting tensile strength," *ACI Materials Journal*, vol. 93, no. 6, pp. 519–523, 1996.

[8] L. Gao and C. T. T. Hsu, "Fatigue of concrete under uniaxial compression cyclic loading," *ACI Materials Journal*, vol. 95, no. 5, pp. 575–581, 1998.

[9] B. Y. Bahn and C. T. T. Hsu, "Stress-strain behavior of concrete under cyclic loading," *ACI Materials Journal*, vol. 95, no. 2, pp. 178–193, 1998.

[10] H. S. Abdelgader and J. Górski, "Stress-strain relations and modulus of elasticity of two-stage concrete," *Journal of Materials in Civil Engineering*, vol. 15, no. 4, pp. 329–334, 2003.

[11] A. Alliche and D. Francois, *Fracture of Concrete and Rock*, Springer, New York, NY, USA, 1989, Edited by S. P. Shah and S. E. Swartz.

[12] W. Suaris and V. Fernando, "Ultrasonic pulse attenuation as a measure of damage growth during cyclic loading of concrete," *ACI Materials Journal*, vol. 84, no. 3, pp. 185–193, 1987.

[13] W. Suaris, C. Ouyang, and V. M. Fernando, "Damage model for cyclic loading of concrete," *Journal of Engineering Mechanics*, vol. 116, no. 5, pp. 1020–1035, 1990.

[14] C. L. Nogueira and K. J. Willam, "Ultrasonic testing of damage in concrete under uniaxial compression," *ACI Materials Journal*, vol. 98, no. 3, pp. 265–275, 2001.

[15] C. Gheorghiu, J. E. Rhazi, and P. Labossière, "Impact resonance method for damage detection in RC beams strengthened with composites," in *Proceedings of the International Society for Optical Engineering*, vol. 5767 of *Proceedings of SPIE*, pp. 205–212, 2005.

[16] P. Shokouhi, "Stress dependency of sonic velocity in concrete under uniaxial load," in *Proceedings of the 87th Annual Meeting of the Transportation Research Record*, 2008.

[17] S. P. . Timoshenko and J. N. Goodier, *Theory of Elasticity*, McGraw-Hill, New york, NY, USA, 3rd edition, 1970.

[18] J. W. S. Rayleigh, *Theory of Sound*, Dover, New york, NY, USA, 1976.

Research Article

Envelope and Wavelet Transform for Sound Localisation at Low Sampling Rates in Wireless Sensor Networks

O. M. Bouzid, G. Y. Tian, J. Neasham, and B. Sharif

School of Electrical, Electronic and Computer Engineering, Newcastle University, Newcastle upon Tyne NE1 7RU, UK

Correspondence should be addressed to O. M. Bouzid, o.m.bouzid@ncl.ac.uk

High sampling frequencies in acoustic wireless sensor network (AWSN) are required to achieve precise sound localisation. But they are also mean analysis time and memory intensive (i.e., huge data to be processed and more memory space to be occupied which form a burden on the nodes limited resources). Decreasing sampling rates below Nyquist criterion in acoustic source localisation (ASL) applications requires development of the existing time delay estimation techniques in order to overcome the challenge of low time resolution. This work proposes using envelope and wavelet transform to enhance the resolution of the received signals through the combination of different time-frequency contents. Enhanced signals are processed using cross-correlation in conjunction with a parabolic fit interpolation to calculate the time delay accurately. Experimental results show that using this technique, estimation accuracy was improved by almost a factor of 5 in the case of using 4.8 kHz sampling rate. Such a conclusion is useful for developing precise ASL without the need of any excessive sensor resources, particularly for structural health monitoring applications.

1. Introduction

Integration of acoustic sensors into wireless sensor networks (WSNs) opens up new horizons for developing wired acoustic source localisation (ASL) systems to wireless systems [1]. This involves the utilisation of distributed sensor nodes which are able to realize onboard computation to achieve either distributed or centralized data manipulation. Such integration is adapted to a large variety of applications, including vehicle identification [2], structural health monitoring [3], and military activities [4, 5].

WSNs have been widely used in such applications due to the enormous number of advantages that are highlighted in [6]. This technology is also facing challenges as discussed in [7], where the authors provided a review and a discussion of the various issues associated with WSNs, including bandwidth and computational limitations at the level of sensor node.

High acquisition sampling rate is an important factor in ASL using WSNs. Thus, it still needs to be investigated in order to optimise this valuable technology as will be discussed in this paper. For example, high acquisition sampling rates, which are commonly used in wired ASL systems

[8] based on the Nyquist criterion and required for precise localisation, not only result in a high volume of data but also demand sufficient memory size and a large bandwidth for data transmission. In addition, the heavy traffic load is not applicable in WSNs due to the introduced high latency in data collection and increased power consumption [9].

This means that using high acquisition sampling rates in wireless ASL leads to more hardware complexity, more power consumption, and hence significantly higher production costs. Additionally, for other applications such as structural health monitoring, for example, powerful devices are not always available. This is especially so when the size of sensor node is restricted and power supply is difficult to obtain. Therefore, utilization of low sampling rates in this case will help in solving such problems, since the power consumption is linearly proportional to the sampling rate of an analog-to-digital converter [10]. Recently, there has been interest in the use of low data acquisition sampling rates in WSNs [11], so that low-cost commercial off-the-shelf (COTS) wireless nodes can be implemented without extra hardware.

Nevertheless, lowering the sampling frequency below the Nyquist criterion is detrimental due to information loss, which will produce inaccurate results for sound localisation.

In this case, conventional time-series methods such as cross-correlation (CC) will deliver inaccurate results if they are used directly to estimate the time delay. This is because, in the time domain, the sampling period determines the time resolution which is very low due to the low sampling frequency which means loss in time information. In frequency domain, the frequency contents are violated since we sample below Nyquist criterion.

This problem compels one to combine the time and the frequency domain information which results in time-frequency domain analysis. Such a domain provides information about how the signal content changes with time, thus providing an ideal technique to process and interpret the received signals at low sampling rates. A variety of time-frequency methods have been developed, including the short-time Fourier transform (STFT), Hilbert-Huang transform (HHT), Wigner-Ville distribution (WVD), and wavelet transform (WT). In this work, the last approach is utilized to overcome the challenge of using law sampling rates mentioned early as will be discussed in Section 2.

To the best of our knowledge, there is no previous wireless ASL system yet that uses low sampling rates below Nyquist criterion. Therefore, the goal of this research is to explore the feasibility of using low sampling rates in WSNs to develop low-cost, energy-efficient, and reliable wireless ASL and to achieve a reasonable estimation accuracy of sound location using time-frequency domain analysis, even if the Nyquist rule is violated. More specifically, our contribution in this paper is to

(1) counteract the impact of using low sampling rates on the estimation accuracy of sound source location by proposing the utilisation of envelope and wavelet transform cross-correlation (EWTCC) in conjunction with parabolic fit interpolation;

(2) show that as a result of employing EWTCC with parabolic fit interpolation technique low-cost COTS wireless nodes can be used in ASL applications through conducting several wireless ASL measurements and comparing the estimation performance of the proposed EWTCC algorithm by the conventional CC algorithm.

The paper is organized as follows. After explaining the reasons behind lowering sampling rate, Section 2 introduces the proposed method for locating a sound source using a wireless system. Section 3 presents the experimental setup for the wireless ASL system. In Section 4, we discuss and compare the estimation results of sound localisation using both proposed and conventional CC methods. Finally, conclusion is laid out in Section 5.

2. Proposed Localisation Approach at Low Sampling Rates

To the best of our knowledge, there is no specific algorithm yet that is suitable for time delay estimation (TDE) at low sampling rates. However, in [11], it has been shown that for sound source localisation applications low sampling frequencies can be used in WSNs provided that time-frequency domain and an appropriate analyse technique are utilized. If frequency domain algorithms are used to analyse the aliased version of the received signal, they will be unable to show the dominant spectral component at the original signal frequency. This means that a major portion of frequency contents is lost and any TDE in this domain will lead to inaccurate results. Furthermore, surrounding noise may affect the original signals. Therefore, using the aliased version of the received signal directly in the time or frequency domain will be insufficient and other techniques are, indeed, needed to counteract the effect of violence Nyquist criterion as well as noise effects and to improve the time resolution in order to gain feasible results.

In literature, utilisation of signal envelope instead of amplitudes in the TDE process is one of the preferable methods for accuracy improvement. This has been used in several applications such as ultrasonic ranging measurements [12–15]. The reason behind is to minimize the ambiguity presenting around the onset of signal amplitudes and peak indices if conventional cross correlation (CC) is used.

So far, using the envelope instead of amplitude signal values is an essential step but it is insufficient to establish a robust localisation algorithm at low sampling rates. Further steps are needed to enhance the estimation accuracy. Time-frequency domain algorithm such as WT which uses feature-based contents is a good candidate in this case, because it relies on the analysis of the time and spectral contents of the signal. In addition, WT has a distinctive attribute of utilizing changeable time-frequency windows in the analysis with respect to the conventional windowed cross-correlation method where a constant size window is applied. These significant WT properties help to induce further improvement in the TDE accuracy. Therefore, this kind of approach is selected in this work for extraction of time and frequency contents as well as noise elimination to estimate the time delay amongst received signals.

The proposed technique is a three-stage strategy as shown in Figure 1. In the first stage, the envelopes of the received signals (denoted by $\tilde{x}_i(t)$, $i \in \{1, 2, 3\}$) are extracted using the methods explained in Section 2.1. In the second stage, the WTs of these envelopes are computed. This is satisfied by the utilisation of discrete values of scaling s_j, $j = 1, 2, \ldots, N$. For each scaling value, the cross-correlation in conjunction with a parabolic fit interpolation in the wavelet domain is applied to estimate the time delay τ_{12j}. Finally, the average of the computed delays is calculated in order to obtain the final time delay τ_{12}. These steps are explained in more details in Section 2.3.

2.1. Envelope Extraction. As pointed out previously, the utilisation of envelopes rather than the absolute amplitude values of the aliased versions helps to optimise the signal shapes. It also minimizes the ambiguity around peak indices of CC. This means that envelopes present a nonambiguous feature for the sound source localisation.

In the literature, there are several methods, which can be employed to extract the envelopes of captured signals. Actually, any extraction methods can be used here as long as
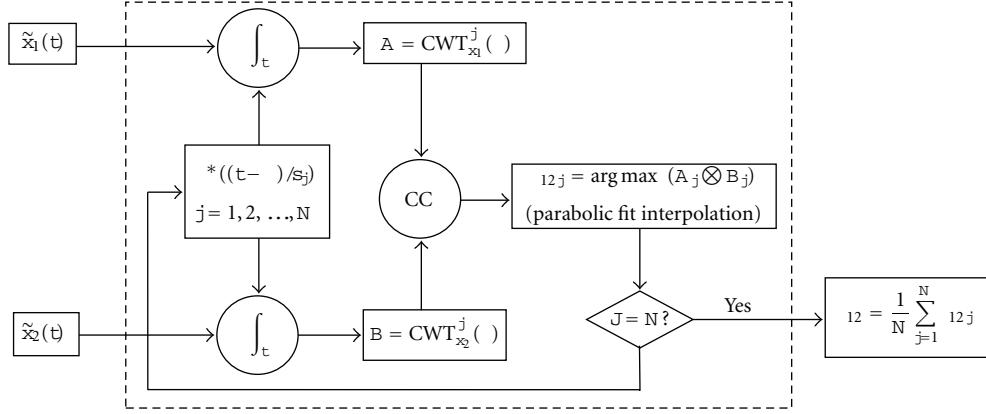
FIGURE 1: Detailed block diagram of the proposed algorithm.

no time delay is introduced due to this operation. Envelopes are usually extracted from bandpass filter outputs by full-wave rectification and lowpass filtering. Another method, which is implemented in this work, is to use the square root of the energies of the original and the Hilbert transformed signals as shown in (1) [16]:

$$\tilde{x}_i(t) = \sqrt{x_i(t)^2 + \hat{x}_i(t)^2}, \tag{1}$$

where $x_i(t)$ is the original signal, $\hat{x}_i(t)$ is the Hilbert transformed signal, $\tilde{x}_i(t)$ is the obtained envelope, and $i \in \{1, 2, 3\}$.

2.2. Wavelet Transform.

Both continuous wavelet transform (CWT) and discrete wavelet transform (DWT) have been found that they are effective approaches in many applications including signal processing fields. In this study, we propose to apply WT to counteract the impact of using low sampling rates on the estimation accuracy of a sound source location. In mathematics, WT is defined for a signal $x(t)$ as in (2):

$$\text{WT}_x^{\psi}(\tau, s) = |s|^{-1/2} \int x(t) \psi^* \left(\frac{t - \tau}{s}\right) dt, \tag{2}$$

where a mother wavelet can be expressed as in (3) [17]:

$$\psi_{(\tau, s)}(t) = |s|^{-1/2} \psi \left(\frac{t - \tau}{s}\right), \tag{3}$$

where $\psi(t)$ is the transforming function (mother wavelet), and $\tau \in \Re$ and $s > 0$ are the translation and scale parameters of the mother wavelet, respectively. $1/\sqrt{|s|}$ is an energy normalization factor and "*" denotes the complex conjugate [18]. Equation (2) is also known as the CWT which has the ability to break up a continuous-time function into wavelets through performing an inner production between the signal and a series of son wavelets. These series are generated by stretching and translation of the mother wavelet via controlling s and τ values [19]. Such an operation provides a capability to analyse the signal at different levels of resolutions and to present the processed signal in the time-frequency domain which offers a good time and frequency localisation as explained in the next section.

In addition, thanks to wavelet transform which offers several different valuable mother wavelets that can be employed in the CWT, DWT, and in the signal analysis, including Haar, Meyer, Morlet, Daubechies, Mexican Hat, Gabor, Gaussian, and others. This is, indeed, the strength of this transform which means that based on the signal features we are looking for we can select an optimum mother wavelet to ease our detection of that particular feature. In our proposed technique, we chose the Haar mother wavelet for processing the received signals because its shape is similar to the acoustic signals received by sensor nodes and therefore high correlations between them will result in. On the other hand, noises will be uncorrelated with the Haar wavelet and thus their effects can potentially be reduced in the estimation process.

DWT is another form of WT which involves the use of the dyadic scheme. This is satisfied by the utilisation of discrete values of scaling and translation $s = 2^j, \tau = k2^j, j, k \in Z$ [17], where Z denotes the set of integers. In this work, CWT is applied instead of DWT since the last transform is unsuitable for feature extraction [17]. This is because CWT does not require that the wavelet has to satisfy the orthogonality condition which makes it easy for the selection of an appropriate wavelet for feature extraction. Another reason for the utilisation of CWT is that it can be time-invariant which means that the same phase relationship is reserved and no additional time delay is introduced [17, 20, 21].

2.3. Sound Localisation Using Cross-Correlation.

The triangular configuration, illustrated in Figure 2, shows the positions of three sensor nodes. They are positioned in a straight line to construct a sensor array with a known geometry. One of the sensor nodes acts as a reference node and is positioned at P_2. The location of the two other sensor nodes varies between points P_0 and P_4 and accordingly the propagation path differences (PPDs) d_n and d_m also vary. The PPDs are the extra distances that the acoustic signals generated from "S" travel in order to reach the two sensor nodes with respect to the reference node. For simplicity, we assume that these nodes are located at points P_0 and P_4. Before we describe the
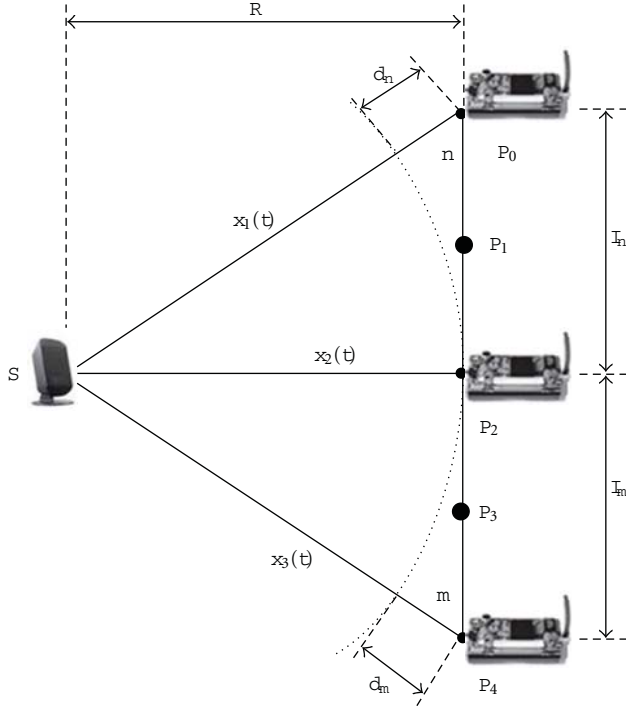
Figure 2: Triangular configuration of sensor nodes-sound source for the localization where P_i represents sensor node position and R is the shortest path between sound source "S" and the sensor node located at P_2.

proposed algorithm to estimate the PPDs, a mathematical model for the acoustic signals received at any microphone is illustrated.

As described in [8, 11] a mathematical model for the acoustic signal captured by any microphone of sensor node $x_i(t)$, $i \in \{1, 2, 3\}$ can be expressed as in (4):

$$x_i(t) = \alpha_i \, s(t - \tau_i) + \gamma_i(t), \tag{4}$$

where α_i represents an attenuation factor; τ_i is the delay time from the acoustic source $s(t)$ to the ith node; $\gamma_i(t)$ is assumed as a zero mean additive white Gaussian noise with average power $N_0 = 2\sigma^2$, where σ^2 is the noise variance at the ith node.

To estimate the time delay between any two received signals, for instance, $x_1(t)$ and $x_2(t)$, there are many techniques that can be applied to these signals such conventional CC, which is expressed as in (5) [22] and used here for comparison purpose:

$$R_{x_1 x_2}(\tau) = \frac{1}{(T - \tau)} \int_\tau^T x_1(t) x_2(t - \tau) dt, \tag{5}$$

where T is the observation time interval. The aim of (5) is to examine the coherence between the received signals to estimate the lag at which the CC function has its maximum.

In the proposed algorithm, the CWT is applied to the envelopes of the received signals, for example, $\tilde{x}_1(t)$ and

$\tilde{x}_2(t)$ just before doing CC. Equations (6) and (7) represent the CWT of these envelopes:

$$\mathrm{CWT}_{x1}^j(\tau) = \int \tilde{x}_1(t) \psi^* \left(\frac{t - \tau}{s_j} \right) dt, \tag{6}$$

$$\mathrm{CWT}_{x2}^j(\tau) = \int \tilde{x}_2(t) \psi^* \left(\frac{t - \tau}{s_j} \right) dt. \tag{7}$$

As stated in the previous section, varying the s parameter in the mother wavelet in (6) and (7) leads to dilate or compress the signals which allows to searching the similarity in terms of frequency contents between the series of son wavelets and $\tilde{x}_i(t)$ at each scale value: $s_j, j = 1, 2, \ldots, N$, where N is the number of variations and τ is assumed to be equal to the sampling period [17]. The process of dilating or compressing the signal via the scale variation allows us to analyse the signal and to compute the wavelet coefficients at different resolutions (multiresolution analysis). The CWT coefficients represent a measure of the cohesion between the signal and the mother wavelet at the current scale. If the frequency components of the signal are corresponding to the current scale of the mother wavelet, then the computed coefficients at this time instant in the time scale are a comparatively large quantity [17]. Two of 2D wavelet coefficients matrices will be generated for both (6) and (7), say A and B, respectively, as shown in Figure 1. Each row in A and B corresponds to the jth wavelet coefficients. The size of these matrices is $(N \times M)$ where M is the length of the processed signal. At each level of resolution the time delay is estimated. As seen in Figure 1 after obtaining the jth wavelet coefficients matrices, the CC algorithm in conjunction with curve-fitting interpolation is applied on the individual rows A_j and B_j and the delay under the jth scale is estimated as in (8):

$$\tau_{12j} = \arg\max_\tau \left(A_j \otimes B_j \right), \tag{8}$$

where "$\otimes$" denotes conventional cross-correlation. This process is repeated until $j = N$ and then the actual time delay τ_{12} between $x_1(t)$ and $x_2(t)$ can be calculated by taking the average of τ_{12j} as given in (9):

$$\tau_{12} = \frac{1}{N} \sum_{j=1}^{N} \tau_{12j}. \tag{9}$$

Once the time delays are estimated as shown in the previous paragraph using (9), the PPDs (d_n and d_m shown in Figure 2) can be computed using (10):

$$d_n = c\tau_{12}, \qquad d_m = c\tau_{23}, \tag{10}$$

where τ_{12} and τ_{23} are the relative time delays between $x_1(t)$ and $x_2(t)$ as well $x_2(t)$ and $x_3(t)$, respectively. c is the propagation speed of sound in air at room temperature and assumed to be constant in these experiments (340 ms-1). As a result, the acoustic source location can be estimated by applying a triangulation method between the sound source and the three sensor node positions as reported in the following paragraph.

In the following derivation of sound source location in 2D space, we assume that the sensor nodes (one, two, and three) are located at the positions P_0, P_2, and P_4, respectively. Nevertheless, this derivation can be generalized for using any three combinations of sensor locations. From the two triangles SP_0P_2 and SP_4P_2, we can derive the cosine relations for both angles φ_n and φ_m which are azimuths for sensor nodes one and three, respectively, as in (11) and (12):

$$\cos\varphi_m = \frac{l_m^2 + (R + d_m)^2 - R^2}{2l_m(R + d_m)}, \qquad (11)$$

$$\cos\varphi_n = \frac{l_n^2 + (R + d_n)^2 - R^2}{2l_n(R + d_n)}, \qquad (12)$$

where l_m and l_n represent the separation distances between sensor nodes as shown in Figure 2 and they are known. R is the shortest path between sound source and reference node. Similarly, from the triangle SP_0P_4 we can develop the expression in (13):

$$\cos(\varphi_m + \varphi_n) = \frac{(l_m + l_n)^2 - (R + d_m)^2 - (R + d_n)^2}{2(R + d_m)(R + d_n)}. \qquad (13)$$

Using (11)–(13) it is now possible to calculate, via appropriate substitutions, the three variables R, φ_n, and φ_m as in (14)–(16):

$$R = \frac{l_n(l_m^2 - d_m^2) - l_m(l_n^2 - d_n^2)}{2(d_m l_n + d_n l_m)}, \qquad (14)$$

$$\varphi_m = \cos^{-1}\frac{l_m^2 + (R + d_m)^2 - R^2}{2l_m(R + d_m)}, \qquad (15)$$

$$\varphi_n = \cos^{-1}\frac{l_n^2 + (R + d_n)^2 - R^2}{2l_n(R + d_n)}. \qquad (16)$$

As we can see in (14)–(16), by knowing the variables R, φ_m, and φ_n, we can estimate the sound source location in 2D. Moreover, the propagation path differences d_n and d_m play an important role in estimating these parameters, and the more accurate d_n and d_m are, the better the localisation results become.

As it is known in the classical time delay estimation measurements, the discrete cross-correlation is only calculated at integer indices. This means that it gives an inaccurate estimation if the true delay between two signals is a nonintegral multiple of the sample period. There are several techniques that can be used to optimise this resolution [23]. A common method which is used widely in resolution optimization is to use a parabolic interpolation. This is because the shape of cross-correlation output is similar to the Gaussian curve where the position of the peak is located at the center of this curve. Theoretically, fitting a parabola requires at least three points as shown in Figure 3: the maximum peak of correlation coefficients, its preceding, and subsequent neighbors. The blue dotted curve represents the fitted curve
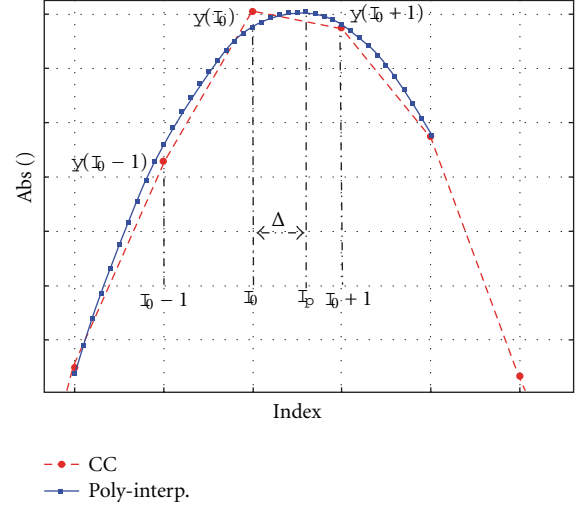

FIGURE 3: Curve-fitting interpolation using three points.

to the cross-correlation output (red dashed curve). These three points are needed to calculate the coefficients a, b, and c in (17) which represents the applied parabola [23]:

$$y = ax^2 + bx + c. \qquad (17)$$

To use this polynomial in the fitting process, we need to first calculate the coefficients a, b, and c. After that, by taking the derivative of (17) which equals zero at the maximum peak, we can compute the interpolated peak, I_p, as illustrated in (18):

$$I_p = -\frac{b}{2a}. \qquad (18)$$

A series of experiments have been conducted concentrating on the estimation of the propagation path differences to show the performance of the proposed approach.

Based on the used sample frequency (4807 Hz), the minimum distance resolution is 7.07 cm. To improve this resolution, we apply the parabolic fit interpolation on the output of the EWTCC. This results in an improvement in this distance resolution from 7.07 to 1.50 cm, which is almost five times better. Such a resolution improvement will contribute to the estimation accuracy of sound source location using WSNs at low sample rates as illustrated in the next section.

3. Experimental Work

The wireless acoustic source localisation system used in this work is depicted in Figure 4. The system was employed to study the utilisation of a single-hop WSN for sound source localisation at low sampling frequencies. Three acoustic sensor nodes were placed in a straight line. The sensor nodes are (MICAz) motes equipped with the sensor board (MTS310), which has different sensor modalities. The nodes sense simultaneously the omnidirectional microphone sensor modality of the sensor boards and send the data to a base station. All the sensor nodes communicate with the
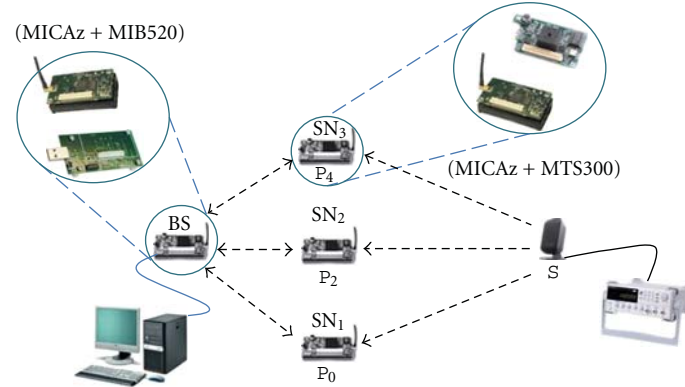
FIGURE 4: Three sensor nodes (SN_1, SN_2, and SN_3) positioned at locations P_0, P_2, and P_4, respectively, are used for acoustic source localization.

base station via an RF interface. The base station is plugged into the gateway board: MIB520, and it is used to forward the received signals to a PC where they are processed. The sensor nodes are programmed under TinyOS (TinyOS is a tiny operating system and has been widely used for WSNs design) environment. A Listen application is used to eavesdrop on messages sent over the mote radios and the data received are saved in a hexadecimal format. The received data are processed off-line using MATLAB. Time delays and the propagation path differences are estimated from acoustic signals captured using the approaches explained in Section 2.

Since we sample much below the Nyquist criterion and our proposed algorithm for TDE is based on the shapes contents of received signals, we have assumed that the acoustic signal which will be used as a test signal in the experimental work is a narrow bandwidth and not periodic signal because it is the type of signal we expect from a real scenario. This means that the generated acoustic signals has a finite pulse duration and the repetition period of this pulse is greater than the sampling duration in order to have one spike vanishes before the next spike is started. The length of the sampling duration also should be long enough to be admitted in order to collect a sufficiently amount of samples that represents a complete pulse.

Based on the aforementioned conditions an acoustic pulse test signal is used and simulated using a function generator through generating a tone burst of 50-sinusoidal cycles of frequency 10 kHz. The test signal is played through a PC speaker and such values are selected experimentally in order to generate a reasonable pulse shape for the conducted experiments. The generated acoustic signals are acquired at a 4807 Hz sampling rate for a sampling duration of 0.25 s. The 4807 Hz is almost the lowest sampling rate that MICAz mote can achieve using the hardware event handler (HEH) mode while in [11] it has been shown that sampling rates below this sampling rate can be used. An important condition here for reducing the sampling rate is that the samples should contain enough samples from the acoustic signal acquired in order to extract the envelope of the signal which should be sufficient to use in the time delay estimation process.

The experiments were conducted in an ordinary indoor laboratory environment which has objects, such as tables, PCs, and equipment. Street traffic and people talking contribute to the background noise where the experiments were being conducted. They were conducted as follows: a base station broadcasts a start sample command. Once sensor nodes receive it, they start sensing until the buffer becomes full (1200 data points). At this point, each node starts to send the acquired data back to the base station. To avoid data collisions nodes will send their own packets in sequence to the base station. In the future work, it is planned to process the received signals locally in the sensor node so that the advantage of utilizing low sampling rates will be obviously. The received data will be processed as shown in the next section.

4. Results and Discussion

In the conducted experiments, for the evaluation study the three sensor nodes were arranged in a straight line at different positions (P_0-P_4) as shown in Figure 4. Once the sensor nodes receive simultaneously a start sample command, they commence to acquire the generated acoustic signal as explained in Section 3.

Before presenting and discussing the results of this work, it is significant important to mention that sound source localisation using WSNs depends highly upon time synchronization among the sensors. However, from previous work in the area [24] and our preliminary experimental results, it is noticeable that the use of time-synchronized sensor nodes based on a global time does not guarantee that the acquired acoustic signals (i.e., sensing operation) are perfectly synchronized with each other. The adopted approach in performing a data acquisition operation also has a significant impact on achieving synchronized data acquisition operations. In general, nondeterministic (if the execution time of the same code varies at each repeated execution) operating systems have the disadvantage that they do not allow the user to control the execution process of their measurement process (i.e., setting priorities to the measurement steps). Such a property makes the execution of the data acquisition operations start at different time instants and also it does not
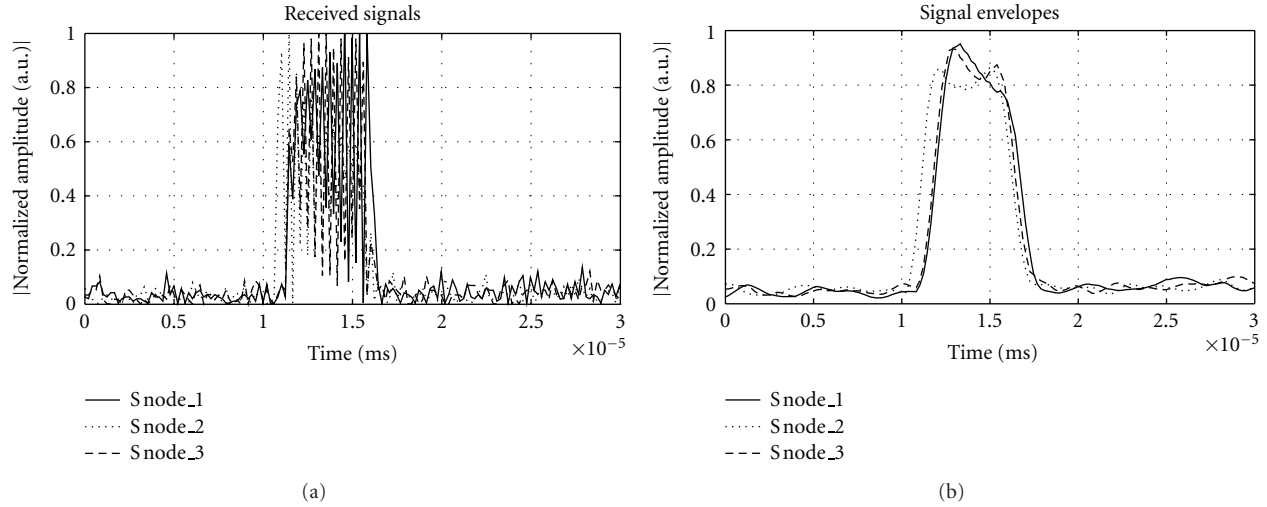
FIGURE 5: Received signals (zoom-in): (a) captured signals, (b) signal envelopes.

take the same amount of time for every execution, especially if it is performed on different microcontrollers, as in the case of WSNs.

TinyOS, which is used in this work as well as others [24], has two modes of execution threads: tasks and hardware event handler (HEH) [25]. The first mode has a nondeterministic nature, which introduces an unpredictable waiting time during the acquisition operation due to the TinyOS scheduler as it executes posted tasks. This results in unequal intervals which makes acoustic sensing tasks at all sensor nodes unsynchronized. To counteract this problem, the HEH mode is proposed to realize a synchronized data sensing amongst sensor nodes because it is a deterministic mode and asynchronous commands are executed immediately.

To verify this, sensor nodes were located at the same point where real PPD values are zeros. This configuration represents the extreme case and helps to test the performance of both modes (tasks and HEH) as it requires a high time resolution for accurate TDE from amongst the received signals. The experiments were repeated 15 times, and in each time, the PPDs were estimated through applying EWTCC algorithm to acquired signals as described in Section 2. The results of this test show clearly that the HEH mode exhibits much better performance than tasks mode. The RMS error of HEH mode is 1.7 cm whereas it is 24.11 cm for tasks mode case.

From the previous discussion, we can conclude that the tasks mode is not applicable in achieving a synchronized sensing process amongst all nodes. In contrast, the HEH mode results show much less synchronization errors. Minimizing these errors results in an improvement in the estimated sound source location. This is because such errors are accumulated to the real-time delays among received signal. Therefore, the HEH mode is chosen for realizing a synchronized data acquisition operation and designing a wireless sound localisation system.

Figure 5(a) shows the acoustic signals (zoom-in) captured using Sensor nodes 1, 2, and 3 as they were positioned at P_0, P_2, and P_4 in Figure 2, respectively. In contrast, Figure 5(b), depicts the signals envelopes extracted from these signals. In both figures, the solid curves represent the signals received at sensor node one and the dashed curves show the signals received at sensor node three. While the dotted curves illustrate the signals received at sensor node two (reference). As we can see in Figure 5(b), the extracted envelopes are much clearer than the original signals and therefore feeding these envelopes, instead of the original signals, to the Wavelet transform is an important step towards improving the localisation accuracy. In the conducted experiments, the distance between the reference node and the sound source represents the shortest path and that why the received signal from this sensor node appears first in Figure 5, whereas the other two sensor nodes were located equally apart from the reference node. Therefore, their received signals appear second and at the same time instance.

Figure 6 illustrates (zoom-in) the results of applying the CC and EWTCC with and without curve-fitting interpolation on envelopes shown in Figure 5(b). Such results illustrate the functionality of the proposed approach and give an example about how it improves the spatial resolution of the sound source localisation. The advantage of using the EWTCC here over the traditional CC method is to enhance the signal-to-noise ratio (SNR) due to the high correlation between these envelopes and used the Haar mother wavelet as well as to sharp the output of CC which makes the identification of the final (most accurate) index much easier when curve-fitting interpolation is utilised.

The experiments were also conducted for different values for d_m and d_n (i.e., positions of sensor nodes one and three were varied between P_0 and P_4). The results of these experiments are reported in Table 1. This table summarises the estimation results obtained by the developed wireless localisation system using both conventional CC and our proposed EWTCC with and without curve-fitting interpolation approaches in d_n and d_m estimations. It summarises the averages and the standard deviations of test results

TABLE 1: Averages (AVGs) and standard deviations (STDs) of estimated propagation path differences (PPDs) for 15 experiments.

| Configuration of | | Actual PPDs | Estimated PPDs (cm) | | | | | |
| SN$_1$ SN$_2$ SN$_3$ | | (cm) | CC | | EWTCC | | EWTCC- Fitting | |
			AVG	STD	AVG	STD	AVG	STD
P_2 P_2 P_2	d_m	00.00	6.14	3.07	1.83	1.17	1.15	0.81
	d_n	00.00	2.56	4.58	1.96	1.87	1.27	1.06
P_0 P_2 P_3	d_m	15.00	12.26	5.65	14.10	3.53	15.19	2.64
	d_n	36.00	26.41	20.62	37.11	3.89	36.49	3.71
P_1 P_2 P_3	d_m	21.00	23.11	9.44	22.95	5.02	21.40	4.12
	d_n	15.00	12.26	10.51	16.55	5.69	15.65	4.53
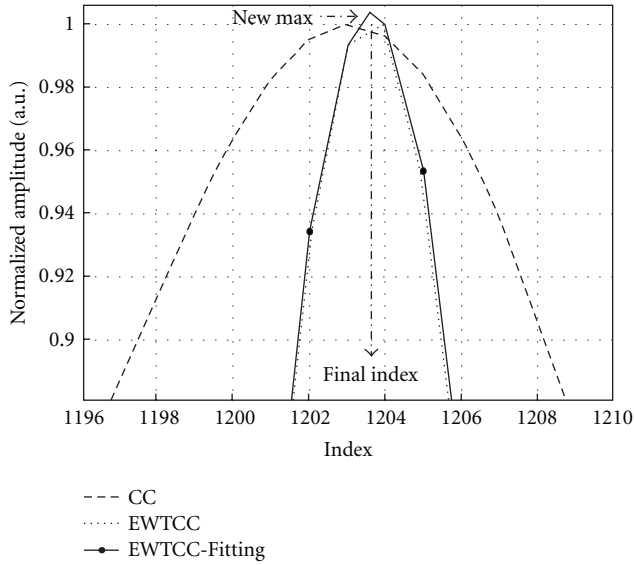
FIGURE 6: Output (Zoom-In) of CC and EWTCC with and without parabolic fit interpolation.

FIGURE 7: RMS errors for CC, EWTCC, and EWTCC-Fitting algorithms.

gained from 15 experiments in order to show that replicated measurements can provide closely similar results. It is apparent from this table that results of applying EWTCC with curve-fitting interpolation are much more correlated to the real values of d_n and d_m than the other results. A good example of this is the case where $d_n = 15$ cm. The average of the estimated result using EWTCC with fitting is 15.65 cm, while it is 12.26 cm using CC and 16.55 using EWTCC without fitting. Again, the variation of the EWTCC with fitting result is 4.53 compared to the other two cases. This means that errors in estimation of d_n and d_m using EWTCC with curve-fitting interpolation are much less than errors in the CC method due to the multiresolution analysis property of CWT and curve interpolation. Consequently, the use of such method in estimation of PPDs exhibits better performance than employing the CC method as shown in Figure 7.

Figure 7 illustrates the RMS computed errors for the three configurations shown in Table 1. As seen from this figure, the maximum RMS errors in estimation of d_n and d_m using EWTCC with curve-fitting interpolation is 1.70 cm while it is 2.68 cm using just EWTCC and 9.97 cm using
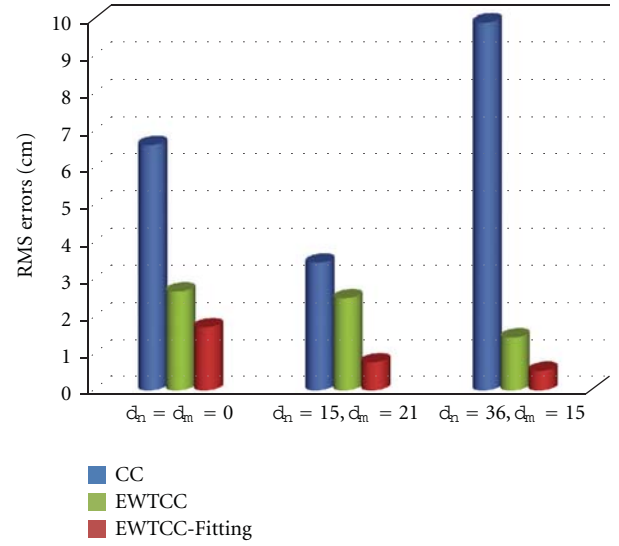
CC. In addition, the trend of the RMS errors using the proposed method shows that RMS errors decreases with moving away from the worst case scenario, whereas, they are randomly for the CC algorithm case. Such an enhancement in the estimation accuracy of sound localisation correlated to two reasons: (1) employing envelopes of acquired signals reduces the ambiguity present around peak indices of CC; (2) processing these envelops in time-frequency domain using WT integrates both time and spectral contents in the estimation-process. Thus, EWTCC algorithm in conjunction with curve-fitting interpolation is able to achieve a sufficient level of estimation accuracy for wireless ASL at low sampling rates compared to the CC method.

5. Conclusion

Envelope and wavelet transform cross-correlation, EWTCC, in conjunction with a parabolic fit interpolation method is proposed for wireless ASL employing low sampling rates. The new technique, in comparison to conventional CC algorithm, offers a multiresolution analysis domain which shows a potential performance in counteracting the ambiguous

peaks due to the low time resolution. The proposed approach also enhances the spatial resolution of the localisation process from 7.07 cm to 1.50 cm. Such results of the conducted experiments show the consistence and low errors for the case study; further evaluation work can be done for large-scale measurement, including complex geometrical and local data processing scenarios as well as optimisation of the estimation process through selection of the best scale values which delivers the best resolution. In addition, the proposed HEH mode realizes a synchronized data acquisition operation for all sensor nodes in the TinyOS-based WSNs. It must be emphasized here that such conclusions can open up new horizons for the development of efficient low-cost, reliable wireless ASL systems based on low-cost COTS sensor nodes without the need to support excessive sensor resources, as low sampling rates not only contribute to a cost reduction but also minimize power consumption and extend the lifetime of sensor nodes which allows having the processing operations in real time.

Acknowledgment

References

[1] J. C. Chen, L. Yip, J. Elson et al., "Coherent acoustic array processing and localization on wireless sensor networks," *Proceedings of the IEEE*, vol. 91, no. 8, pp. 1154–1161, 2003.

[2] M. F. Duarte and Y. H. Hu, "Vehicle classification in distributed sensor networks," *Journal of Parallel and Distributed Computing*, vol. 64, no. 7, pp. 826–838, 2004.

[3] A. Lédeczi, T. Hay, P. Völgyesi, D. R. Hay, A. Nádas, and S. Jayaraman, "Wireless acoustic emission sensor network for structural monitoring," *IEEE Sensors Journal*, vol. 9, no. 11, pp. 1370–1377, 2009.

[4] M. Winkler, K.-D. Tuchs, K. Hughes, and G. Barclay, "Theoretical and Practical aspects of military wireless sensor networks," *Journal of Telecommunications and Information Technology*, vol. 2, pp. 37–45, 2008.

[5] J. Sallai, W. Hedgecock, P. Volgyesi, A. Nadas, G. Balogh, and A. Ledeczi, "Weapon classification and shooter localization using distributed multichannel acoustic sensors," *Journal of Systems Architecture*, vol. 57, no. 10, pp. 869–885, 2011.

[6] J. Yick, B. Mukherjee, and D. Ghosal, "Wireless sensor network survey," *Computer Networks*, vol. 52, no. 12, pp. 2292–2330, 2008.

[7] A. Jangra, Swati, Richa, and Priyanka, "Wireless sensor network (WSN): architectural design issues and challenges," *IJCSE: International Journal on Computer Science and Engineering*, vol. 2, no. 9, pp. 3089–3094, 2010.

[8] H. Atmoko, D. C. Tan, G. Y. Tian, and B. Fazenda, "Accurate sound source localization in a reverberant environment using multiple acoustic sensors," *Measurement Science and Technology*, vol. 19, no. 2, Article ID 024003, 2008.

[9] C. T. Cheng, C. K. Tse, and F. C. M. Lau, "An efficient data collecting network structure in wireless sensor networks," in *Proceedings of the International Conference on Communications, Circuits and Systems (ICCCAS '08)*, pp. 444–447, May 2008.

[10] K. Philips, ΣΔ *A/D conversion for signal conditioning*, Ph.D. thesis, 2005.

[11] O. M. Bouzid, G. Y. Tian, J. Neasham, and B. Sharif, "Investigation of sampling frequency requirements for acoustic sourcelocalisation using wireless sensor networks," *Applied Acoustics*. In press.

[12] R. Raya, A. Frizera, R. Ceres, L. Calderón, and E. Rocon, "Design and evaluation of a fast model-based algorithm for ultrasonic range measurements," *Sensors and Actuators, A*, vol. 148, no. 1, pp. 335–341, 2008.

[13] F. E. Gueuning, M. Varlan, C. E. Eugène, and P. Dupuis, "Accurate distance measurement by an autonomous ultrasonic system combining time-of-flight and phase-shift methods," *IEEE Transactions on Instrumentation and Measurement*, vol. 46, no. 6, pp. 1236–1240, 1997.

[14] A. Egaña, F. Seco, and R. Ceres, "Processing of ultrasonic echo envelopes for object location with nearby receivers," *IEEE Transactions on Instrumentation and Measurement*, vol. 57, no. 12, pp. 2751–2755, 2008.

[15] X. L. Xu, A. H. Tewfik, and J. F. Greenleaf, "Time delay estimation using wavelet transform for pulsed-wave ultrasound," *Annals of Biomedical Engineering*, vol. 23, no. 5, pp. 612–621, 1995.

[16] B. S. Lazarov, R. Matzen, and Y. Elesin, "Topology optimization of pulse shaping filters using the Hilbert transform envelope extraction," *Structural and Multidisciplinary Optimization*, vol. 44, no. 3, pp. 409–419, 2011.

[17] J. Lin and A. Zhang, "Fault feature separation using wavelet-ICA filter," *NDT and E International*, vol. 38, no. 6, pp. 421–427, 2005.

[18] O. Rioul and P. Duhamel, "Fast algorithms for discrete and continuous wavelet transforms," *IEEE Transactions on Information Theory*, vol. 38, no. 2, pp. 569–586, 1992.

[19] K. C. Ho and Y. T. Chan, "Optimum discrete wavelet scaling and its application to delay and doppler estimation," *IEEE Transactions on Signal Processing*, vol. 46, no. 9, pp. 2285–2290, 1998.

[20] J. Lin and L. Qu, "Feature extraction based on morlet wavelet and its application for mechanical fault diagnosis," *Journal of Sound and Vibration*, vol. 234, no. 1, pp. 135–148, 2000.

[21] M. Lang, H. Guo, J. E. Odegard, C. S. Burrus, and R. O. Wells, "Noise reduction using an undecimated discrete wavelet transform," *IEEE Signal Processing Letters*, vol. 3, no. 1, pp. 10–12, 1996.

[22] J. P. Ianniello, "Time delay estimation via cross-correlation in the presence of large estimation errors," *IEEE Transactions on Acoustics, Speech, and Signal Processing*, vol. 30, no. 6, pp. 998–1003, 1982.

[23] N. S. M. Tamim and F. Ghani, "Techniques for optimization in time delay estimation from cross correlation function," *IJET/IJENS: International Journal of Engineering & Technology*, vol. 10, no. 2, pp. 39–68, 2010.

[24] T. Nagayama, S. H. Sim, Y. Miyamori, and B. F. Spencer, "Issues in structural health monitoring employing smart sensors," *Smart Structures and Systems*, vol. 3, no. 3, pp. 299–329, 2007.

[25] P. Levis and D. Gay, *TinyOS Programming*, Cambridge University Press, Cambridge, UK, 2009.

Research Article

Flexible GMR Sensor Array for Magnetic Flux Leakage Testing of Steel Track Ropes

W. Sharatchandra Singh, B. P. C. Rao, S. Thirunavukkarasu, and T. Jayakumar

NDE Division, Indira Gandhi Centre for Atomic Research, Kalpakkam 603 102, India

Correspondence should be addressed to B. P. C. Rao, bpcrao@igcar.gov.in

This paper presents design and development of a flexible GMR sensor array for nondestructive detection of service-induced defects on the outer surface of 64 mm diameter steel track rope. The number of GMR elements and their locations within saddle-type magnetizing coils are optimized using a three dimensional finite element model. The performance of the sensor array has been evaluated by measuring the axial component of leakage flux from localized flaw (LF) and loss of metallic cross-sectional area (LMA) type defects introduced on the track rope. Studies reveal that the GMR sensor array can reliably detect both LF and LMA type defects in the track rope. The sensor array has a fast detection speed along the length of the track rope and does not require circumferential scanning. It is also possible to image defects using the array sensor for obtaining their spatial information.

1. Introduction

Track ropes are a type of wire ropes used for transportation of coal in mining industries. One such rope system is operated for about 10 hours every day to transport 3000 tons of coal with the help of 256 numbers of buckets, each carrying nearly 1.6 tons of coal. The track rope is stationary and is rigidly supported by towers at periodic intervals. As shown in Figure 1, the track rope has 8 layers of stranded wires of different diameters. The 6 inner layers are round-type wires, while the outer two layers are Z-type wires. The round wires are locked by two Z wires to get the strength of the rope. The width of the outer surface of the first Z wire is 6.45 mm, and the gap width between two outer Z wires is 0.76 mm.

During the operation of the rope system, the carriage wheels of the bucket come in contact with the top surface of the outer Z wire as shown in Figure 2(a). Prolonged use of the rope system is expected to cause abrasion and wear, resulting in loss of metallic cross-sectional area (LMA) or localized flaw (LF) type defects (Figure 2(b)). Also wire breakage and formation of fatigue cracks, pitting corrosion, inter strand nicking or martensitic embrittlement, and so forth are likely to occur [1, 2]. When more than two Z wires of the outer layer are broken, they will be separated from the adjacent layers. Detection of damage in track rope is essential as part of the condition monitoring and life management programs. Nondestructive detection of damage in the track rope is challenging due to heterogeneous structure of the rope, multiplicity and uncertainty of broken wires, and hostile working environment.

Among various nondestructive evaluation (NDE) techniques, visual and magnetic flux leakage (MFL) techniques are widely used for monitoring the health of steel track ropes [3, 4]. Although visual inspection is simple and does not require special instrumentation, it is not suited for monitoring the internal deterioration in track ropes. On the contrary, the MFL technique is capable of detecting both LF and LMA type defects in wire ropes [4].

In MFL technique, wire ropes are locally magnetized using electromagnets or permanent magnets. If any defect is present in the rope, the magnetic flux produced in the rope takes a longer path around the defect and as a result, some amount of flux lines leak out of the surface. Measurement of this leakage flux using sensors forms an important step in MFL testing. The leakage flux has axial (along the rope length) and radial components which can be detected using
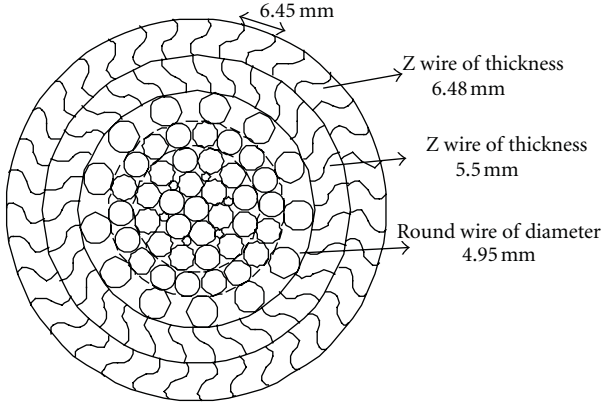
FIGURE 1: The cross-section of double locked track rope.

coils [5, 6] or sensors [7–9] and correlated to the size and location of the defects. The magnetization can be continuous [10] or pulsed [11, 12]. Recently, authors proposed GMR sensor [13, 14] -based technique for NDE of track ropes, and this requires the use of sophisticated scanning set-up for circumferential scanning over the ropes. Use of array sensors is attractive, and this enables fast and reliable inspection of track ropes [15]. This paper discusses the design and development of a flexible GMR sensor array for detection of damage on the outer surface of the track rope. The performance of the array sensor has been evaluated for fast inspection of track rope and imaging of LF and LMA type defects on the outer Z-wire of the track rope.

2. GMR Sensor

GMR sensor consists of a few nm thick multilayer structures (Co/Cu/Co) in which ferromagnetic layers are separated by nonmagnetic layers. The sensor works on GMR effect in which there is a large drop in electrical resistance of multilayer for an incident magnetic field, due to the spin dependent scattering of electrons [16]. The GMR sensors are characterized by high sensitivity at low magnetic field and high spatial resolution. They are inexpensive and consume less power [17]. In this study, the GMR sensors are connected in bridge configuration to measure the differential output with high stability. The sensor is encapsulated with standard SOIC-8 package of $5.9 \times 4.9 \times 1.4 \, mm^3$ size. The maximum hysteresis of the GMR sensor is 2% unit.

3. Three Dimensional Finite Element Modeling

In order to identify the number of GMR elements required to cover the top surface of the track rope and to determine the sensor locations, 3D finite element modeling has been performed using COMSOL 3.4 Multiphysics software package. Figure 3(a) shows the mesh generated for the geometry which consists of a track rope (length 300.0 mm, outer diameter 64.0 mm) and magnetizing coils. Equation (1) has

been solved in three dimensions using the finite element method:

$$\nabla \times \frac{1}{\mu_0 \mu_r} \nabla \times A = J, \tag{1}$$

where A is the magnetic vector potential, μ_0 is the magnetic permeability of free space, μ_r is the relative permeability, and J is current density. Two saddle coils (length 120.0 mm, width 35.0 mm) each consisting of 90 turns with a cross-sectional area of $20.0 \times 10.0 \, mm^2$ are used for magnetization of the track rope at a current of 5 A, as shown in Figure 3(a). The magnetizing current in the saddle coils is set in opposite directions to ensure axial magnetization of the rope region between the saddle coils.

For simplicity, in the model the track rope is assumed as a solid rod, and GMR sensor as well as velocity effects is not modeled. The relative magnetic permeability of the rope is assumed constant as 100. Magnetic insulation ($n \times A = 0$) boundary condition is applied at the outer boundaries constructed for the model. The computation time for solving (1) with 5673392 degrees of freedom is approximately 50 minutes in a dual-core 64 bit processor workstation with 8 GB primary memory.

The magnetic vector potential is computed in the solution region, and the axial component of the magnetic flux density (B_z) between the two saddle coils is predicted. As can be seen from Figure 3(b), the magnetic flux density is nearly uniform for an optimum circumferential intercoil distance of 80.0 mm that completely covers the expected damage region on the top surface of the Z-wire (dotted region in Figure 3(b)). This region can accommodate 12 GMR sensors. Hence, a flexible array of 12 GMR sensors has been fabricated and used for detection of damage on the track rope.

4. Design of GMR Sensor Array

The layout of the flexible GMR sensor array and its photograph are shown in Figures 4(a) and 4(b), respectively. Each sensor element in the array has a common power input of 5 V, and the array has 12 differential outputs. The overall size of the sensor array is $100 \times 12 \, mm^2$ with a centre-to-centre distance (pitch) between two sensors of 6.6 mm. The sensor array is kept at the middle of the magnetizing coils. The GMR sensors measure the axial component (along the scan direction) of leakage flux from defects. The array sensor maintains a constant lift-off of 1 mm. The sensors' outputs are acquired and analysed using a LabVIEW-based data acquisition system incorporating averaging and low-pass filter to minimize noise.

5. Performance Evaluation

The performance of the sensor array has been evaluated by measuring the axial component of leakage fields from two LF and two LMA type defects in track rope. The two LFs are simulated by electro discharge machining (EDM) notches of size $5.5 \times 2.0 \times 2.0 \, mm^3$ (length $\times$ width $\times$ depth) oriented
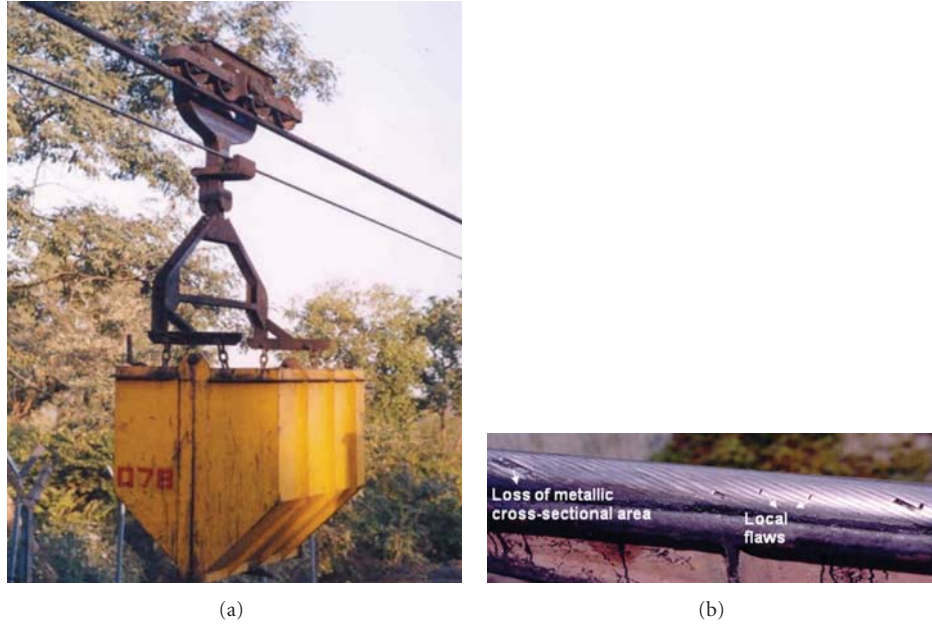
(a)

(b)

FIGURE 2: (a) photograph of the track rope system with bucket carrying coal and (b) local flaws and loss of metallic area at the outer surface of the track rope.
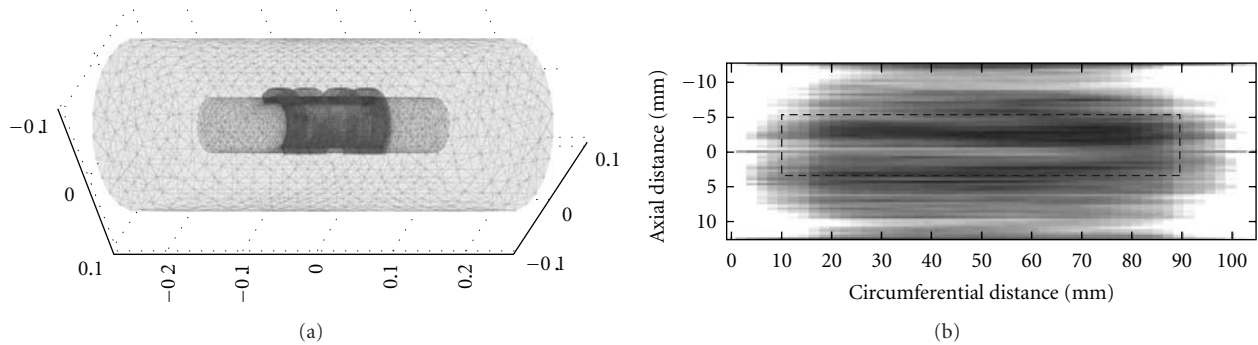

(a)

(b)

FIGURE 3: (a) 3D finite element mesh and (b) predicted magnetic flux density between the saddle coils along half of circumferential distance.

along axial and circumferential directions in the track rope, as shown in Figures 5(a) and 5(b). The two LMAs of sizes $42.0 \times 9.0 \times 3.0\ mm^3$ and $33.5 \times 14.2 \times 4.9\ mm^3$ are made along axial and circumferential directions, respectively (refer to Figures 5(c) and 5(d)).

The test set-up used for evaluation of performance of the GMR sensor array is shown in Figure 6. It consists of two saddle coils, variable DC power supply, track rope, flexible sensor array, GMR field meter, and a personal computer. Each saddle coil consists of 90 turns with a cross-sectional area of $20 \times 10\ mm^2$. The centre-to-centre distance between the two saddle coils is 80 mm. Measurements are made by moving the sensor array and the magnetization coils together as a single unit over the track rope. For this, a DC servo motor is used, as shown in Figure 6. In order to enhance the sensitivity, each GMR sensor output is amplified using low-noise differential amplifiers and notch rejection filter at 50 Hz, followed by 100 kHz low-pass filter. The sensor

outputs are digitized using a 16-channel data acquisition system of 16-bit resolution.

The MFL signals of the sensor array for a circumferential LF of $5.5 \times 2.0 \times 2.0\ mm^3$ in the track rope are shown in Figure 7. As the length of the flaw is 5.5 mm, only two GMR sensors, namely, S6 and S7 have shown the output of the leakage flux.

The GMR array sensor output has been processed for removing background noise and formatted to obtain images. Typical MFL images of axial and circumferential LFs of size $5.5 \times 2.0 \times 2.0\ mm^3$ are shown in Figures 8(a) and 8(b), respectively. As compared to the MFL signals, it is possible to readily discern the spatial extent of the flaws from the MFL images produced by the sensor array. The MFL image of the axial LF is found to be extended as compared to that of the circumferential LF.

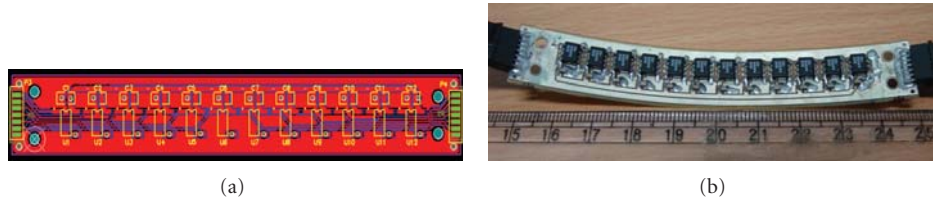Typical MFL images of axial and circumferential LMAs are shown in Figures 9(a) and 9(b), respectively. As can be

(a)

(b)

FIGURE 4: (a) the layout of the 12-element GMR sensor array on a flexible PCB and (b) the fabricated flexible sensor array.
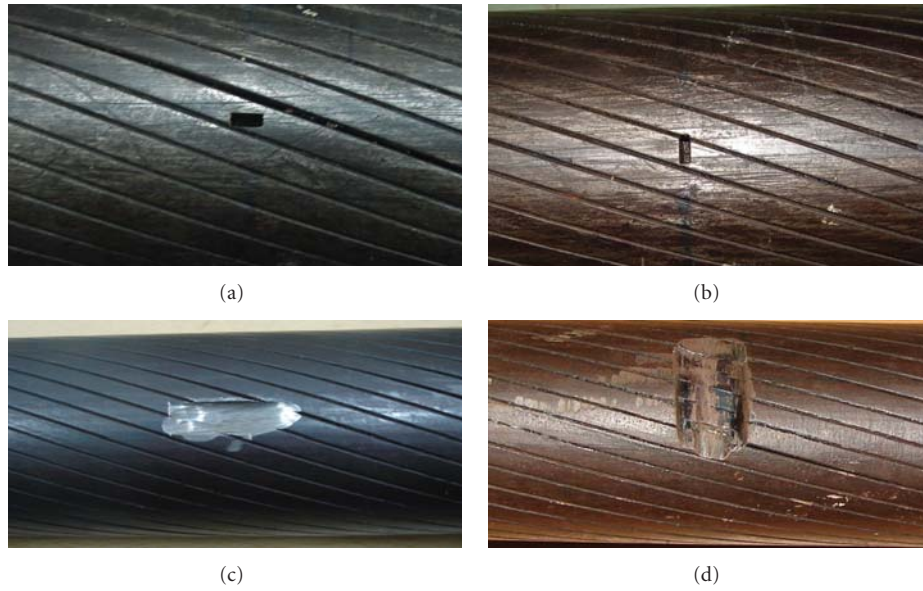

(a)

(b)

(c)

(d)

FIGURE 5: photographs of (a) axial LF, (b) circumferential LF, (c) axial LMA, and (d) circumferential LMA type defects in the track rope.
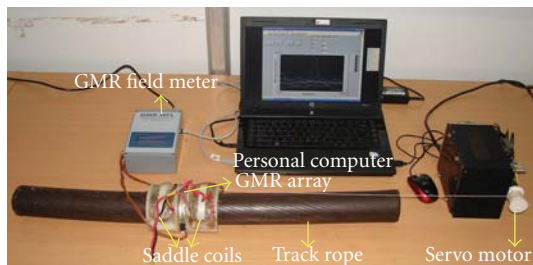

FIGURE 6: Test set-up used for performance evaluation of flexible GMR sensor array.

FIGURE 7: GMR sensor array response for a 5.5 mm long circumferential LF.

noted, the spatial extents of the LMAs could be readily felt from the images, despite some random noise. In the case of circumferential LMA, the output of three sensors, namely, S5, S6, and S7 that are exactly over the LMA defect have been found saturated due to high leakage field.

The flexible GMR sensor array designed has shown detection capability for both LF and LMA type defects oriented along the axial as well as circumferential directions. The sensor array has a fast detection speed along the length of the track rope and does not require circumferential scanning like in [13]. The images of circumferential notches have been found to be sharp and lo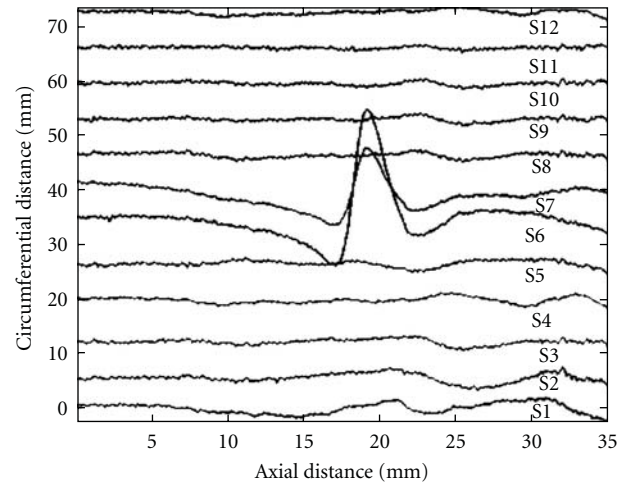calized as compared to that of the axial notches. Thus, the flexible GMR array sensor proposed in this paper can be used for rapid nondestructive inspection of track ropes. Towards deployment of the sensor array for field use, studies are in progress to assess the probability of detection (POD) of the MFL technique. Studies are also
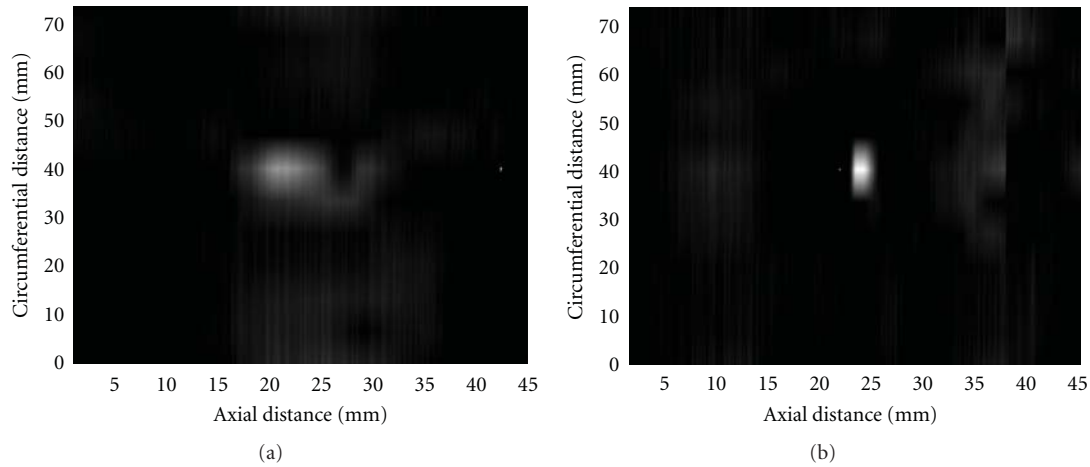
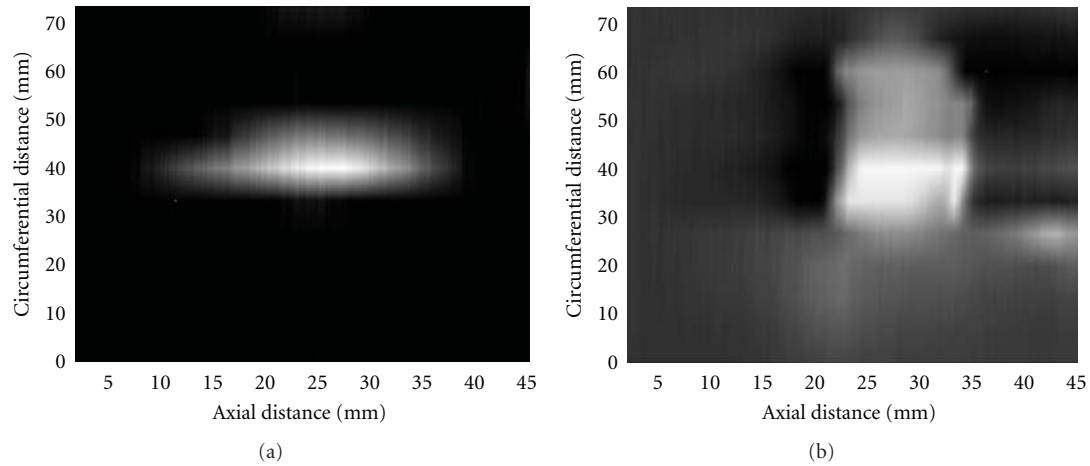FIGURE 8: MFL images for (a) axial and (b) circumferential LFs.

FIGURE 9: MFL images of (a) axial LMA ($42.0 \times 9.0 \times 3.0$ mm^3) and (b) circumferential LMA ($33.5 \times 14.2 \times 4.9$ mm^3).

in progress to enhance the detection capability for defects located in between sensor elements as well as the resolution of the sensor array, through the use of another tandem sensor array beside, with a slight angular shift.

6. Summary

A flexible GMR array sensor has been developed for fast magnetic flux leakage testing of 64 mm diameter steel track rope through detection of leakage magnetic fields from LF and LMA type defects on Z-wire rope. Three dimensional finite element modeling has been performed to identify the number of GMR sensor elements and their locations. The performance of the sensor array has been evaluated using machined LF and LMA type defects in the outer Z-wire. The flexible array sensor has shown detection of both types of defects in the track rope, with the possibility for imaging to obtain the spatial information of the defects.

References

[1] D. Basak, "Performance comparison of drive ropes in a cable belt conveyor system using an NDT technique," *Insight*, vol. 51, no. 8, pp. 439–441, 2009.

[2] H. R. Weischedel and R. P. Ramsey, "Electromagnetic testing, a reliable method for the inspection of wire ropes in service," *NDT International*, vol. 22, no. 3, pp. 155–161, 1989.

[3] H. R. Weischedel, "The inspection of wire ropes in service: a critical review," *Materials Evaluation*, vol. 43, no. 13, pp. 1592–1605, 1985.

[4] N. Sumyong, A. Prateepasen, and P. Kaewtrakulpong, "Influence of scanning velocity and gap distance on magnetic flux leakage measurement," *ECTI Transactions on Electrical Engineering, Electronics and Communications*, vol. 5, no. 1, pp. 118–122, 2007.

[5] C. Jomdecha and A. Prateepasen, "Design of modified electromagnetic main-flux for steel wire rope inspection," *NDT and E International*, vol. 42, no. 1, pp. 77–83, 2009.

[6] E. Kalwa and K. Piekarski, "Design of inductive sensors for magnetic testing of steel ropes," *NDT International*, vol. 20, no. 6, pp. 347–353, 1987.

[7] E. Kalwa and K. Piekarski, "Design of Hall-effect sensors for magnetic testing of steel ropes," *NDT International*, vol. 20, no. 5, pp. 295–301, 1987.

[8] W. S. Singh, B. P. C. Rao, S. Vaidyanathan, T. Jayakumar, and B. Raj, "Detection of leakage magnetic flux from near-side and far-side defects in carbon steel plates using a giant magneto-resistive sensor," *Measurement Science and Technology*, vol. 19, no. 1, Article ID 015702, 2008.

[9] J. W. Wilson and G. Y. Tian, "3D magnetic field sensing for magnetic flux leakage defect characterisation," *Insight: Non-Destructive Testing and Condition Monitoring*, vol. 48, no. 6, pp. 357–359, 2006.

[10] W. S. Singh, B. P. C. Rao, T. Jayakumar, and B. Raj, "Simultaneous measurement of tangential and normal component of leakage magnetic flux using GMR sensors," *Journal of Non-Destructive Testing & Evaluation*, vol. 8, no. 2, pp. 23–28, 2009.

[11] A. Sophian, G. Y. Tian, and S. Zairi, "Pulsed magnetic flux leakage techniques for crack detection and characterisation," *Sensors and Actuators, A*, vol. 125, no. 2, pp. 186–191, 2006.

[12] J. W. Wilson and G. Y. Tian, "Pulsed electromagnetic methods for defect detection and characterisation," *NDT and E International*, vol. 40, no. 4, pp. 275–283, 2007.

[13] W. S. Singh, B. P. C. Rao, C. K. Mukhopadhyay, and T. Jayakumar, "GMR-based magnetic flux leakage technique for condition monitoring of steel track rope," *Insight*, vol. 53, no. 7, pp. 377–381, 2011.

[14] W. S. Singh, B. P. C. Rao, S. Mahadevan, and T. Jayakumar and B. Raj, "Giant magneto-resistive sensor based magnetic flux leakage technique for inspection of track ropes," *Studies in Applied Electromagnetics and Mechanics, Electromagnetic Nondestructive Evaluation (XIV)*, vol. 35, pp. 256–263, 2011.

[15] R. Grimberg, L. Udpa, A. Savin, R. Steigmann, V. Palihovici, and S. S. Udpa, "2D Eddy current sensor array," *NDT and E International*, vol. 39, no. 4, pp. 264–271, 2006.

[16] M. N. Baibich, J. M. Broto, A. Fert et al., "Giant magnetoresistance of (001)Fe/(001)Cr magnetic superlattices," *Physical Review Letters*, vol. 61, no. 21, pp. 2472–2475, 1988.

[17] B. P. C. Rao, T. Jayakumar, and B. Raj, "Electromagnetic NDE techniques for materials characterization," in *Ultrasonic and Advanced Methods for Non-Destructive Testing and Material Characterisation*, C. H. Chen, Ed., chapter 11, pp. 262–265, World Scientific Publishing, Singapore, 2007.